Monte Carlo Simulation of Large Angle Scattering Effects

in

Heavy Ion Elastic Recoil Detection Analysis and

Ion Transmission Through Nanoapertures

Rick D. Franich

BSc (Hons), DipEd.

A thesis submitted for the degree of

Doctor of Philosophy

School of Applied Sciences

Science Engineering and Technology Portfolio

RMIT University

Melbourne, Australia

May 2007

Declaration

Except where acknowledgements are made in the text, all work described in this thesis is that of the author. This thesis has not previously been submitted in whole or in part for any academic award to any Institute or University. The content of this thesis is the result of work carried out since the official commencement date of the approved research program.

Rick D. Franich

Acknowledgements

This thesis and the work described herein would not have been possible without the support and assistance of many people.

I would first like to sincerely thank my supervisors, Peter Johnston and Ian Bubb for their support and guidance throughout the duration of this work. Their support extended beyond academic supervision to include employment in various teaching and research capacities. These opportunities have been an important part of my career development and are greatly appreciated. Peter's continuous involvement in the entire project has been invaluable, and Ian's offer to interrupt retirement to offer advice on the thesis structure and to proof-read the final draft was most generous.

The experimental work conducted at ANSTO was made possible by the ever-helpful staff of the ANTARES accelerator laboratory, Nick Dytlewski, David Cohen and Reiner Siegler. Assistance from Dennis Mather and the staff at AINSE with travel and accommodation arrangements in Sydney was appreciated.

The experimental work in this project was supported by financial assistance from AINSE, and I was the recipient of an RMIT Postgraduate Research Scholarship without which I would not have embarked on this project.

I would like to thank Leszeck Wielunski, Sunni Lim, and Dae Won Moon, for providing samples which were used to generate experimental reference spectra. Peter Johnston, Mohamed El Bouanani and Warren Stannard supplied some of the experimental data used in this work. Warren Stannard developed the '*RDA_WBS'* software for graphical extraction of

elemental Time of Flight spectra from multi-parameter data files, and kindly updated it to suit new file formats adopted at ANSTO during this project.

Andrew Alves, Michael Taylor and Patrick Reichart conducted the measurements of ion transmission through nano-apertures. Sergey Rubanov performed the focused ion beam machining of the apertures in the silicon cantilevers. Both of these procedures were done at the Micro-Analytical Research Centre (MARC) at the University of Melbourne. Michael Taylor analysed the experimental data and generated the figures depicting the results and the corresponding energy plots for the simulation data. Michael also produced the Scanning Electron Microscopy images of the cantilevers. He claims he only broke a few!

Of course, there are people who help you get through something that takes this long, by being important in everything that *isn't* the project…

Alex Merchant for helpful advice on getting through (i.e. "abandoning") the thesis writing process, for many helpful, interesting and entertaining conversations, and for sharing a passion for teaching. Warren Toye, who is always thinking about the bigger picture, and John Watson of the MQRG, who is a connoisseur of "RMIT Gold".

Thanks to Mum and Dad for valuing that 'good education' and for being supportive and encouraging even though they probably never quite understood exactly what it was I was doing all this time.

And finally to my partner and best friend, Lynn, who saw the whole thing happen from enthusiasm to relief. My deepest thanks for being so supportive, letting me get away with helping very little at home, and for enduring the great imposition on *our* time. We are definitely overdue for a holiday.

Table of Contents

List of Figures

List of Tables

Abstract

Heavy Ion Elastic Recoil Detection Analysis (HIERDA) is a versatile Ion Beam Analysis technique well suited to multi-elemental depth profiling of thin layered structures and near-surface regions of materials. An existing limitation is the inability to accurately account for the pronounced broadening and tailing effects of multiple scattering typically seen in HIERDA spectra. This thesis investigates the role of multiple large angle scattering in heavy ion applications such as HIERDA, and seeks to quantify its contribution to experimental output. This is achieved primarily by the development of a computer simulation capable of predicting these contributions and using it to classify and quantify the interactions that cause them. Monte Carlo ion transport simulation is used to generate simulated HIERDA spectra and the results are compared to experimental data acquired using the Time of Flight HIERDA facility at the Australian Nuclear Science and Technology Organisation.

A Monte Carlo simulation code was adapted to the simulation of HIERDA spectra with considerable attention on improving the modelling efficiency to reduce processing time. Efficiency enhancements have achieved simulation time reductions of two to three orders of magnitude. The simulation is shown to satisfactorily reproduce the complex shape of HIERDA spectra. Some limitations are identified in the ability to accurately predict peak widths and the absolute magnitude of low energy tailing in some cases. The code is used to identify the plural scattering contribution to the spectral features under investigation, and the complexity of plurally scattered ion and recoil paths is demonstrated. The program is also shown to be useful in the interpretation of overlapped energy spectra of elements of similar mass whose signals cannot be reliably separated experimentally.

The effect of large angle scattering on the transmission of heavy ions through a nano-scale aperture mask, used to collimate an ion beam to a very small beam spot, is modelled using a version of the

program adapted to handle the more complex geometry of the aperture mask. The effectiveness of nano-aperture collimation was studied for a variety of ion-energy combinations. Intensity, energy, and angular distributions of transmitted ions were calculated to quantify the degree to which scattering within the mask limits the spatial resolution achievable. The simulation successfully predicted the effect of misaligning the aperture and the beam, and the result has subsequently been observed experimentally.

Transmitted ion distributions showed that the higher energy heavier ions studied are more effectively collimated than are lower energy lighter ions. However, there is still a significant probability of transmission of heavy ions with substantial residual energy beyond the perimeter of the aperture. For the intended application, ion beam lithography, these ions are likely to be problematic. The results indicate that medium energy He ions are the more attractive option, as the residual energy of scattered transmitted ions can be more readily managed by customising the etching process. Continuing research by experimentalists working in this area is proceeding in this direction as a result of the conclusions from this work.

Chapter 1

Introduction

Heavy Ion Elastic Recoil Detection Analysis is a versatile Ion Beam Analysis technique well suited to multi-elemental depth profiling of thin layered structures and near-surface regions of materials. An existing limitation of the technique is the inability to accurately account for the pronounced multiple scattering experienced by heavy ions penetrating matter. The primary objective of this work is to understand the role of multiple scattering in HIERDA and to quantify its contribution to output spectra. This will be achieved primarily by developing a computer simulation capable of predicting these contributions and using it to classify and quantify the interactions that cause them. This will help to realise the potential for HIERDA to be a very accurate and fully quantitative Ion Beam Analysis technique.

Energetic ions have been employed in a diverse range of scientific fields from materials science to medicine. At the heart of all of these applications are the interactions between ions and matter, which can be tailored to induce changes in the matter or to yield information about the sample being probed.

Energy transferred to matter by these ions can be used to alter structure at a sub-atomic level – locally changing the elemental composition, electronic bonding, or inducing nuclear reactions. Applications include altering material properties, nano-fabrication, and medical uses such as cancer treatment. Changes to the ions' kinetic energy and/or trajectory due to interactions with the sample provide valuable information regarding stoichiometry, molecular bonding and spatial distribution.

Similar information can also be provided by emissions from induced reactions or particles ejected from the sample after energy transfer from the incident ion. It is these abilities that have made ion beams such a valuable tool to materials scientists.

Materials science is an area of technology which is driving physics research. The field is rich with the development of novel materials with particular physical and chemical properties, and the design and manufacture of increasingly smaller structures for more energy efficient devices. Characterisation is important to the design, development, manufacture and assessment of these structures. Several classes of materials, for example semi-conductors, super-conductors, and opto-electronic devices, frequently feature very thin multi-layered structures. This requires analysis techniques with the ability to provide elemental depth profiles with high spatial resolution.

Many analysis techniques are available to materials scientists for the purpose of characterisation. The quantity or parameter being sought often prescribes the choice of analysis method, although there are frequently options available. Different techniques intended to extract similar information have strengths and weaknesses related to the quality of the information they are able to provide or the circumstances in which they may be used. These advantages and limitations may be related to the fundamental physics of the interactions involved or practical implementation issues.

Ion Beam Analysis (IBA) has consistently been a popular choice for analysing these types of structures. The probing of matter with beams of energetic particles has a long history, and some techniques are mature and widely used for routine analysis. Remaining limitations include the interpretation of output data. The accuracy and precision of measurements are influenced by the degree to which the physical reality of the measurement resembles the assumptions made in order to simplify the interpretation.

In Ion Beam Analysis, it is often assumed that each probing ion has a single interaction event. In some cases the assumption is valid to within tolerances imposed by other factors such as instrument

resolution. In other cases such as the IBA technique known as Heavy Ion Elastic Recoil Detection Analysis (HIERDA), multiple scattering of the primary incident ions and recoil atoms ejected from the target plays a significant role and must be properly accounted for to accurately interpret the experimental output. Current data analysis methods do not correctly incorporate these effects and the consequential inaccuracy and uncertainty is a significant shortcoming of this valuable technique.

1.1 Ion Beam Analysis

Ion Beam Analysis refers to a group of techniques which share a common feature: the structure or constituency of a material is analysed by a beam of charged particles generated by a particle accelerator. The ionisation of the particles enables acceleration by an electrostatic potential, and focussing of the beam by electromagnetic lenses. The beam of charged particles impinges upon a sample surface followed by the detection of interaction products which may be used to identify the interactions taking place and in some cases the locations of those interactions. Incident particles may be protons (H^+ ions), alpha particles (He^{2+} ions) or heavier ions. The products detected may be induced electromagnetic emissions such as x-rays and γ-rays, nuclear reaction products such as neutrons, the beam particles themselves having been scattered from the sample, or atoms ejected from the sample. The detected particles are usually energy analysed and in the case of recoil atoms, further scrutinised for species identification by means of charge, mass, velocity or energy loss rate determination. The various techniques are usually named for the combination of the incident particle used and the reaction product or particle detected.

Heavy Ion Elastic Recoil Detection Analysis (HIERDA) employs a beam of high energy heavy ions to eject nuclei from a target material. The recoiled nuclei can be identified for simultaneous quantitative compositional analysis, and energy analysed for depth profiles of individual elements.

In the last two decades, HIERDA has become established as an excellent 'all-round' technique. It combines many of the strengths of other well established IBA methods without some of their inherent limitations.

Earlier work at RMIT employed several Ion Beam Analysis techniques to the study of two classes of materials (i) compound semiconductor materials [1, 2], and (ii) high dielectric constant ferro-electric structures [3-5]. In recognition of particular limitations of some of the methods, the potential advantages of HIERDA were recognised as offering a means of more accurately characterising these important materials. The lack of a HIERDA specific formalism for analysing the output data became apparent when existing analysis software failed to correctly account for the pronounced multiple scattering effects of the technique.

1.2 Simulation Assisted Interpretation

There are few IBA experiments that can be performed for which the output is inherently quantitative or can be directly interpreted in terms of the structure of the sample being measured. The usual procedure for interpretation of output is an iterative process of simulation and matching.

The output spectrum of a proposed sample description is predicted by simulation and compared to the experimental output. Any differences are used to refine the proposed description and a new simulated spectrum is generated. The process is repeated until the two agree 'sufficiently well', at which point the model description is assumed to be a description of the sample being studied.

Analytical simulation methods are based on the premise that the simplest structure consisting of a single mono-elemental layer of uniform thickness, when analysed with an ion beam, will yield a predictable output spectrum. The spectra of more complicated structures can be predicted by combining the contributions of the constituent elements and layers.

HIERDA proved to be a difficult case, particularly due to the heavy influence of multiple scattering, where the analytical approach fails to accurately reproduce some spectral features. It was stated in the widely respected reference *Handbook of Modern Ion Beam Materials Analysis* [6] that a quantitative treatment of multiple scattering requires Monte Carlo simulation of each particle trajectory [7].

1.3 Development of Monte Carlo Simulation

As the fundamental interactions involved are stochastic processes, the Monte Carlo approach using randomly generated numbers to simulate statistical outcomes, was a natural choice. The Monte Carlo approach involves the simulation of individual ion trajectories including each interaction along the path through the sample. For the large number of ion trajectories required to represent an ion beam, this involves a *very* large number of calculations. The enormous amount of computational power required is recognised as an obstacle, and this approach has often been dismissed on that basis, particularly for routine analysis [7]. This is a result of the inherent inefficiency of most IBA processes – a large number of incident particles must be impinged on the target to get a statistically significant number of events occurring in the detector, which typically subtends a small solid angle at the sample.

Although evolutionary increases in readily available computing power are improving the situation, the magnitude of the task is considerable. While routine analysis of HIERDA by Monte Carlo methods may not yet be practical, the development of a Monte Carlo simulation code to study the multiple scattering effects in detail is possible. However, initial simulation times in the order of weeks to months of computer time indicated that significant efficiency improvements would be needed in the simulation process.

While the primary motivation for this work was to study the role of plural scattering in HIERDA, the development of a HIERDA simulation code became a major objective. The aims of (i) creating

a useable simulation code for routine analysis, and (ii) creating a tool suitable for studying plural scattering, are slightly at odds – an everyday code would most likely ignore lower probability, highly plural events in order to save processing time. This is the approach taken by Arstila and co-workers who have also applied Monte Carlo simulation to the interpretation of HIERDA spectra [8, 9]. The present plural scattering study necessitated inclusion of all such events no matter how low in probability in order to quantify them and their influence on experimental spectra.

A detailed reproduction of the paths of such ions allows a comprehensive analysis of those paths including the frequency, magnitude and energy transfer characteristics of the interactions involved. This characterisation may also be applied to the identification of indicator parameters which can be used to identify and classify them or to predict their occurrence. This information may in turn be exploited to improve processing efficiency, by limiting the simulation to the relevant ion paths of interest. Using this strategy, an efficient Monte Carlo simulation code has been developed and applied to the problem of modelling and quantifying the multiple small angle scattering, and less frequent large angle scattering which influences HIERDA measurements.

1.4 Ion Beam Collimation with Nano-apertures

Large angle scattering of ions is important in the collimation of ion beams using nano-apertures. A mask featuring a very small aperture is an alternative to beam focusing to achieve a small beam spot on target in IBA and in ion beam fabrication – the formation of three dimensional structures using ion beams. In IBA, localisation of the beam spot permits spatial resolution of the analysis. In ion beam fabrication, the spot size dictates the lateral scale of patterns or structures that can be formed. Beam localisation is achieved in one of two ways; by focussing the beam using electric or magnetic field lenses along the beam-line, or by collimation using an aperture, slits or scrapers.

Focussing to very small (sub-100 nm) beam spot sizes is technically challenging and expensive due to equipment requirements. By comparison, the use of apertures is relatively simple although not

without practical difficulties. These include the manufacture of very small (<100 nm) regularly shaped apertures in a mask which is otherwise opaque to the beam, and the positioning of apertures relative to beam and sample.

The effectiveness of very small apertures for the collimation of energetic ions is limited by the scattering of ions from the walls of the aperture and the partial transparency of all materials to MeV ions. Thus the spatial resolution of the collimator will be effectively limited by the ion scattering which occurs in the material of the nano-aperture mask.

This ion beam scattering problem clearly has features in common with the multiple scattering complications experienced in HIERDA analysis. Individual irregular ion paths are relevant, and treatment of the ion beam as a continuous distribution is inappropriate. It was a natural choice to apply Monte Carlo ion transport simulation to investigate the transmission of ions through nano-apertures.

1.5 Thesis Scope and Structure

The primary aim of this work was to study the role of multiple scattering in HIERDA and to be able to calculate its contribution to experimental spectra. This would allow the accurate simulation of experimental output for the purpose of qualitative analysis of results. Of particular interest were those ion paths featuring more than one large angle scattering event – so called "plural scattering". It is these events, which are not properly considered in current data analysis methods, that make the output spectra complex and difficult to fit by analytical simulations.

Monte Carlo (MC) simulation was clearly the appropriate tool for reproducing these events in sufficient detail for study. The development of a MC code that allowed the simulation of complete HIERDA spectra had obvious advantages – the output could be validated against experimentally obtained data and the resulting computer code could potentially be a valuable tool for general

interpretation of experimental data. Thus the development of a Monte Carlo HIERDA simulation code became central to the project.

The processing time cost of MC simulation was a foreseen obstacle. Strategies for significantly improving the efficiency of the modelling needed to be developed. As the aim was to study plural scattering contributions to spectra, efficiency enhancements could not simply be at the expense of low probability events being ignored. Thus the resulting program may not necessarily be fast enough for routine data analysis, but simulation times are short enough to make representative sample studies practicable. The MC code could then be applied to several problems involving ion beam scattering and be shown to be a useful technique for addressing problems intractable by other methods.

In Chapter 2, the HIERDA technique is described in detail, including the attributes which make it such a valuable technique, and the underlying physics which lead to the complications being addressed in this work. The technique is discussed in the context of alternative IBA methods and the extent to which existing data interpretation methods fail to satisfactorily handle the pronounced multiple scattering effects inherent in HIERDA.

Chapter 3 contains a description of the specific HIERDA experiments used in this work. The Heavy Ion Time of Flight facility of the ANTARES accelerator at ANSTO was used to obtain the experimental reference spectra required for validation of simulation output. The experimental apparatus is described and sample results presented to illustrate the issues being addressed.

MC simulation of ion transport is introduced in Chapter 4. Approximations used to simplify the modelling are described together with the specific requirements for its adaptation to HIERDA simulation with a Time of Flight – Energy detector and the generation of simulated spectra. The successful application of the MC code is demonstrated for two fundamental cases:

(i) a HIERDA measurement of a uniform mono-elemental layer of high Z material to illustrate the reproduction of multiple scattering features, and

(ii) a HIERDA measurement conducted such that the detector is positioned beyond the critical angle for single scattering of the incident ions. In this situation, *all* detected scattered ions are *plurally scattered*. That is, they have suffered more than one large angle scattering event.

Chapter 5 contains descriptions of all of the efficiency enhancements implemented in the MC code. These include efficient programming strategies, modelling approximations, exploiting limitations imposed by the experimental configuration and a detailed analysis of scattering in ion paths. This latter investigation provides the understanding of the frequency and magnitude of significant scattering events which is the main aim of this work, and also offers a useful avenue for improving the efficiency of simulation.

Multiple and plural scattering are addressed in Chapter 6. An appropriate definition of plural scattering is described and a "degree of plurality" introduced. The MC code is used to quantify the contribution of plurally scattered ions and recoils to output spectra. Sample spectra are presented with segregated contributions from plural scattered particles of different degrees. Path complexity of plural scattered atoms is discussed.

In Chapter 7, the MC simulation is applied to the problem of overlapping signals in HIERDA. Finite mass resolution of detection systems results in some similar mass isotope signals being inseparable. The spectral contributions can be separated in the simulation, providing information which can be helpful in the analysis of experimental data.

Finally, in Chapter 8, Monte Carlo simulation of large angle ion scattering is applied to the general problem of ion beam collimation using small apertures. It is shown that Monte Carlo simulation can be used to investigate the extent to which the scattering of ions in an aperture mask limits the effectiveness of a collimator.

1.6 Publications Arising From This Work

Copies of manuscripts are included in Appendix A

1. Johnston, P.N., Franich, R.D., Bubb, I.F., El Bouanani, M., Cohen, D.D., Dytlewski, N., and Siegele, R., *The Effects of Large Angle Plural Scattering on Heavy Ion Elastic Recoil Detection Analysis.* Nuclear Instruments and Methods in Physics Research Section B: Beam Interactions with Materials and Atoms, 2000. **161-163**: p. 314-317.

2. Franich, R.D., Johnston, P.N., Bubb, I.F., Dytlewski, N., and Cohen, D.D., *Efficiency Enhancements to Monte Carlo Simulation of Heavy Ion Elastic Recoil Detection Analysis Spectra.* Nuclear Instruments and Methods in Physics Research Section B: Beam Interactions with Materials and Atoms, 2002. **190**(1-4): p. 252-255.

3. Franich, R.D., Johnston, P.N., and Bubb, I.F. *The Paths of Plurally Scattered Ions in Heavy Ion Elastic Recoil Detection Analysis.* in Application of Accelerators in Research and Industry: 17th International Conference on the Application of Accelerators in Research and Industry. 2003. AIP. **680**. p. 385-388

4. Johnston, P.N., Bubb, I.F., Franich, R., Cohen, D.D., Dytlewski, N., Arstila, K., and Sajavaara, T. *Scattering of Ions Beyond the Single Scattering Critical Angle in HIERDA*. in Application Of Accelerators In Research and Industry: 17th International Conference on the Application of Accelerators in Research and Industry. 2003. AIP. **680**. p. 460-463

5. Franich, R.D., Johnston, P.N., and Bubb, I.F., *Efficient Monte Carlo Simulation of Heavy Ion Elastic Recoil Detection Analysis Spectra.* Nuclear Instruments and Methods in Physics Research Section B: Beam Interactions with Materials and Atoms, 2004. **219-220**: p. 87-94.

6. Taylor, M.L., Franich, R.D., Alves, A., Reichart, P., Jamieson, D.N., and Johnston, P.N., *Ion Transmission through Nano-Apertures.* Nuclear Instruments and Methods in Physics Research Section B: Beam Interactions with Materials and Atoms, 2006. **249**(1-2): p. 752-755.

7. Taylor, M.L., Alves, A., Reichart, P., Franich, R.D., Rubanov, S., Johnston, P.N., and Jamieson, D.N., *Ion Beam Lithography Using a Nano-Aperture.* Nuclear Instruments and Methods in Physics Research Section B: Beam Interactions with Materials and Atoms, (Accepted for publication September 2006, *Article In Press -Proof avail online Feb. 2007*).

Chapter 2

HIERDA and other Ion Beam Analysis Techniques

In this chapter, Heavy Ion Elastic Recoil Detection Analysis (HIERDA) will be described for the purpose of understanding the limitations being addressed in this work. Some comparisons will be made with other techniques in common usage for stoichiometric analysis and depth profiling of thin films and surface regions. This will highlight the broad usefulness of HIERDA and demonstrate the importance of studying multiple scattering, which has a significant influence on experiments conducted using this technique. Multiple scattering as it applies to HIERDA will be described, and work done to date on this issue will be reviewed.

2.1 Ion Beam Analysis

The concept of probing matter with charged particles is popularly traced back to its roots in 1909 in the famous experiments of Gieger and Marsden whose alpha particle scattering experiments lead to Rutherford's model of the atom. The development of the first electrostatic ion accelerator and its application to nuclear physics by Van de Graaff, Cockroft and Walton in the late 1920's and early 1930's laid the foundations for the use of ion beams in physics.

Contemporary implementation employs a particle accelerator to produce a beam of protons, alpha particles or heavier ions to probe a sample. Scattered incident ions, recoiled target atoms, or

induced atomic and nuclear reaction products are interrogated for information regarding the sample. The choice of technique(s) used will ideally be based upon the strengths or weaknesses of each technique relative to the required information. However, practical issues such as availability, analysis time, and cost may also be important considerations. When several outcomes are sought, multiple measurements with different methods may be preferred, although a single technique which features the best compromise between relevant factors may be attractive.

Within these considerations, HIERDA can be shown to have an important role amongst other mature and very widely used techniques such as Rutherford Backscattering Spectrometry (RBS) and Proton Induced X-ray Emission (PIXE), and more specialised methods such as Nuclear Reaction Analysis (NRA) and Secondary Ion Mass Spectrometry (SIMS). In general, different IBA techniques are considered *complementary* rather than *competing* options. Material analyses frequently feature measurements performed using two or more techniques on the same samples to most accurately describe different quantities, or to provide confidence in results obtained. HIERDA has been shown to feature several strengths of other techniques, with few of the associated weaknesses, and has been described as a potentially 'universal' analysis method by many authors including Barbour and Doyle [10], Assmann et al. [11], Forster et al. [12], and Davies et al. [13]. This is in recognition of the ability to provide stoichiometric analysis and depth profiles of all elements simultaneously. The improvement of data interpretation and analysis, by fully quantifying the effects of multiple scattering is an important part of realising this potential.

Following convention, the term *ion* will generally be used to refer to the incident projectile, and *recoil atom* to refer to a target atom ejected from its initial position in the sample. The description given here is based on that of Barbour and Doyle [10] which focuses on conventional ERDA using He ions for H profiling, and is extended here with emphasis on Heavy Ion ERDA.

2.2 Heavy Ion Elastic Recoil Detection Analysis

Depth profiling of light elements in heavy matrices via the detection of recoils ejected from a sample under ion bombardment, was first reported by L'Ecuyer et al. in 1976 [14]. The technique has since become widely known as Elastic Recoil Detection Analysis (ERDA or ERD) or Recoil Spectrometry. ERDA is now widely used for depth profiling of light elements, an area of limitation for RBS, and in particular for hydrogen profiling which cannot be done with RBS, and is very time consuming using NRA.

The extension of ERDA using very heavy ions capitalises on its advantages over other techniques and can improve sensitivity, depth resolution, and mass resolution (discussed in section 2.3). Sample elements with a wide range of masses can be analysed simultaneously and unambiguously. This makes HIERDA a powerful tool for determining quantitative depth profiles for complex materials and structures. The fundamental concepts in HIERDA are described below.

2.2.1 Basic Principles

HIERDA uses a beam of heavy ions to probe a sample by causing the ejection of energetic recoil atoms from the sample. The recoil atoms are detected and analysed for mass and energy to provide elemental and depth information. The number of recoils of different species detected is related to the stoichiometry of the sample. Two particle collision kinematics govern the energy transfer in the binary collision that dislodges the recoil atom. The difference between measured and expected recoil energy for known particle masses and scattering angles, is attributable to energy lost by the ion and recoil traversing the sample and indicates the depth of the scattering event.

The schematic of the experimental set-up is shown in Figure 2.1. The typical grazing angle of incidence and detection is shown. This facilitates the detection of more forwardly scattered recoils which have higher energy, and enhances the depth resolution by amplifying the path lengths through the sample. A scattering event occurring at a depth, x, will feature a path length of $x/\cos(\alpha)$

for the ion prior to the collision, and also for the resulting recoil in the case of symmetric incident and exit angles. Note that the incident and recoil angles need not be symmetrical, and asymmetry may be used to enhance recoil yield in certain situations.

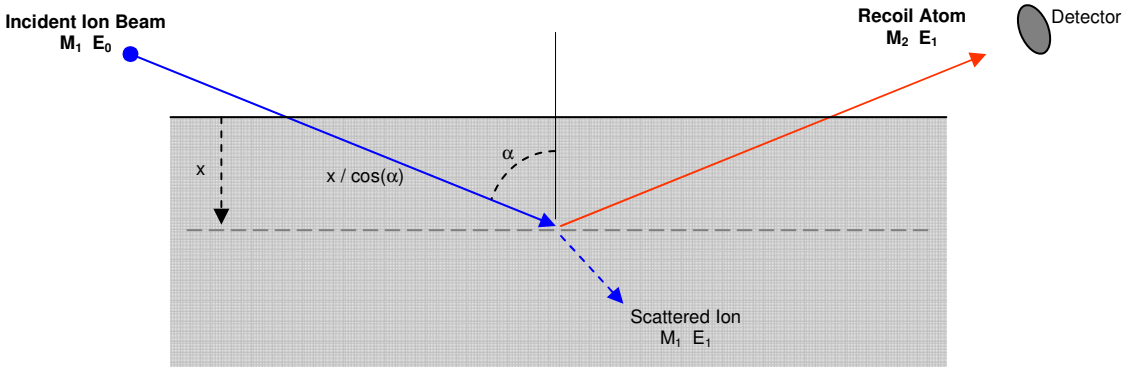

Figure 2.1 HIERDA Experimental Geometry

In conventional H profiling with ERDA, light ions such as He are used to recoil H atoms from the sample which are detected using a silicon energy detector. A thin absorber foil stops scattered He ions, and other recoil species, from reaching the detector. The energy spectrum of detected H ions provides the H depth profile. In Heavy Ion ERDA, heavier mass recoils may be produced, and a two-parameter detection system may be used to enable mass discrimination of recoiled nuclei. Individual elemental energy, and hence depth, profiles are obtained simultaneously.

HIERDA depends upon the following concepts which are described in detail below:

- The energy transfer between a projectile ion and a target nucleus in a binary collision;
- The differential scattering cross section which gives the probability for the scattering event to occur;
- Energy loss of the incident ion and recoil atom as they traverse the sample; and
- Detection and identification of recoil atoms ejected from the sample (and in some cases, scattered incident ions).

2.2.2 Energy Transfer in a Binary Collision

Consider the collision between an incident ion of the analysing beam, and a stationary atom of the sample, as illustrated in Figure 2.2. The incident ion is deflected from its original trajectory by an angle, θ. A kinetic energy ΔE is transferred to the target atom dislodging it from its position in the target matrix if $\Delta E > E_D$, the displacement energy of the target atom. The struck atom *recoils* with energy ΔE at an angle ϕ to the original direction of the incident ion which continues along its new trajectory with energy $E' = E_0 - \Delta E - E_D$ where E_0 denotes the ion energy immediately prior to the collision.

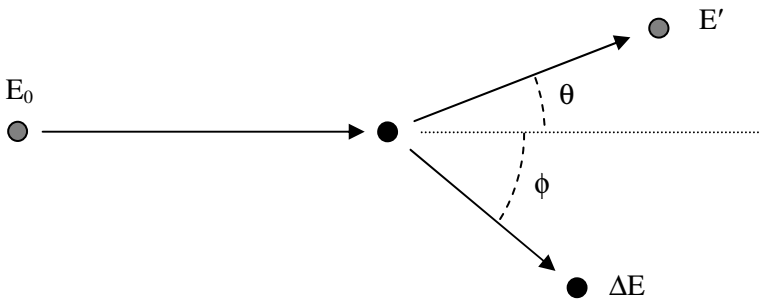

Figure 2.2 Scattering of an ion with incident energy E_0 from an initially stationary target atom, showing the ion scattering angle, θ, and the recoil angle, ϕ. The struck atom recoils with transferred energy, ΔE.

HIERDA experiments are normally conducted under conditions involving elastic collisions at energies where relativistic effects may be neglected. Solving the equations for the conservation of energy and momentum for this binary scattering event yields the following relationships between the energy transferred in the collision, and the resulting trajectories of the two particles.

For the scattered incident ion, the *kinematic factor for scattering*, K, describes the fraction of the incident ion kinetic energy, E_0, retained by the scattered ion:

$$K = \frac{E_1}{E_0} = \left[\frac{M_1 \cos\theta \pm \left({M_2}^2 - {M_1}^2 \sin^2\theta \right)^{1/2}}{M_1 + M_2} \right]^2 \tag{2.1}$$

For the recoiling target atom, the *kinematic factor for recoiling*, Λ, describes the fraction of the incident ion kinetic energy, E_0, transferred to the recoiled target atom:

$$\Lambda = \frac{E_2}{E_0} = \frac{4M_1M_2}{(M_1 + M_2)^2}\cos^2\phi \tag{2.2}$$

where

E_1	kinetic energy of the ion after scattering
E_2	kinetic energy of the recoil after scattering
θ	scattering angle of ion
ϕ	scattering angle of recoil
M_1	atomic mass of ion
M_2	atomic mass of recoil

The kinematic equations are equivalent to those for two hard spheres of differing masses; the energy transfer and scattering angles are dependent upon the mass ratio of the two particles. For the case $M_1 > M_2$ the kinematic factor for scattering, K, is double valued, and the scattering angle for the projectile, θ, is limited to

$$\theta_c \leq \sin^{-1}\left(\frac{M_2}{M_1}\right) \tag{2.3}$$

where θ_c is called the *critical* angle for scattering. This maximum scattering angle can be used experimentally to exclude scattered incident ions from reaching the detector. As will be shown later, it can also be exploited in the study of multiple scattering by allowing the experimental detection of purely multiply scattered ions.

2.2.3 Scattering Cross Section

The determination of elemental stoichiometry is one of the primary objectives of a HIERDA measurement. The recoil yield is related to the relative concentrations of the target constituent

elements, and these may be extrapolated by adjusting the absolute yields by the ratio of the cross sections for scattering of each of the recoil species into the solid angle of the detector.

The forces acting during the collision between the incident ion and the target atom are, in many cases, well described by the Coulomb repulsion between the two nuclei. For two-body Coulomb scattering, the recoil production probabilities are given by the Rutherford Cross Section:

$$\frac{d\sigma}{d\Omega} = \frac{[Z_1 Z_2 e^2 (M_1 + M_2)]^2}{(2M_2 E_0)^2 \cos^3 \phi} \tag{2.4}$$

where

E_0	is the energy of the incident ion immediately prior to scattering
ϕ	is the recoil scattering angle in the laboratory frame
Z_1, Z_2	are the atomic numbers of the incident and recoil ions respectively
M_1, M_2	are the atomic masses of the incident and recoil ions respectively
e	is the electronic charge

The corresponding Rutherford differential cross section for the scattered incident ions in the laboratory frame of reference is:

$$\frac{d\sigma}{d\Omega} = \left(\frac{Z_1 Z_2 e^2}{4E_0} \right)^2 \frac{4\left[\sqrt{M_2{}^2 - M_1{}^2 \sin^2 \theta} + M_2 \cos\theta \right]^2}{M_2 \sin^4 \theta \sqrt{M_2{}^2 - M_1{}^2 \sin^2 \theta}} \tag{2.5}$$

As higher energy projectiles are used to increase probing depth, there is an increased likelihood that scattering cross sections may become non-Rutherford (see Figure 2.3). The incident and target nuclei may get sufficiently close that they interact via the nuclear force in addition to the Coulomb force, and nuclear reactions may occur. HIERDA experiments are generally conducted within parameters that ensure this condition is avoided.

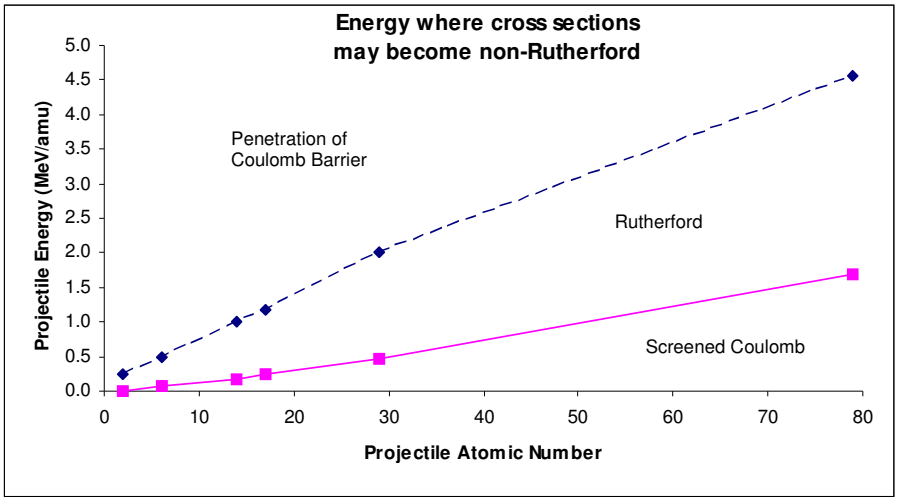

Figure 2.3 Energy regimes where scattering Cross Sections may become non-Rutherford – above the dashed line the projectile may penetrate the Coulomb barrier; below the solid line there may be significant screening of the nuclear charge (graph adapted from [6]).

The dependence of the Rutherford cross section on the nuclear charge, Z_i, of the colliding atoms will be influenced by electronic *screening* of the nuclear charge by electrons carried with the projectile, and those of the target atom. The degree of screening depends upon the distance of closest approach of the ion to the target atom in the binary collision which is in turn a function of the incident ion energy.

Electronic screening will be more significant at lower energies where the ion may capture additional electrons, and less so at high energies where it is likely to be stripped of its electrons. The charge state of high energy heavy ions in matter is not easily measured and is, in general, not well understood. However, the distance of closest approach of the ion to the target atom in the most significant collisions is very small. The ion and atom are inside each other's electron cloud, and the screening is only due to those electrons whose orbits lie between the nuclei. Thus the presence or absence of outer or weakly bound electrons has little influence for the high energy heavy ions of the typical HIERDA analysing beam. The gross detail of the ion path is dominated by these close collisions with small impact parameters, and the screening influence is small.

By conducting experiments under conditions which preserve Rutherford cross sections as closely as possible, HIERDA may be regarded for practical purposes, as an inherently quantitative technique.

2.2.4 Electronic Energy Loss

Energy loss as a function of path length is a critical parameter of the IBA methodology. It is this association that yields the depth profile information which is one of the main objectives of the measurement.

An ion penetrating matter will lose energy to atomic electrons of the sample in a large number of inelastic collisions along its path. Due to the large mass ratio between an ion and an electron, the individual energy transfers are small and directional deviations for the ion may be neglected. Thus, to a very good approximation, electronic energy loss may be considered a continuous process between the relatively rare nuclear scattering events. Nuclear scattering also contributes to the energy loss of moving ions in matter. While it is the dominant process at very low energies (eg. a few 10's of keV), it has a minor influence at the typical energies used in HIERDA measurements which are in the order of 1 MeV/amu.

The energy loss *rate* of an ion passing through matter is known as *stopping power*, (or more recently *stopping force* [15, 16] to maintain consistency with units – although *stopping power* is still the most widely used expression). Stopping power is a function of the ion species, energy and charge state and of the composition and density of the target medium.

The theoretical consideration of the interactions involved in electronic energy loss, is a complex field which has been the subject of a great deal of study for over a century due to its significance in many fields. Detailed reviews are available in [17] and [18]. Simple analytical models have been developed from observed data for application to ion beam analysis.

At ion velocities greater than the Bohr velocity of atomic electrons, the electronic energy loss is assumed to be proportional to the square of the ion charge. The energy loss per unit length is well described by the Bethe-Bloch formula:

$$\frac{dE}{dx} = NZ_2\left[\frac{4\pi(Z_1e^2)^2}{m_e v_1^2}\right]L \tag{2.6}$$

where N is the atomic density, m_e is the electron mass, and v_1 is the ion velocity. L is called the *stopping number* and is given by

$$L = \ln\left(\frac{2m_e v_1^2}{I}\right) \tag{2.7}$$

where I is an average over the excitation and ionisation energies of the electrons in the target. Bloch showed that I was proportional to Z_2, with the coefficient of proportionality determined empirically to be approximately 10 eV.

The Bethe-Bloch formula applies at high velocities when the ion is fully stripped of its electrons. To extrapolate to the intermediate region where the ion is only partially stripped, a velocity proportional effective charge may be incorporated into Equation 2.5.

A quantity related to the stopping power is the *stopping cross section*,

$$\varepsilon = \frac{1}{N}\frac{dE}{dx} \tag{2.8}$$

Using the stopping cross section, the Bragg additivity rule can be defined for stopping in a compound, A_xB_{1-x} :

$$\varepsilon_{AB} = x\varepsilon_A + (1-x)\varepsilon_B \tag{2.9}$$

The Bragg rule assumes that the interaction between an ion and a target atom is independent of the surrounding target atoms. The chemical and physical state of the target material usually has a

negligible effect on the energy loss, however corrections can be made for some compounds where deviations in the order of 10 % can be found.

The stopping of heavy ions may be scaled against those for light ions using the *heavy ion scaling rule*:

$$\varepsilon_{HI} = \varepsilon_H Z_{HI}^2 \gamma_{HI}^2 \tag{2.10}$$

where ε_{HI} and ε_H are the heavy ion and proton stopping cross sections respectively, and γ_{HI} is the fractional velocity-proportional effective charge of the ion. There are several effective charge formulations described in [17] and [18]. The following expression is from Ziegler [19],

$$\gamma_{HI} = 1 - e^{-A}\left(1.034 - 0.177e^{\left(-0.08114 Z_{HI}\right)}\right) \tag{2.11}$$

with the fitting parameters given by

$$A = B + 0.0378 \sin(\pi B / 2) \tag{2.12}$$

$$B = 0.1772\, E_{HI}^{1/2}\, Z_{HI}^{-2/3} \tag{2.13}$$

Formulations for stopping powers are dependent upon experimental data and there are many combinations of ion, energy and target to be measured. Although the number of experimental studies on energy loss has been described by Rauhala as “overwhelming” [18], most of the work done in this area has focused upon stopping of light ions (H and He). These light ions have been used for many years as the probing beam of the well developed RBS technique [20]. Increased attention on the need for accurate data for heavier ions has lead several groups [21-23] to develop improved methods for efficiently collecting broad data sets across a continuous energy range. A large body of experimental data has been compiled by Hubert Paul for access via an internet website [24]. The 25,000 experimental data sets upon which SRIM relies is similarly available online [25]. Other collections are listed by Rauhala in [18]. The experimental data needs to be readily incorporated into calculations and to this end attempts have been made to fit empirical expressions to these data sets e.g. [16, 26, 27]. While the number of heavy ion stopping

measurements is growing, they still represent a small fraction of the available stopping data [28] and exhibit significant variability. Weijers et al. examined the data of the Paul database for the purpose of developing a simple empirical formula for the fast calculation of stopping powers for all ion species [16]. They have identified the existence of stopping powers measured by different groups for the same system, which differ by up to 50 %. They have compared the quality of their fitted function to that of other stopping power predictors compiled by Paul and Schinner [29]. The quality indicators used were the average normalised difference and distribution standard deviation, σ, between the predictor and each experimental value. The results are summarised in Table 2.1 for a subset of the data presented in [16] and [29], restricted to ions with energy from 0.1 to 1.0 MeV/amu stopping in elemental solid targets.

Table 2.1 The average normalised difference between measured data and calculated values for various stopping power predictors, for ions with energies of 0.1 – 1.0 MeV/amu stopping in solid elemental targets.

Predictor	***Type***	***Z_1***	***Avg. Normalised difference* (%)***
SRIM [30]	Program	3-18	-0.9 ± 8.7
		19-36	-0.9 ± 7.3
MSTAR [26]	Program	3-18	-1.4 ± 8.5
Northcliffe-Schilling [31]	Tables	3-18	-2.0 ± 11
		19-36	-4.1 ± 8.5
Weijers et al. [16]	Formula	2-92	-0.95 ± 9.7

**(measured-calculated)x100/measured. Data reproduced from Weijers et al. [16]*

The small average systematic error of 0.9 % - 4.1 % indicates that the overall fit of these methods is quite good and follows the shape of the stopping data curves. The significant random error, having standard deviations of 7.3% - 11 %, indicates the degree to which the experimental data are distributed around the mean values close to the curves. For example, Weijers' random error of σ= 9.72 % shows that their function lies within ± 19.4 % of 98 % of the experimental data points.

The spread of measured stopping data can be seen in light ion – heavy target systems for which there are many measurements. An example (He stopping in Au) is shown in Figure 2.4 which is taken from the Ziegler database [25].

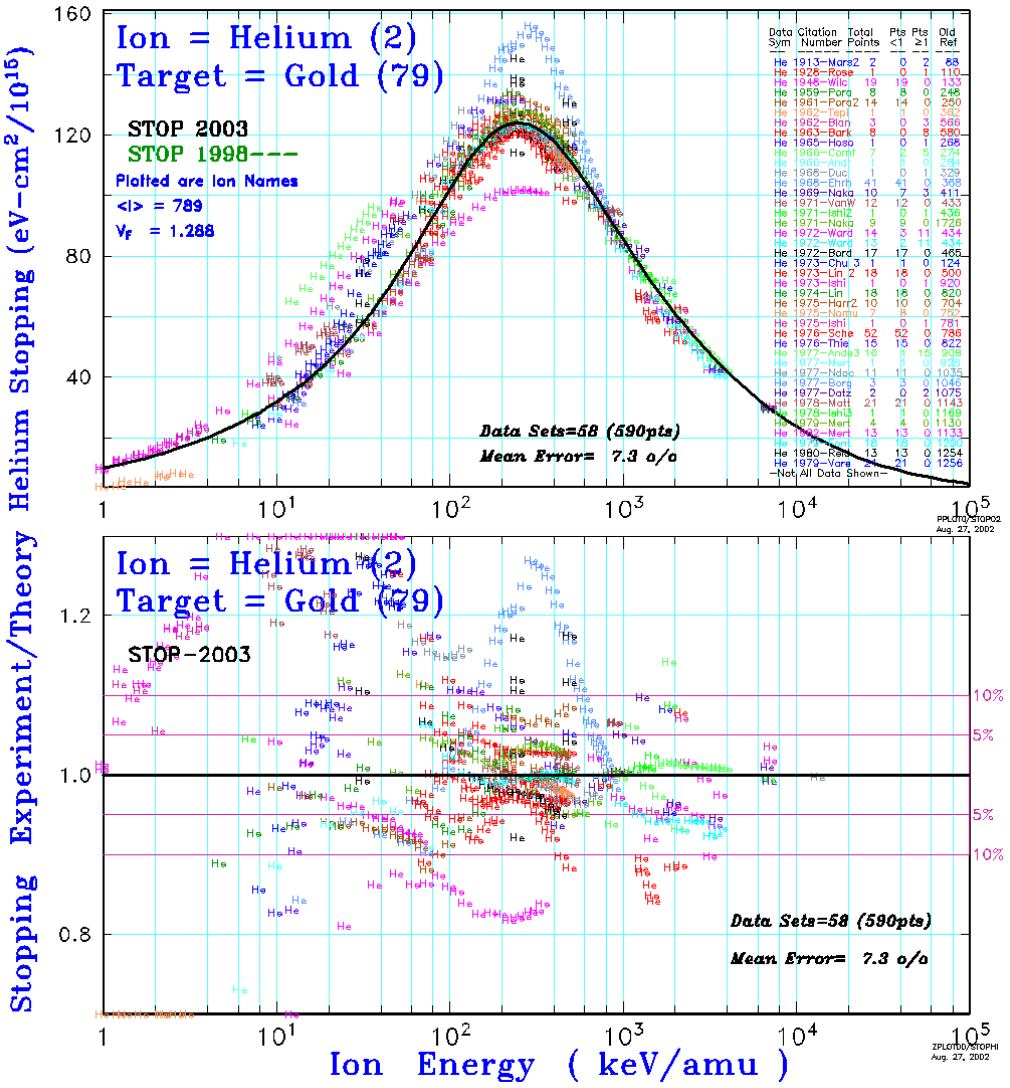

Figure 2.4 Measured stopping powers for He stopping in Au (above) and relative to SRIM prediction (below) illustrating variability of experimental data (see text). Data reproduced from [25].

The stopping of iodine and gold in a gold target are relevant to the present work and are discussed in Chapter 4. The Paul database identifies the availability of just 5 and 2 published data sets respectively. One of the Au in Au data sets involving only GeV ions is not relevant to HIERDA

applications and is not considered here. These data are shown in Figure 2.5. The SRIM-2006 [30] calculations are included for comparison. The scarcity of experimental data is illustrated, and the uncertainty in the I in Au data is evident – differences of up to ~25 % between measurements can be seen.

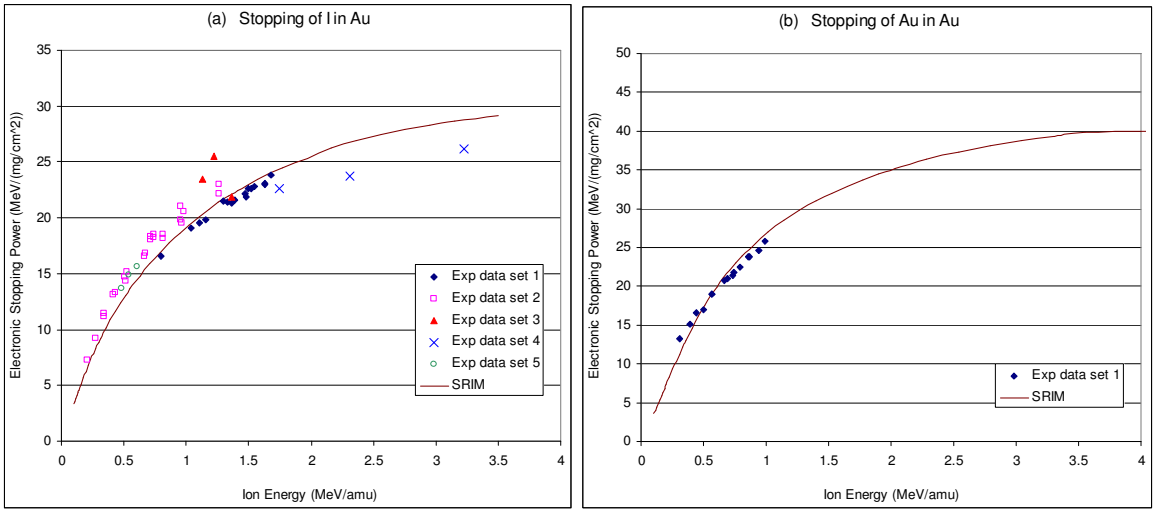

Figure 2.5 Experimental stopping power data for (a) I in Au, and (b) Au in Au. Solid curves are SRIM calculations. Experimental data extracted from [24]

It will be shown in Chapter 4 that a significant correction to the SRIM estimated stopping power for I in Au is required to match simulations with experimental spectra. Similar deficiencies in tabulated and calculated stopping powers have been reported by Timmers et al. [32] for ions in Au, and by Elliman et al. [33] for other systems, where corrections of up to 30 % were required to enable accurate simulation.

For accurate interpretation of data from ion beam analysis measurements involving heavy ions, more experimental data is needed, and accurate theoretical representation required. In general, heavy ion stopping powers are still regarded as poorly known.

2.2.5 Energy Straggling

The energy loss processes discussed in the previous section are in reality due to discrete interactions, and are therefore subject to statistical fluctuations due to the uniqueness of individual ion histories. As a result, the energy distribution of the ion beam broadens as the medium is traversed. This spreading of the beam energy is called *energy straggling*. In ion beam analysis, the broadening of measured energy distributions impairs depth and mass resolution, which deteriorate with increasing depth.

At the ion energies typical in HIERDA, the individual energy transfers to target electrons are very small compared to the width of the total energy loss distribution. Under these conditions, the distribution is approximately Gaussian, and Bohr's theory may be applied:

$$\Omega_B^2 = \frac{e^4}{4\pi\varepsilon_0} Z_1^2 \, Z_2 \, Nt \tag{2.14}$$

where Ω_B^2 is the variance of the energy loss distribution, and Nt is the areal density of the target. The condition for the Gaussian distribution was formulated by Besenbacher et al. [34] as

$$Nt \geq 2x10^{20} \, \frac{1}{Z^2} - \left(\frac{E}{Z_1} \right)^2 \tag{2.15}$$

where the energy of the ion, E, is in units of MeV/amu. The Gaussian approximation fails for thick targets where the energy loss during penetration exceeds 25 %.

2.2.6 Recoil Detection

Several detector options exist for ERDA measurement systems. In the simplest case such as light ion ERDA systems for H profiling, an energy detector (e.g. a Si surface barrier detector) is used with a range foil sufficiently thick to stop scattered incident ions from reaching the detector. In this configuration, all detected particles are assumed to be recoiled H, and the energy spectra are processed to yield H depth profiles.

In general when using heavier incident ions, recoils of any mass (within the limits imposed by the choice of incident ion species and energy) can be recoiled into the detector. A range foil may still be used to exclude recoils above a given mass, and energy differential may be used to distinguish recoil species based on the kinematics of the experimental configuration. Mass-depth ambiguity remains in the context that recoils of different mass originating at different depths in the sample may be detected with the same energy.

Thus the ideal detection system should be mass or charge dispersive in addition to measuring energy. Two-parameter systems meeting these criteria have been employed, and are usually one of two basic types: (i) Time of Flight and Energy (ToF-E) which are mass resolving; and (ii) Energy loss and Energy (ΔE-E) which are nuclear charge resolving. The Time of Flight and Energy detection system used in this work is discussed here, and specific experimental details are described in Chapter 3.

2.2.7 Time of Flight Recoil Spectrometry

The ToF-E telescope measures a particle's velocity before its energy is measured by a Si surface barrier detector. This is achieved by measuring the time taken for a detected particle to traverse the known distance between the time pick-offs of the telescope. Thus the ToF-E telescope is mass dispersive, using the following simple relationship between the flight time, T, and the measured energy, E:

$$E = \frac{M_2}{2}\left(\frac{L}{T}\right)^2 \tag{2.16}$$

where M_2 is the mass of the particle and L is the flight length of the telescope. Relativistic corrections are negligible at typical HIERDA energies. A typical ToF-E HIERDA system is depicted in Figure 2.6.

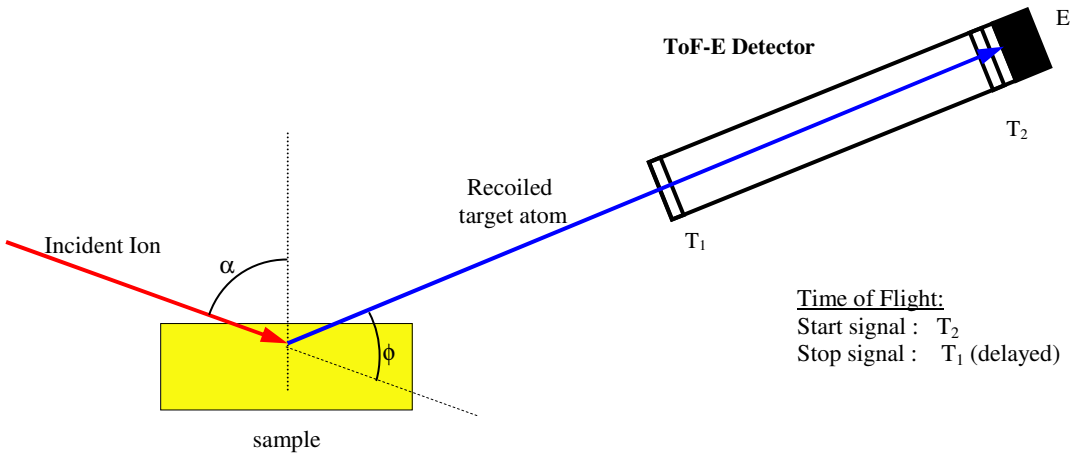

Figure 2.6 ToF-E detector arrangement for HIERDA showing time pick-offs T_1 and T_2, and Si surface barrier energy detector, E.

ToF-E HIERDA systems have been used and developed by several research groups including, for example, those in Sweden [35], Finland , France [36], Germany [37], Canada [38, 39], USA [40], Japan [41], Slovenia [42], Belgium [43], and Australia [44].

The main advantages of ToF-E recoil detection systems are (i) excellent depth resolution, and (ii) recoil mass resolution over a wide range of energies. The depth resolution obtainable with ToF ERDA is improved by converting the Time spectra to Energy spectra for depth profiling, and using the Si energy detector as the mass dispersive element [10]. The improvement in depth resolution arises because the resolution of the timing system is better than the energy resolution obtainable with surface barrier detectors [45-47]. These semiconductor detectors also suffer an energy broadening effect, referred to as the 'pulse height deficit', due to some of the energy being deposited in the detector as atomic displacements rather than purely the production of electron-hole pairs [10]. This effect is ion species and energy dependent, as is the resulting pulse height shift as the energy response of the detector changes due to the heavy ion irradiation damage [48]. The use of Time spectra to generate Energy spectra also allows for a far simpler direct calibration procedure, as described in Chapter 3 and by Stannard et al. in [3].

As a result of the poor energy resolution of Si detectors for heavy ions, ToF-E detectors experience reduced mass resolution for very heavy elements. This may be partially compensated for by using increased energies, for which the energy resolution of Si detectors improves [45]. Mass discrimination is effective down to significantly lower energies than for gas detectors. This allows for larger probing depths, particularly for heavy recoils, as recoils from greater depths have lower energy. It also enables HIERDA to be performed on smaller accelerators with lower terminal voltages, which are more widely available, as shown by Grigull et al. [37].

The main alternative to ToF-E detectors is the "ΔE-E" type of detection systems. These measure the *energy loss rate* of a particle through the detection medium before registering the total residual energy. The energy loss rate is a function of nuclear charge, *Z*, of the particle. Provided the particle energy is above the maximum ("Bragg Peak") of the stopping power curve (generally in the order of 1 MeV/amu), this can be used to identify the recoil element. This requires the use of higher energy, heavier incident ions to maintain the higher recoil energies [37].

Position sensitive, gas ionisation ΔE-E detectors, such as those used at the Australian National University [32] and the University of Munich [49], permit the use of large detector solid-angles with corrections for kinematic energy spread [11]. The improved efficiency of large solid-angle detectors allows shorter measurement times which reduce sample irradiation damage and 'beam-time' costs [11, 32, 48, 50, 51].

Gas detectors with continuous flow-through gas are insensitive to cumulative effects of radiation damage [52] and can be more sensitive to recoil identification for light ions than ToF-E systems [49]. Non-linear energy response [16] (as for Si detectors) and limited mass differentiation for isotopes of heavy elements remain as limitations in the application of ΔE-E detectors in HIERDA.

2.3 Advantages of Using Heavy Ions

The original recoil spectrometry experiments by L'Ecuyer et al. [14] actually used quite heavy ions, ^{35}Cl, at 1 MeV/amu and so were in effect HIERDA experiments. ERDA using light ions came later. The ability to profile light elements in heavy materials was the primary use, being an area of difficulty for RBS. Hydrogen profiling in particular was a top priority as it cannot be done using backscattering techniques, and is quite complex using NRA or SIMS. Light element profiling only requires beam ions heavier than the elements to be analysed, and H profiling can be done with He ions as demonstrated by Doyle and Peercy [53].

ERDA using light to medium ions fills a gap in the capabilities of the widely available RBS technique and can be performed satisfactorily using the same 1-3 MeV accelerators [53]. However there are advantages to using very heavy ion beams and higher incident energies if a suitable accelerator facility is available. It should be noted that the use of heavy ion beams requires a higher beam energy to remain in the Rutherford scattering regime (see section 2.2.3 and Figure 2.3). The energy required is generally in the order of 0.5 – 1 MeV/amu.

2.3.1 Profiling of Heavy Elements

Profiling of heavy elements requires recoil energies high enough to enable emergence from the sample and detection of the particle. Energy transfer to recoils is higher for projectiles of similar mass to the target atom. To eject energetic heavy recoils using light ions, would necessitate such high incident energies that the collisions would no longer be Rutherford due to the penetration of the coulomb barrier and resulting nuclear reactions. The use of heavy incident ions enables profiling of heavier elements than is possible using light ions.

All recoils have similar velocities when very heavy ions are used. This follows from the kinematic factor for recoiling (Equation 2.2) which yields the following approximation when $M_1 >> M_2$:

$$\frac{E_2}{M_2} \approx \frac{4E_1}{M_1}\cos^2\phi \tag{2.17}$$

showing that velocity of all recoils is a function of the beam species and energy. This can be important for the detection of recoils of all species in a single measurement, particularly as it relates to the flight length of ToF telescopes.

2.3.2 Improved Depth Resolution

The glancing geometry used in ERDA increases the path length in the sample thereby increasing the energy difference associated with depth measured normal to the sample surface. The use of heavy ions, which have higher stopping powers than light ions, amplifies this effect. In this way, an energy resolution for any given detection system corresponds to a narrower depth resolution in the sample. For some types of detector, energy resolution improves for heavier ions and higher energies, lowering the limiting resolution and further improving the depth resolution obtainable.

Those using stopper foils to exclude scattered incident ions, can use thinner foils due to the shorter range of heavy ions. This reduces energy straggling in the foils for detected recoils, thereby improving energy and depth resolution.

It is worth commenting here that the extended path lengths in the sample also increase the effects of multiple scattering and the likelihood of plural scattering events. These effects can have a negative impact on depth resolution, and are discussed further, later in this chapter.

2.3.3 Improved Mass Resolution

Particle identification by mass differentiation of recoils is improved if heavier ions and higher incident energies are used. For mass differentiation, it is preferable that a small difference in mass between two recoil species should produce the largest possible energy difference in the recoiling

nuclei. The recoil energy difference, ΔE_2, between two recoils whose masses differ by ΔM_2 is given by

$$\Delta E_2 = E_0 \frac{d\Lambda}{dM_2} \Delta M_2 \tag{2.18}$$

Differentiating the kinematic factor for recoils, Λ (Equation 2.2), with respect to M_2

$$\frac{d\Lambda}{dM_2} = \frac{4M_1(M_1^2 - M_2^2)}{(M_1 + M_2)^4} \cos^2\phi \tag{2.19}$$

So Equation 2.18 becomes

$$\Delta E_2 = E_0 \frac{4M_1(M_1^2 - M_2^2)}{(M_1 + M_2)^4} \cos^2\phi \, \Delta M_2 \tag{2.20}$$

A large coefficient of ΔM_2 in Equation 2.20 gives better mass resolution. This can be achieved by using heavier ions (i.e. increasing M_1) and/or higher incident energy, E_0. Decreasing the recoil detection angle, ϕ, can also improve mass resolution although in practice other considerations will influence the choice of ϕ, which will often be fixed in a given laboratory system.

2.3.4 Increased Sensitivity

The recoil cross section, $\sigma_r(E_0,\phi)$, has a strong $[Z_1M_1]^2$ dependence on the atomic number and mass of the incident beam species (see Equation 2.4). This means that the sensitivity to impurities is greatly improved by the use of heavy ions. Even considering different beams with a constant energy per unit mass ratio, a Z_1^2 dependence remains. Under conditions where the incident ion is significantly heavier than the target atom, i.e. $M_1 >> M_2$, the recoil cross section may be approximated as

$$\sigma_r(E_0,\phi) \approx \left(\frac{Z_1M_1}{E_0}\right)^2 \left(\frac{Z_2}{M_2}\right)^2 \frac{e^2}{2\cos^3\phi} \tag{2.21}$$

Since the recoil dependency term Z_2/M_2 has an almost constant value in the order of 0.4-0.5 for all isotopes, the sensitivity is approximately the same for all recoil species. As the same ratio applies to the incident ions, the sensitivity scales like Z_1^4. For hydrogen, one of the most important

elements for impurity profiling, the ratio Z/M = 1, so the recoil sensitivity is approximately four times greater.

The low dependence of the recoil cross section on the target atom species prevents the recoil signal of light elements from being easily overwhelmed by that of heavier matrix components. This is one of the major advantages of HIERDA over RBS.

2.3.5 Reduced Sample Irradiation Damage

The increased sensitivity also allows for reduced analysis times as fewer incident ions are required to generate the same number of detected recoils. As well as reducing measurement time and cost, beam-induced damage of the sample can be lessened. It has been shown by several authors including Assmann et al. [11] and Davies et al. [13, 54], that for some types of samples, the beam damage can actually be minimised by using the heaviest available beam.

The quantity of interest is the damage induced per detected recoil. At the typical beam energies used in HIERDA, projectiles deposit energy primarily by electronic energy loss in the near-surface regions analysed. If different projectiles at similar velocities (i.e. constant energy per unit mass) are compared in the 1-2 MeV/amu range, the electronic energy loss scales almost linearly with Z_1 [11, 13]. Consequently, because of the Z_1^2 dependence of the recoil cross section, the beam-induced change per detected recoil can be smaller for heavier ions. However in some materials, a non-linear dependence of damage rate on electronic stopping power have been observed [11, 13, 54] and this simple relationship does not always hold.

Beam induced changes in the sample can monitored in some cases using ‘event-by-event’ data acquisition. In some HIERDA facilities such as the ANSTO system used in this work, recoil detection events are recorded in a log file as they occur. The output spectra are reconstructed from this event file. This allows subsets of the output to be separated and compared. Changes in the

stoichiometry of the sample during the measurement, due to beam induced 'mixing' or gaseous effusion of volatile components such as H_2, N_2, and O_2 can be detected. Timmers et al. [51] and Bohne et al. [46, 55] have shown that the change in stoichiometry can be plotted as a function of projectile fluence and a correction applied so that a 'zero dose composition' can be determined .

2.3.6 Critical Angle for Scattering

The critical angle for scattering of heavy ions from lighter nuclei (see Equation 2.3) can be exploited to prevent scattered incident ions from reaching the detector. While mass dispersive detectors such as ToF-E telescopes usually allow the separation of the scattered ion signal from the recoil signals, radiation damage of the energy detector can be reduced by excluding the relatively high fluence of the scattered beam particles.

2.4 Limitations in Heavy Ion ERDA

The advantages described in the previous section are consequences of the kinematic energy transfer characteristics, higher energy loss rate, and enhanced scattering cross sections of heavy ions. These differences also lead to some disadvantages. The appropriate choice of analysis method including incident beam and energy, will generally be a compromise between the benefits discussed above and the restrictions outlined here.

2.4.1 Reduced Analysis Depth

The higher energy loss rate and interaction cross section for heavy ions, reduces the range and hence the probing depth for heavy ion beam techniques. The reduced ion range may be compensated for by using a higher incident energy. This, however, requires the availability of a larger accelerator with a higher accelerating voltage, and/or the selection of higher charge-state ions in the accelerator analyser. The latter is limited by the charge-states which are available for various beam ions and the lower yield of highly charged ions within the charge-state distribution.

2.4.2 Sample Damage

While HIERDA is not intentionally destructive, the energy deposited by swift heavy ions in the processes of electronic and nuclear stopping result in damage of the sample under analysis. Higher stopping powers associated with heavy ions result in higher linear energy transfer (LET) coefficients which characterise the damage density per unit path length. The damage per incident ion will be greater for heavier ions, although as described above, the total sample damage per measurement can be optimised by considering the increased probability of recoil production.

For samples containing volatile components such as H, N and O, the higher damage density increases the molecular recombination rate and subsequent desorption of H_2, N_2 and O_2 molecules. A study by Walker et al. [56], of radiation damage in various materials during HIERDA analysis, showed that such desorption is strongly sample dependent, and also depends approximately on the square of the electronic stopping power of the projectile and so varies with Z_1^2. Shrestha and Timmers [57] observed rapid nitrogen depletion during analysis of indium nitride films with ^{197}Au and ^{109}Ag projectiles but not when using ^{32}S and ^{19}F beams. They have concluded that there may exist a threshold atomic number and energy loss rate below which gaseous effusion does not occur.

2.4.3 Increased Multiple Scattering

Enhanced cross sections and extended path lengths increase the probability of more than one significant scattering event occurring along the paths of the incident ion and recoil atom through the sample. The analysis of ERDA data assumes that a single scattering event generates the recoil and that the detection angle and energy transfer are well characterised by the kinematic equations of section 2.2.2. The occurrence of secondary scattering events changes the angles involved in the primary scattering event, and alters the incident or recoil energy before or after the event.

These differences between the ideal situation and the reality of the experiment complicate the interpretation of data. The degree to which predicted spectra based upon the single-scatter approximation agree with experimental output, decreases for heavier incident ions as the scattering cross section increases and the influence of multiple scattering events grows correspondingly larger. This discrepancy is the motivation behind this work and described in detail in the following sections. The simulation process, by which IBA data are usually interpreted, is described including the difficulties presented by multiple scattering.

2.5 Data Interpretation By Simulation

The interpretation of output data from IBA experiments is usually done by *spectrum simulation*. In this process, the shapes of energy spectra that will be produced using a particular experimental configuration, and for a given sample description, are theoretically predicted and compared to the measured output. An iterative procedure of refinement of the sample description, followed by further quantitative comparison, ultimately leads to a 'sufficiently good' fit. The proposed sample description is then assumed to match that of the experimental sample.

The prediction of the energy spectra is done by a method known as *slab analysis*. The sample is described as a series of thin layers, or 'slabs', whose thickness is chosen sufficiently thin that energy loss and cross section changes within any slab can be ignored. The contribution to output spectra of each layer is determined separately and adjusted by considering the effects of the overlying layers on the energy and yield of ions and recoils passing through each of the layers. For each recoil species in each layer, the energy of detectable recoils is determined as a function of depth of origin by calculating the energy loss in each layer along the paths. A relationship between energy and depth is identified so that the energy spectra can be interpreted as depth concentration profiles. Slab analysis is depicted in Figure 2.7 which is adapted from [10] where the complete details of the calculations can also be found.

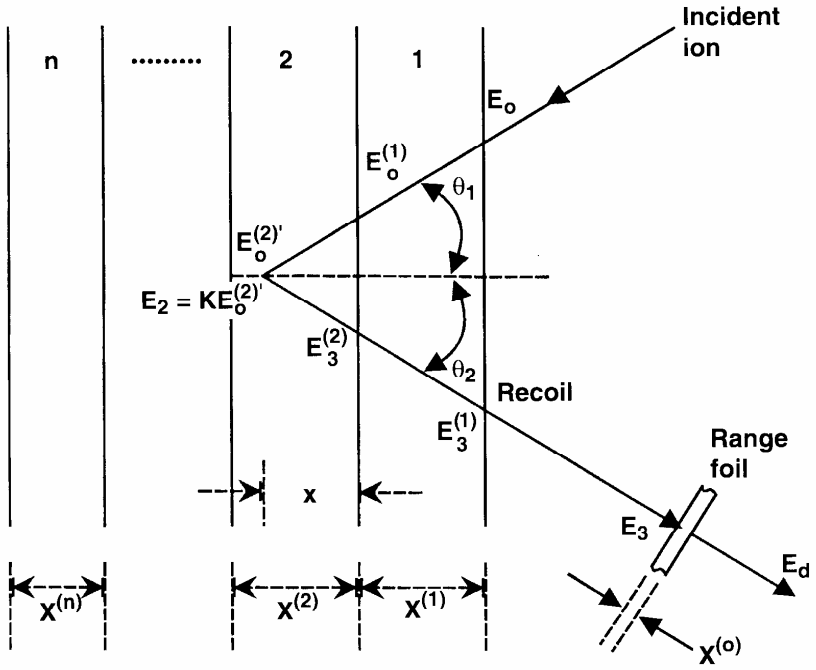

Figure 2.7 Slab analysis of a sample described as a series of n layers.

(Figure adapted from [10] in [6])

There are a number of widely used software packages, all of which implement the slab analysis method of data interpretation for various IBA techniques. Well known examples include RUMP [58], DEPTH [59, 60], SIMNRA [61], RBX [62], and IBA Data Furnace [63]. In a comprehensive review of ion beam data analysis and simulation software in 2006, Rauhala et al. [64] presented a detailed review of 12 widely used programs and described a vast array of other codes whose use is generally limited to a single institution. Almost all programs described were based on slab analysis and theoretical simulation comparison, with only a few direct spectrum analysis methods existing, the latter usually designed to solve very specific problems.

The profiles predicted by considering the scattering kinematics and energy loss processes must be corrected for physical and experimental factors that degrade the signal in the experimental spectra. If processes causing peak broadening in the measured energy profiles that are associated with depth are not accounted for, matching measured spectra will be difficult and may lead to errors in the sample description. Examples of such factors include: the distribution widths of incident beam

energy and direction, beam spot size, detector solid angle, electronic energy loss straggling, energy detector resolution and the influence of an absorber foil if present, including thickness inhomogeneity. These influences are usually modelled as Gaussian functions which are then convoluted with the profiles generated from descriptions of the layer thicknesses and stoichiometry. The resulting spectra should feature the resolution observed in the experimental spectra, however, unless the simulation also accounts for multiple scattering, there is likely to be a discrepancy.

Simulations are usually based on a single-scatter model. The ingoing and outgoing paths are assumed to be straight lines with a single scattering event occurring where these paths intersect. In reality, ions undergo many small interactions along their paths through the sample, and these paths are not necessarily straight lines. This multiple scattering manifests itself as a further energy broadening in the elemental spectra. A few simulation programs include an approximation of this effect, and are discussed in section 2.7.

The lack of accurate representation of multiple scattering is one of the most significant limitations in the analysis of HIERDA spectra. The oblique angles, long path lengths, and high cross sections mean that multiple scattering cannot be ignored, and that an overly simplified treatment is unlikely to be successful in the general case. The handling of multiple scattering in the spectrum simulation process will be discussed following a detailed description of the influences involved in multiple scattering.

2.6 Multiple and Plural Scattering

Multiple scattering of energetic ions by sample nuclei is generally divided into two categories: (i) small angle multiple scattering and (ii) large angle plural scattering. The distinction between the two regimes is somewhat arbitrary, and is usually based upon qualitative assessment of effects observed in the output data, or the mathematical treatments required to deal with them. A practical

differentiation might be based on the degree to which a continuous analytical treatment of multiple scattering adequately represents measured data.

Small angle multiple scattering refers to the process of many small interactions which together contribute to a gradual divergence of a parallel beam of ions, both in direction and lateral displacement, combined with energy straggling due to the individual path differences. Small angle multiple scattering is depicted in Figure 2.8.

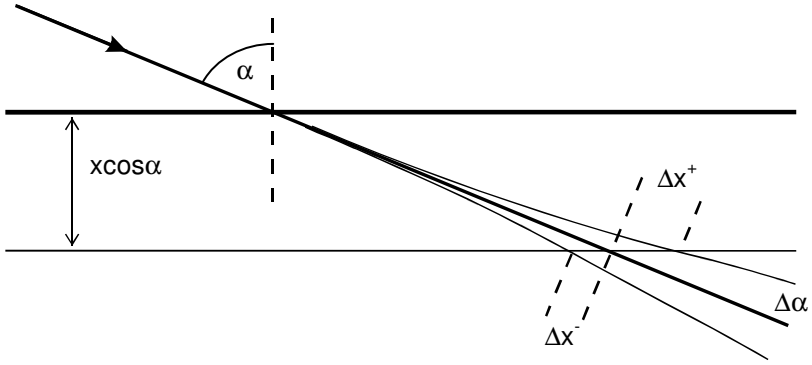

Figure 2.8 Small Angle Multiple Scattering of an incident beam passing through a sample layer. The beam divergence, $\Delta\alpha$, is shown, together with the corresponding increase, $\Delta x+$, or decrease, $\Delta x-$, in the path length, x, for ions reaching a depth $x\cos\alpha$.

Large angle plural scattering refers to the cases where an ion or recoil atom experiences a small number of discrete events with significant energy transfers and direction changes. Several variants are possible depending upon whether it is the incident ion, the recoil atom, or both, which have a secondary scattering event. These are depicted in Figure 2.9. A recoiled target atom may reach the detector after being initially directed away from the detector but subsequently scattered into the detector solid angle (Figure 2.9a). The recoil may be directed into the detector by an ion which has previously been scattered from the initial beam direction (Figure 2.9b). Both of the above may occur (Figure 2.9c). An incident ion may be detected after being plurally scattered in the sample (Figure 2.9d).

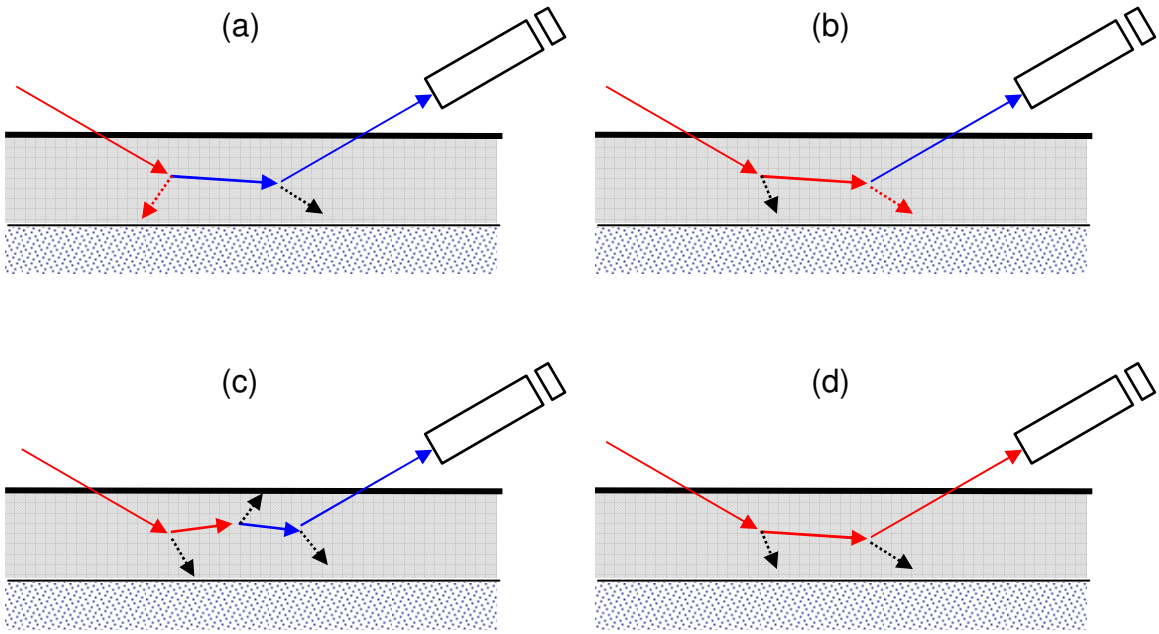

Figure 2.9 Large angle plural scattering of (a) the detected recoil, (b) the projectile prior to generating the detected recoil, (c) both of these events, and (d) a detected scattered projectile.

In each case, the major influence of multiple scattering is that the energy of a detected recoil or scattered incident ion is not necessarily simply related to its depth of origin within the sample. As discussed in section 2.5, the relationship between the energy of a detected particle and its depth of origin in the sample is a fundamental part of the data interpretation process.

Multiple scattering in ion beam analysis has been the topic of a significant amount of investigation, as it imposes a fundamental limit on the depth resolution obtainable with a given experimental technique. Most work has focussed upon small angle multiple scattering because it is the most amenable to analytical mathematical methods. As the process consists of a large number of small interactions, the effects on the distribution of particles in the beam can be considered statistically, and the net effect on the output of the experiment can be treated as a continuous function operating on the elemental energy spectra of the detected recoils. Large angle plural scattering, however, involves a relatively small number of discrete events whose individual influences will vary in magnitude and are more complicated to account for as each interaction must be considered.

2.6.1 Small Angle Multiple Scattering

Small angle multiple scattering, as depicted in Figure 2.8, involves two effects: energy straggling due to the statistical variation in the amount of energy imparted during the many small nuclear elastic scatters; and beam broadening – both angular and lateral spreading of the beam of ions. These latter beam broadening components also manifest themselves as energy broadening effects in the experimental output. This occurs by two mechanisms: path length differences and kinematic angle change.

Consider a beam of ions incident upon a sample at an angle, α, as depicted in Figure 2.8. An un-deflected ion reaching a depth $x\cos\alpha$ in the sample will have traversed a path length, x. Ions reaching the same depth after having been deflected slightly by multiple scattering, will have an increased or decreased path length, depicted by $\Delta x+$ and $\Delta x-$ respectively. In addition to the normal energy straggling associated with electronic stopping, these ions will have components due to the differences in macroscopic path lengths, and nuclear scattering. A positive feedback mechanism exists – the more an ion is deviated from its initial direction, the more energy it has imparted in nuclear scattering and the longer its path length. The reduced ion energy increases the cross section for further scattering.

The angular spread associated with this lateral spreading of the beam, means that the scattering angle required in the primary scattering event for an ion or recoil to reach the detector is altered. The result is a broadening of the energy of detected particles according to the dependence of kinematic factors on scattering angles (see Equations 2.1 and 2.2).

The energy differences resulting from these two effects act in opposite directions. Ions scattered away from the sample normal will have an increase in path length to reach the same depth, so the

additional electronic stopping decreases its energy. Such an ion will now require a smaller scattering angle to cause a detected ion or recoil which will therefore have a higher kinetic energy.

The grazing angles of HIERDA geometry lead to asymmetry of the energy spread of particles deflected toward or away from the sample normal. The path length asymmetry is shown in Figure 2.8 in the magnitudes of $\Delta x+$ and $\Delta x-$. A yield asymmetry also arises from the depth difference associated with scattering toward or away from the normal. Fewer particles recoiled from deeper in the sample will reach the surface and be detected.

Comprehensive theoretical studies of small angle multiple scattering have been published by several authors including Sigmund and Winterbon [65], Marwick and Sigmund [66], and Amsel, Battistig and L'Hoir [67]. Sigmund and Winterbon have tabulated angular distributions, and Marwick and Sigmund the corresponding lateral spread distributions. The numerical calculations were based on a small angle limit approximation and are valid in the screened Coulomb regime corresponding to the large impact parameters which yield small angular deflections. Amsel et al. built on the work of Sigmund and co-workers incorporating stochastic theory and extensive numerical calculations to make the theory more robust by properly considering the statistical dependence between the angular and lateral spreads. Szilagyi et al. have incorporated these results into their computer program DEPTH [60] to improve the accuracy of simulation of IBA spectra.

The small angle approximation used in the theoretical approach neglects the momentum transfer to target atoms. That is, the effect of small angle multiple scattering is incorporated only as direction changes and lateral deviations and not energy losses due to momentum transfer to recoil atoms. Thus the treatment is particularly limited in its application to the scattering of ions heavier than the sample components beyond very small angles. An attempt by Winterbon [68] to analytically calculate the angular distribution of very heavy ^{209}Bi ions in a thin C layer involved numerical series with hundreds of terms and was described as being no simpler than a full Monte Carlo solution. The validity of these analytical approaches fails when the directional deviations and

energy transfers are large and infrequent enough that they can no longer be treated as continuous energy loss processes. This is the case for large angle scattering events which have a low probability, and rarely occur more than a few times for the same ion.

2.6.2 Large Angle Plural Scattering

Ions and recoils detected following large angle plural scattering will be recorded with an energy which is not simply related to their depth of origin in the sample. As was discussed in the previous section, the relationship between the energy of a detected particle and its depth of origin in the sample is a fundamental part of the data interpretation process. Plurally scattered particles generally have reduced energy due to the energy imparted during secondary scattering events, and will appear to have originated deeper in the sample.

It is also possible for plurally scattered recoils to be detected with higher than expected energy. This occurs when the product of kinematic factors for the smaller scatters exceeds the factor for single scattering at the detection angle. Consider the case of a single scatter at 45˚ versus two scatters of 22.5˚ each. Comparing the recoil kinematic factor, Λ, for a recoil angle of $\phi = 45^\circ$, with the square of the factor for $\phi = 22.5^\circ$, gives

$$\frac{(\Lambda_{22.5^\circ})^2}{\Lambda_{45^\circ}} = \frac{4\beta}{(1+\beta)^2}\frac{\cos^4 22.5}{\cos^2 45} \tag{2.22}$$

where $\beta = M_2/M_1$ is the mass ratio of the two particles (note: the recoil kinematic factor is symmetrical in M_1 and M_2). Solving for β shows this ratio exceeds 1 for values of $\beta < 3.55$ as shown in Figure 2.10. The triple-scatter factor is also shown to exceed 1 for $\beta < 2.72$. The situation is slightly more complicated for scattered ions due to the double valued kinematic factor for scattering and the critical angle limit when $M_1 > M_2$. For the positive roots of equation 2.1, and for $M_2 > M_1$, the kinematic products for 2 and 3 equal scatters totalling 45˚ are always greater than 1.

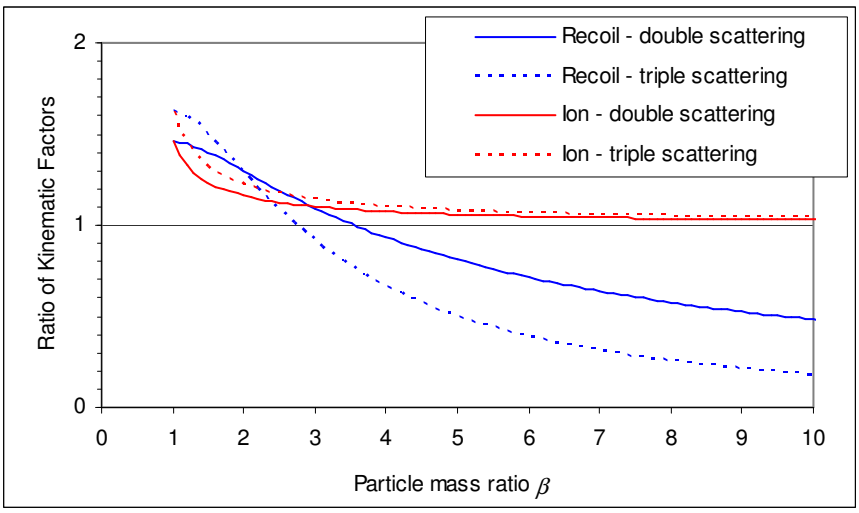

Figure 2.10 Ratio of the product of kinematic factors for double and triple scattering compared to single scatter factor. See text for details.

The above considerations mean that plural scattering can result in counts at almost any energy in the range of the recoil spectrum, including above the high energy surface edge. Experimentally, plural scattering is responsible for long, low energy tailing and conspicuous high energy edge artefacts in measured spectra. These are discussed in further detail in Chapters 4 and 5.

The spectral distortions introduced by plural scattering are complex, and analytical treatments based upon small angle multiple scattering approximations fail to predict these features of the experimental spectra [64, 69, 70].

A few studies [61, 71-74] have attempted to partially address plural scattering by developing an analytical treatment of *double* scattering which is expected to be responsible for a large fraction of plural scattering. Most of these studies have been in the context of RBS which is a much simpler case: only the He or H projectile needs to be accounted for; normal incidence provides for useful symmetry properties; and backscattering geometry only requires consideration of paths with two quite large scatters. Only Repplinger et al. [74] have tried to model double scattering in He-ERDA, requiring the consideration of multiple recoil species, but their results were described by Rauhala

[64] as unsatisfactory, being too low in magnitude by a factor of 10, clearly indicating that not all contributions were being correctly accounted for.

Barradas et al. modelled double scattering in grazing angle RBS, and showed that the asymmetry associated with shallow angles, as are also used in HIERDA, greatly complicates the calculation [73]. Mayer's simplified double scattering model increases the computing time required by a factor of about 200 [75]. Barradas' showed that including a more detailed double scattering calculation when grazing angles are involved, increased the number of trajectories to be calculated by a factor of approximately 6000 for a typical sample containing 5 elements. To include the double scattering trajectories and deflections for all recoils in a HIERDA model would further increase the number of calculations by a factor of $(N_E+1)^5$ or $6^5=7776$ for a sample of $N_E=5$ elements (The index 5, represents 3 path segments separated by 2 scattering points in a double scatter trajectory). Thus the total calculation burden would be in the order of $5x10^7$ times larger than a single scatter model.

The complexity of these calculations, just to achieve a double scatter model let alone higher order plural scattering, has lead several authors to the conclusion that quantitative treatment of plural scattering can only be satisfactorily achieved using Monte Carlo techniques, e.g. [7, 64, 72]. In their theoretical treatise on multiple scattering [67], Amsel et al. used Monte Carlo simulation as the 'gold standard' with which to validate the theoretical models for small angle scattering. In Monte Carlo simulation, individual scattering interactions are modelled for each ion, so both multiple and plural scattering are implicitly included together and not treated separately. The Monte Carlo technique for simulating ion transport problems is described in detail in Chapter 4.

Several studies have been published describing Monte Carlo approaches to dealing with multiple scattering and plural scattering: RBS studies include those by Steinbauer, Biersack and Bauer [76-78], Eckstein and Mayer [72], and Pusa et al. [79]. Li and O'Connor studied backgrounds in low energy heavy ion backscattering spectrometry (HIBS) [80], and Tassotto and Watson studied very low energy (2-4 keV) recoil spectrometry of diamond surfaces [81].

MC simulation has been used to study HIERDA by Johnston and co-workers [48, 82], Arstila, Sajavaara, Edelmann and co-workers [8, 9, 83, 84], Mayer et al. [85], Knapp et al. [86], and in publications arising from this work [87-91].

2.7 Multiple & Plural Scattering in Simulation Software

Many ion beam data analysis programs do not include any handling of multiple scattering. In their recent review of analysis software [64] Rauhala et al. listed the features of twelve widely used IBA software packages. Only four of these include a small angle multiple scattering component, and just two (SIMNRA and WiNDF) include a double scattering approximation. None address higher order plural scattering. A summary of these columns of the list is given in Table 2.2.

Table 2.2 Summary of Multiple and Plural Scattering handling of twelve IBA data analysis programs (source: Rauhala et al. [64])

Program	IBA Techniques	Multiple Scattering	Plural Scattering
Beam Expert	RBS, HIBS, NRA	None	None
BS1	RBS, NRA	None	None
DEPTH	RBS, ERDA, NRA	Yes	None
DVBS	RBS	None	None
GISA	RBS	None	None
IBA	RBS, ERDA, NRA	None	None
Particle Solid Tools	RBS	None	None
PERM	RBS	None	None
RBX	RBS, ERDA, NRA	Yes (DEPTH model)	None
RUMP	RBS, ERDA	None	None
SIMNRA	RBS, ERDA, NRA	Yes (Gaussian approx. of DEPTH model)	Double Scattering approximation optional
WiNDF (DataFurnace)	RBS, ERDA, NRA, NDP, PIXE	Yes (Gaussian approx. of DEPTH model)	Double Scattering approximation optional

Of those that include small angle multiple scattering, only DEPTH and RBX use the full theoretical treatment of Szilagyi [60] mentioned in section 2.6.1 and discussed below. The other two, SIMNRA and WiNDF use a Gaussian approximation of the energy broadening with the width obtained using the DEPTH code, to simplify the calculation. Most energy broadening effects are modelled as Gaussian functions as these can be easily combined to predict the experimental resolution. However, as shown by Szilagyi, the energy spread due to multiple scattering is not Gaussian.

In the DEPTH code treatment of multiple scattering, the angular deviation and lateral displacement of each particle are highly correlated and this dependence must be explicitly corrected for. Scattering along inward and outward paths are independent, so the analytical representations of these two components are to be convolved with the other, usually Gaussian, components . The convolution process is complicated for non-Gaussian functions. For this reason, Gaussian shaped approximations are attractive as the convolution of these returns another Gaussian whose width is simply calculated via quadratic summation. Szilagyi has employed an alternative curve fitting method that allows a convolution-like composition to be done more readily. While describing their method as 'not rigorous', the results are more precise than those obtained using Gaussian approximations.

Szilagyi, Wielunski and co-workers have demonstrated the DEPTH code against H profiles in thin layered Al, Cu, Ag, and Au samples [69], and in thicker Al, Cr, Zr, and W samples [70] measured by He-ERDA. The calculated curves fitted the measured data quite well - much more closely than did RBX which has no multiple scattering treatment, providing strong evidence of the need to include multiple scattering effects. It was shown that not accounting for multiple scattering effects will result in incorrect sample interpretation. It was concluded that multiple scattering is the dominant component responsible for limiting both depth resolution and H detection sensitivity.

In both papers, only recoiled H profiles were calculated – no heavier element profiles were shown. Although the fits were far better than for RBX predictions, discrepancies in both the tailing and the peak yield could still be observed. These effects were more pronounced for the heavier samples, and were attributed to plural scattering which was not taken into account. Due to the higher cross sections, the discrepancies are expected to be greater for heavy ions and high Z recoil elements.

Of the many simulation codes, the few sophisticated programs such as DEPTH, SIMNRA, and WiNDF (which is actually a fitting algorithm with DEPTH and SIMNRA type simulations embedded) are gaining popularity, and regularly feature in published material studies. However, they rarely appear in studies using heavy ion techniques, and do not appear to have been properly tested or at least convincingly demonstrated to be accurate for HIERDA of heavy recoil species where multiple and plural scattering effects are most pronounced. Elliman et al. [33] determined that, in HIERDA using Au ions, DEPTH calculations underestimated the measured depth resolution of Al and Co recoils, except at the surface. Weijers et al. [92] showed DataFurnace simulations fit well to light element (O, N) spectra obtained by HIERDA with 200 MeV Au ions, but discrepancies existed for Si spectra. Similar discrepancies occurred for SIMNRA fitting to Si and O profiles from HIERDA measurements using 10 MeV Au in work by Climent Font et al. [40].

Alternative methods exist with the potential to enable inclusion of all effects. A novel artificial neural network approach introduced by Vieira and Barradas [93] uses a 'learning algorithm' which can eventually interpret experimental spectra, after being 'trained' on a sample set of 'known' spectra and solutions. The program requires no built-in physics. The principle drawback is the requirement for 1000's (or 10's of 1000's !) of sample spectra of each specific system to be studied (e.g. Ge implants into Si, to doses between 10^{14} and 10^{18} Ge atoms/cm^2 and depths between 1 and 1500 nm). While the training burden is clearly a significant impediment, some success has been demonstrated for a few more complex systems, using training spectra generated artificially with simulation codes. Of course, if the simulated spectra have not comprehensively accounted for plural scattering effects, then the training process has an inherent weakness, and errors are likely to

be made when analysing real samples which *do* have these effects. So far, the method has only been applied in systems where the plural scattering contributions, and any deficiencies in the DEPTH treatment of multiple scattering, have been declared negligible.

The most promising method for dealing appropriately with multiple and plural scattering is Monte Carlo simulation. The modelling of individual interactions inherently allows for proper inclusion of all scattering effects. There is currently no general release MC software available for analysis of ion beam data. All studies so far that have applied MC techniques to IBA problems, have employed codes developed by the authors, usually based upon existing fundamental ion transport algorithms originally created for other purposes.

2.8 Summary

HIERDA is a powerful analysis tool and is recognised as a valuable complement to other materials characterisation methods. Multiple and plural scattering strongly effect HIERDA experiments, in some cases being the limiting factor in obtainable depth resolution and sensitivity. A rigorous analytical treatment of small angle multiple scattering goes a long way towards reducing the errors associated with the influence of multiple scattering on measured elemental energy profiles. This approach, however, fails to correctly account for the high and low energy spectral features associated with large angle plural scattering. These features are often very pronounced in IBA techniques using heavy ions. Current slab analysis programs cannot reproduce these features accurately, and not accounting for multiple and plural scattering has been shown to lead to incorrect sample analysis in many cases.

Monte Carlo simulation is a natural choice for studying these effects. A detailed understanding of all scattering contributions may contribute to the development of an analytical approach to their inclusion. Alternatively, improvements in the efficiency of MC simulation of HIERDA spectra may ultimately allow routine use of this approach for data analysis.

Chapter 3

Experimental Method for Acquisition of Reference Spectra

The Monte Carlo simulation developed as part of this study (described in detail in the next chapter), requires validation against experimental data. Reference spectra were acquired from measurements conducted on well characterised samples for direct comparison to simulated spectra. The samples were specifically chosen to test the ability of the code to accurately predict the complex features associated with plural scattering, and to demonstrate pathological cases where data interpretation is difficult and MC simulation offers some insight into the contributing factors.

The experimental configuration to be simulated is described here along with descriptions of the samples and the method of data processing, including the extraction of Time spectra for comparison to simulated data.

3.1 Experimental Configuration

3.1.1 Accelerator

The HIERDA measurements were performed using the ANTARES (*Australian National Tandem Accelerator for Applied RESearch*) accelerator facility of the Australian Nuclear Science and Technology Organisation (ANSTO), located at Lucas Heights, Australia.

ANTARES is a 10 MV Tandem accelerator with several beam-lines and target stations including the Ion Beam Analysis chamber fitted with a Time-of-Flight spectrometer for HIERDA. A multi-sample caesium sputter ion source allows a choice of ion species. ^{127}I and ^{81}Br beams at energies between 40 and 97.5 MeV were used in this work.

3.1.2 Time-of-Flight Spectrometer

The Time-of-Flight and Energy (ToF-E) telescope is positioned at an angle of 45˚ to the incident beam direction as shown in Figure 3.1. Samples are typically mounted symmetrically with incident and exit angles of 67.5˚ to the surface normal, although this can be adjusted by tilting the sample relative to the beam direction to improve recoil yield in some measurements.

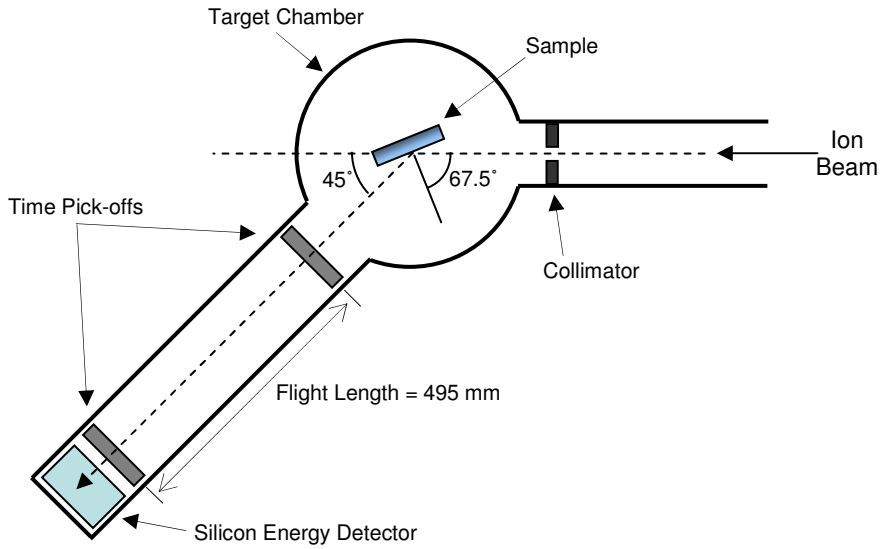

Figure 3.1 Schematic of experimental target chamber and Time-of-Flight telescope.

(Figure adapted from [94] as cited in [10])

The ToF-E telescope of the ANSTO installation follows the design of Whitlow and has been described in detail in [95]. The telescope consists of two time pick-off detectors separated by a flight length of 495 mm, and a silicon surface barrier energy detector. The time pick-off detectors are based on the design by Busch et al. [96] and are shown in Figure 3.2. Each time detector

consists of a 25.3 μg/cm^2 carbon foil perpendicular to the path of the recoil ions entering the detector. Secondary electrons ejected from the foils when the recoil nuclei pass through, are directed towards the micro-channel plate electron multipliers by an electrostatic potential 'mirror' and the resulting timing signal is recorded. The design is such that the electron trajectories are isochronous relative to the position on the foil struck by the recoil ion, to minimise the electron path length contribution to time resolution.

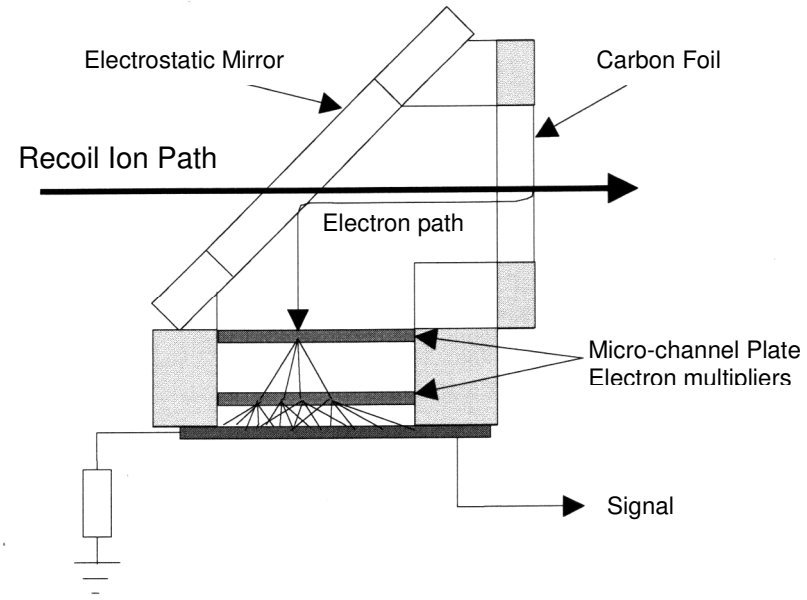

Figure 3.2 Schematic diagram of time pick-off detector (picture adapted from [95])

A Time to Amplitude Converter produces a pulse with a voltage amplitude related to the time interval between the two timing signals. A greater number of signals is generated by the first timing foil than the second due to the former's larger solid angle. To reduce the number of random coincidence events recorded by START signals without corresponding STOP signals, the pulse from the second timing foil is used as the START signal, and the pulse from the first timing foil is delayed and used as the STOP signal. The flight time ΔT is given by $\Delta T = T_0 - T$ where T is the time measured between the timing signals by a Time to Amplitude Converter (TAC), and T_0 is the delay time added to the signal from the first time detector.

A silicon surface barrier (SiSB) detector is used as the energy detector of the ToF-E telescope. The SiSB detector has an active area of 100 mm^2 and is positioned approximately 15 mm after the second timing foil, such that the effective solid angle for the ToF-E telescope is determined by the solid angle of the second timing foil and not further reduced by the energy detector.

The two outputs of the ToF-E detector are processed in coincidence mode so that only events generating both Time and Energy signals are recorded. The energy-proportional pulse and the TAC output are converted from analogue voltage amplitudes to digital channels and stored event-by-event in a log file during run-time. The event file data can be displayed as two-dimensional histograms viewed during measurements, or post-processed off-line.

3.2 Experimental Output and Data Processing

3.2.1 Two Dimensional Time-of-Flight and Energy Histograms

Plotting of two-dimensional ToF-E histograms and the extraction of one-dimensional Time spectra in this work is done using the RDA (Recoil Data Analysis) software developed at RMIT by Stannard [5]. Figure 3.3 shows an example of the 2-D ToF-E histogram from a measurement of a multi-layered chromium sample consisting of three 135 nm Cr layers on a Si substrate, where the intermediate layer is a metalised hydrocarbon layer containing 18 % Cr, 64 % C and 18 % H.

Each isotopic mass is represented as a curve in the Time-Energy plane, with the colour map representing counts. The elements present in this sample are labelled. The upper right end of each curve represents the detection of the highest energy particles of each mass, from either the sample surface or the uppermost interface of a sub-surface layer. The Cr signal shows the 3 layers, the surface and buried layers having higher intensity than the intermediate layer which has a lower Cr content. The surface can be seen to have some C and O contamination. The C signal of the intermediate layer is clear, and this layer also has some N and O contamination. The H signal is not visible in this plot as the gain settings have been chosen optimally for heavier recoil species. The Si

substrate can be seen below the sample layers. Some tailing is visible at the layer interfaces for each element – this is the multiple scattering contribution i.e. particles detected whose energy is not simply related to the scattering kinematics and the electronic energy loss associated with their depth of origin.

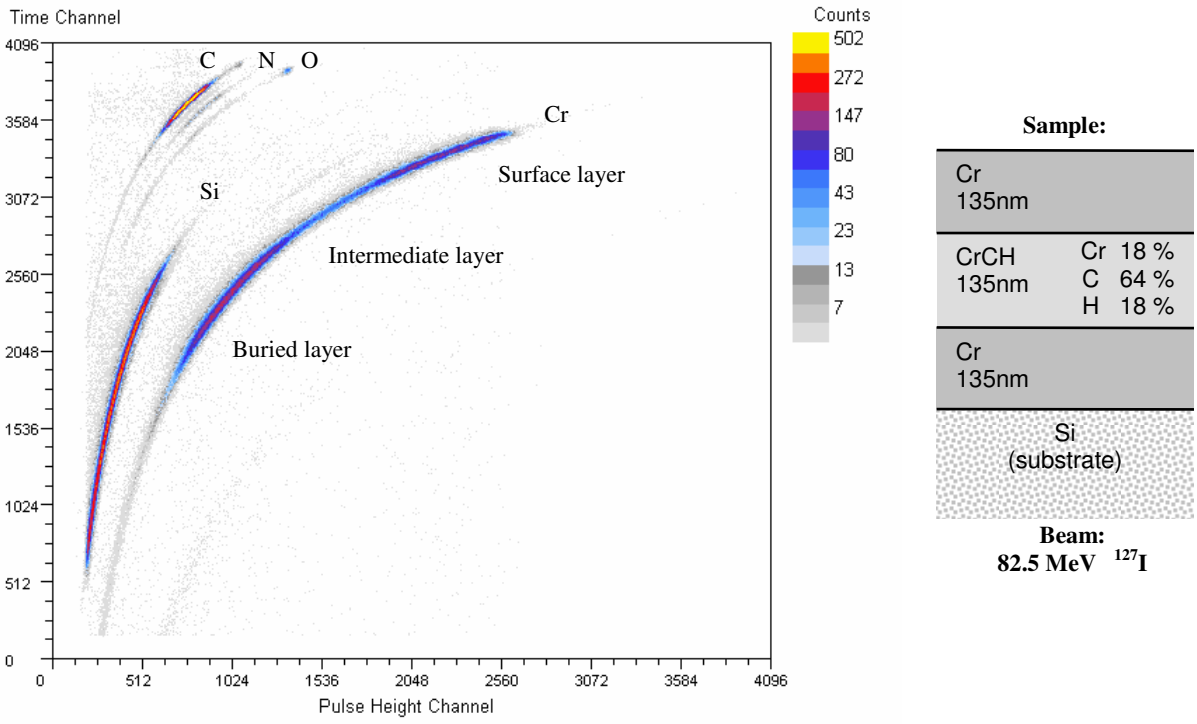

Figure 3.3 Two-dimensional histogram from a HIERDA measurement of a Cr multi-layer sample with dimensions and composition as depicted (right).

The data from a single isotope may be selected geometrically using the graphical user interface of the RDA software, and the subset of events can be projected to the Time or Energy axis, and extracted to a separate file for display as a Time spectrum. Figure 3.4 shows the geometrical selection of the Cr signal (a), 'cut' of points outside the selection (b), and projection of the selected subset to the Time axis (c). The Cr Time spectrum clearly shows the 3 layers but it is interesting to observe that at all three layer interfaces, the distinction between the layers is obscured by the pronounced tailing due to multiple and plural scattering. The precise location of the interfaces is unclear, and the traditional 'trapezoidal' shapes normally associated with discrete layers in backscattering and recoil spectra are almost unrecognisable.

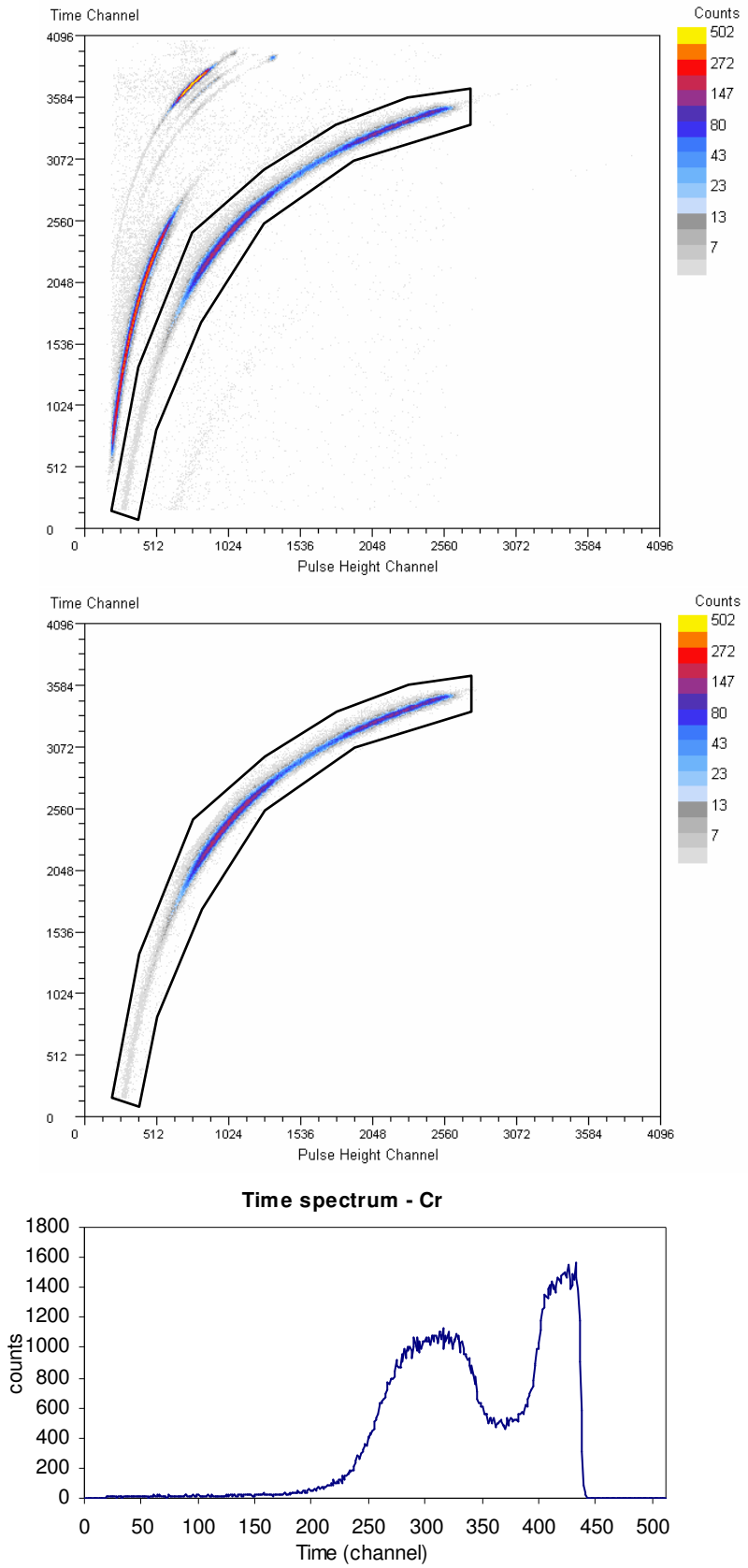

Figure 3.4 Geometrical selection (a), subset extraction (b), and projection to Time axis (c) of Cr signal from 2-D Time-Energy histogram.

3.2.2 Calibration

Time calibration is achieved by collecting spectra for a set of known samples and extracting Time spectra. For each known element, the time channel corresponding to the half height of the surface edge of the measured peak (see Figure 3.5) is associated with the energy of atoms recoiled from the surface. The surface recoil energy is calculated using Equation 2.2 for the recoil kinematic factor, and converted to time using Equation 2.16. The calculated recoil energy is corrected for energy loss in the first timing foil using stopping powers calculated with SRIM. An example of a calibration data set is given in Table 3.1. This calibration is for the 97.575 MeV Iodine beam as specified in Table 3.2 along with the detector parameters required for the calculations. The determination of the surface edge channel is shown in Figure 3.5 for recoiled Zr. The resulting Time calibration function is also shown in Figure 3.5, showing that the response of the Time-of-Flight telescope is highly linear.

Table 3.1 Time of Flight calibration data for HIERDA measurements using 97.575 MeV Iodine beam and detector parameters as specified in Table 3.2.

Recoil Species	**Mass** (amu)	**Z**	**Recoil Kinematic Factor**	**Recoil Energy** (MeV)	**Stopping Power in C foil, Se(E)** (keV/ug/cm2)	**E Loss in C foil** (keV)	**Energy in ToF** (MeV)	**Time of Flight** (ns)	**Surface Edge** (measured channel)
C	12.011	6	0.1580	15.415	5.4742	109	15.305	31.56	486
O	15.999	8	0.1989	19.403	8.2956	166	19.237	32.49	481
Si	28.086	14	0.2968	28.956	18.764	375	28.580	35.32	465
Co	58.933	27	0.4331	42.261	40.349	807	41.454	42.48	424
Zr	91.220	40	0.4866	47.482	48.291	966	46.516	49.90	380
Ta	180.950	73	0.4846	47.284	50.106	1002	46.281	70.45	269
Au	196.970	79	0.4766	46.504	49.65	993	45.511	74.12	249
Beam:			**Scatter factor**	**Scatter energy**					
I	126.900	53							
Scattered from:									
Ta	180.950	73	0.6430	62.745	55.003	1100	61.645	51.12	377

Table 3.2 Incident beam energy calculation and detector parameters for input to Time of Flight calibration of Table 3.1

Beam Parameters			Detector Parameters		
Beam species:	**^{127}I**	(Iodine)	Recoil detection angle:	**45**	degrees
Mass	**126.9**	u	Flight length:	**0.495**	m
Injection voltage	**0.075**	MV	Timing foil thickness:	**25.3**	μg/cm^2
Tank Voltage	**7.500**	MV			
Energy at Stripper	**7.575**	MV			
Charge State 'Q'	**12+**				
Energy of beam	**97.575**	MeV			

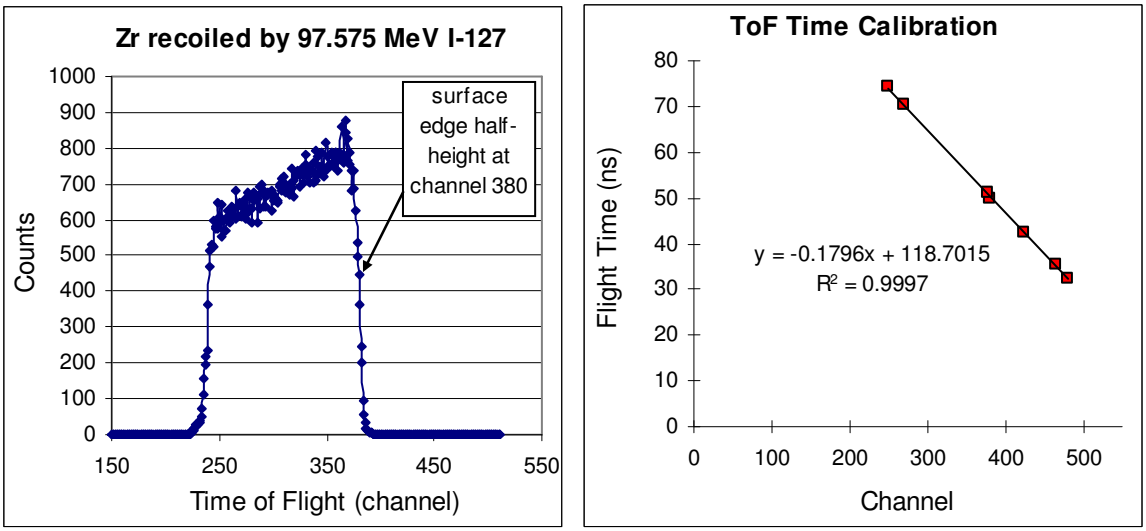

Figure 3.5 Calibration Time spectra for Zr recoiled by 97.575 MeV ^{127}I with surface edge channel indicated by the arrow (left); and Time of Flight calibration curve for data in Table 3.1 with linear regression fit (right).

Different Energy signal amplifier gain and Time signal delay settings were adopted for each set of measurements on different samples or with different beam species and energies. This was to ensure the appropriate ranges of Flight times and residual energies were included for the recoil species being measured. Scattered ion signals were also always included as these are used for normalising the simulated and measured spectra. A new calibration was performed for each new combination of gain and delay settings.

The negative gradient of the Time calibration function is a consequence of the reversal of the signals from the first and second time pick-offs to produce the STOP and START pulses respectively. The constant offset (c = 118.70 ns in this example) is closely related to the delay applied to the first Timing pulse (120 ns for this measurement), but differs by the internal delay associated with the electronic signal processing.

The energy detector is not explicitly calibrated for measurements relating to this work. The signal from the SiSB detector is used as the mass dispersive element only. Off-line processing of the HIERDA data enables the signal from different masses to be separated graphically. This makes accurate absolute calibration of the energy detector unnecessary. The calibration of SiSB energy detectors is complicated by their non-linear energy response which is mass and charge dependent, and degrades due to radiation damage during measurements [5].

3.2.3 Time Spectra vs Energy Spectra

The Time of Flight spectra may be converted directly to Energy spectra using the relationship in Equation 2.16 after correction for energy loss in the timing foils. The superior resolution of the Timing foils compared to the SiSB energy detector means that Energy spectra generated by conversion of Time spectra feature better depth resolution than Energy spectra from the SiSB detector [45].

It is the Energy axis of the Energy spectra which is normally associated with depth in the 'spectral scaling' process for interpreting ERDA data. In this method, tabulated recoil cross-sections and effective stopping powers for each layer are interpolated to determine scaling factors for each channel in the recoil spectrum. Channel by channel, the yield data are scaled to concentration and the energy scale transformed to depth. The method relies on the assumption that each layer is

sufficiently thin that the stopping power, *dE/dx*, and the scattering cross-sections are constant within the layer.

Data interpretation by simulation makes this scaling unnecessary – after iteratively refining the sample description and matching predicted energy spectra to experimental spectra, the proposed description is assumed to describe the real sample. By convention, most simulations predict energy spectra, as the various factors which influence the resolution of measurements are described theoretically as energy broadening processes.

For matching with Monte Carlo simulated spectra, the experimental data is retained as Time spectra. These are subject to a far simpler direct calibration procedure, as described above, than are energy detector spectra. The resolution of the detection system is not explicitly modelled in this work. In the case of the ToF detector, the Time resolution of the ANSTO system is approximately 340 ps [5] which is a width of approximately 2 channels for the calibration shown above. Other contributions to resolution such as finite detector solid angle and multiple scattering, produce much more significant effects and the influence of Time detector resolution may be safely neglected.

3.3 Samples

A range of different samples were chosen for consideration in this work. HIERDA measurements were conducted on the samples using different beam species and incident energies. Samples included different elements, layer thicknesses, and multi-elemental compositions of interest e.g. light elements in a heavy matrix, or more than one heavy element of similar atomic mass. Sample composition and layer thicknesses were independently known prior to the HIERDA measurements. The gold single layer samples and metallic multi-layered samples for which results have been included in this work have been previously used in other studies by other authors, and characterisations used in this work are those previously published. The tantalum pentoxide samples and their characterisations were provided by the Korean Research Institute of Standards and

Science. All samples used in this study have been manufactured specifically for previously published multiple scattering and resolution studies, or as layer thickness reference standards, and as such have been prepared to have low surface and interfacial roughness and high layer thickness uniformity.

3.3.1 Mono-elemental Gold Layers

Typical samples analysed by HIERDA users are very thin layered structures, and it is the layer interfaces that are made complex by multiple scattering. A single layer of high *Z* material is a simple structure which would demonstrate the features to be studied. Thin mono-elemental samples require shorter simulation times, and the use of a high *Z* material ensures that multiple scattering effects are well pronounced.

Mono-elemental Au layers with thicknesses between 39 and 139 nm on Si substrates were used as a benchmark for validation of the simulation, assessment of the timing efficiency improvements, and demonstration of the breakdown of the plural scattering contribution to spectra. Samples were analysed with 60 MeV and 70 MeV $^{127}I^{9+}$ ions incident at 67.5° to the sample surface normal. The measured data for the 60 nm sample were provided by Peter N. Johnston and described in [87]. Other mono-elemental Au layer samples were manufactured by Sunni Lim at the RMIT Microscopy and Microanalysis Facility.

3.3.2 Beyond the critical angle

To study plural scattering, spectra were collected from a beam-sample combination for which the detector lies beyond the critical angle for single scattering (see Equation 2.3). This configuration yields a purely multiply scattered spectrum for the scattered beam ions i.e. no single scatter contribution is present. This also provides a test for the ability of the simulation to appropriately reproduce such a result which can be seen experimentally, but cannot be predicted by any analytical simulation.

A solid Vanadium sample was analysed with a 60 MeV $^{81}Br^{8+}$ ion beam at an incident angle of 67.5˚ to the sample surface normal. The critical angle for scattering of Br from V is 39.6˚ which is less than the experimental detection angle of 45˚. The measured data were provided by Peter N. Johnston and described in [87].

3.3.3 Light elements in heavy matrix

Well characterised tantalum pentoxide reference samples were obtained from the Korean Research Institute for Standards and Science (KRISS). This tantalum-oxygen compound, of interest to material scientists as a dielectric material for high density memory devices, is an example of a light element present in a heavy matrix which is problematic for analysis by RBS, and is therefore a typical candidate for analysis by HIERDA. The relative effects of multiple scattering on heavy and light elements may be compared using the simulation.

Two reference samples were provided having Ta_2O_5 layers of 91.3 nm and 326 nm on Si substrates. These samples were analysed with ion beams of 40 MeV, 77 MeV and 97.5 MeV ^{127}I ions, incident at 67.5˚ to the sample surface normal. The author would like to thank Dae Won Moon of KRISS for providing these samples.

3.3.4 Double Layers

A series of multi-layered samples were measured that consist of two pure metallic layers, separated by an intermediate amorphous hydrocarbon layer, on a Si substrate. In some of the samples, the same metal is also present in a low percentage in the intermediate layer. Detailed descriptions are given in Table 3.3.

These multi-layered samples demonstrate the effects of multiple scattering by direct comparison of surface layers to buried layers, and show the compound effect of superposition of plural scatter

tailing features at layer interfaces. They also provide a test of the ability of the simulation to reproduce these complex artefacts. The Ag sample is used in Chapter 7 as an example of a case where the signal from the scattered beam ions overlaps with that of a sample element. ToF-E spectra from the Cr sample were shown in section 3.2 to demonstrate the data extraction procedure. The samples were analysed with ion beams of 40 MeV, and 82.5 MeV ^{127}I and ^{81}Br, incident at 65° to the sample surface normal.

These samples have previously been used in multiple scattering studies by Wielunski et al. [70] and Szilagyi et al. [69]. In those works, the experimental depth resolution obtainable for hydrogen profiling of the intermediate layer was investigated. The results were compared with predictions by the DEPTH code, including a small angle multiple scattering model (see Chapter 2). The author would like to thank Leszek Wielunski for his interest in the present study and for providing these samples.

Table 3.3 Layer descriptions of the multi-layered samples measured to generate reference spectra.

Sample No.	Layer 1	Layer 2	Layer 3	Substrate
1	Cr 135 nm	Cr 18 % : C 64 % : H 16 % 135 nm	Cr 135 nm	Si
2	W 74 %: C 26 % 110 nm	W 32 % : C 63 % : H 5 % 110 nm	W 77 % : C 23 % 110 nm	Si
3	Zr 200 nm	Zr 18 % : C 66 % : H 16 % 200 nm	Zr 200 nm	Si
4	Al 355 nm	*a-$C_{1.0}H_{0.7}Al_{0.3}$ 50 nm	Al 350 nm	Si
5	Cu 170 nm	*a-$C_{1.0}H_{0.6}$ 50 nm	Cu 173 nm	Si
6	Ag 166 nm	*a-$C_{1.0}H_{1.0}Cl_{0.1}Ca_{0.35}$ 50 nm	Ag 165 nm	Si
7	Au 145 nm	*a-$C_{1.0}H_{0.85}Cl_{0.7}$ 50 nm	Au 144 nm	Si

* hydrogenated amorphous Carbon (a-C) with trace elements as indicated

Chapter 4

Monte Carlo Ion Transport and HIERDA Simulation

Monte Carlo simulation of HIERDA spectra requires simulation of the trajectories of individual ions, which collectively make up the analysing beam. The paths of these ions are generated by considering the stochastic processes and physical forces governing the transport of the ions through matter. In this chapter, the methods used to simulate ion transport, including scattering events and energy loss processes are described. The adaptation of an existing ion transport code to the problem of generating simulated HIERDA spectra is discussed. Some HIERDA specific modifications are required such as the virtual detection of scattered and recoiled particles.

Sample results are presented to demonstrate the ability of the Monte Carlo simulation to successfully reproduce the features in HIERDA spectra which are attributable to multiple and plural scattering. It is these features that are the subject of this investigation. An example is presented of a purely multiply scattered spectrum to illustrate the successful handling of a case which is beyond the capability of traditional slab analysis methods.

4.1 Description of Ion Transport Simulation

4.1.1 Event-by-Event Simulation of Ion Beam Analysis

The principle of the *event-by-event* simulation approach is to consider the contribution to the spectrum of each ion in the analysing beam of the HIERDA experiment. That is, to reproduce the path, or 'history' of each ion incident upon the sample including its direction changes and energy loss, and ultimately its energy deposition, if any, in the detector.

Firstly an ion with a specified charge and mass is initiated with a trajectory consistent with the energy and direction of the experimental beam relative to the sample surface. As it penetrates the sample the ion will undergo electromagnetic interactions with electrons and nuclei of the sample. The transfer of momentum will result in direction and velocity changes for the ion. Ultimately, the ion and any recoil atoms displaced in these interactions, will either stop somewhere within the sample material or emerge from the sample, possibly in the direction of the detector.

A detected ion or recoil will generate a signal in the experimental system that is recorded in the output spectrum. The signal amplitude will be related to the kinetic energy of the detected particle by a calibration function established experimentally. In the simulation, the energy of an ion entering the virtual detector is known explicitly. Events depositing energy in the detector are recorded individually for later processing into a spectrum using binning parameters derived from the experimental signal processing configuration. The simulation of particle detection is discussed later in this chapter.

4.1.2 Binary Collision Model for Ion Transport

The path of the positively charged ion through the sample is dictated by electromagnetic interactions between the ion and the positively charged nuclei and the negatively charged electrons of the atoms in the sample. At any moment in time, the net force on the ion will be the sum of the

forces, dominated by the Coulomb force, due to *all* charged particles in the sample. The net force will change continuously as the position of the ion changes relative to the other charged particles. Clearly as the Coulomb force is inversely proportional to the square of the separation between charged particles, only those nearest the ion contribute significantly. In fact, the path of the ion is dominated by direction changes occurring when the ion passes very close to nuclei in the sample matrix. Screening tends to increase the influence of the nearest nucleus particularly when the distance is less than the radii of the inner electrons.

When the ion passes near to a nucleus the force on the ion due to that nucleus becomes much greater than that due to more distant nuclei according to the $1/r^2$ dependence of the Coulomb force. The net force on the ion may be approximated by the single term due to the nearest nucleus.

In this way, the path of the ion may be approximated by a series of *binary* collisions between the ion and individual single target nuclei. These binary interactions are separated by *free flight paths* assumed to be straight lines. This latter assumption follows from (i) nuclei exert no net effect when the ion is far away, and (ii) electrons will have a negligible influence on the *direction* of the ion's path, due to the very large difference in masses.

4.1.3 Monte Carlo Simulation for Stochastic Processes

Ion histories consist of stochastic processes. That is, collisions with target nuclei and energy transfer to electrons are processes that are random within appropriate probability distributions. The simulation of a random event is achieved by generating a (pseudo-) random number which is used to determine the outcome of the random experiment. The reference to 'Monte Carlo' draws the analogy with the rolling of dice, and is an expression which has been used since the time of the Manhattan Project. It refers to the idea of simulating random outcomes explicitly and individually rather than performing calculations using average values or distributions of random variables.

The main stochastic events to be simulated are (i) *Coulomb scattering* between the incident ion and target nuclei, and (ii) *electronic stopping* – the transfer of energy from the incident ion to electrons of the target material. The Monte Carlo simulation of a Coulomb scattering event is described here, followed by a discussion of the Continuous Slowing Down approximation of electronic energy loss.

4.1.4 Monte Carlo Simulation of Coulomb Scattering

The scattering equations governing the energy transfer and direction changes of the ion and the recoil atom (described in section 2.2) are usually solved in *centre of mass* co-ordinates as depicted in Figure 4.1. The force between the two particles acts along the line between them, and the relative motion of the particles can be reduced to that of a single particle moving in a central potential centred at the origin of the C of M co-ordinates (more details are given in section 4.1.6). The relevant centre of mass relationships are:

Energy in the C of M system:

$$E_{CM} = \frac{M_2}{(M_1 + M_2)} E_0 \tag{4.1}$$

Recoil scattering angle:

$$\phi_{CM} = 2\phi \tag{4.2}$$

Ion scattering angle:

$$\theta_{CM} = \pi - \phi_{CM} = \pi - 2\phi \tag{4.3}$$

When $M_1 \leq M_2$:

$$\theta_{CM} = \theta + \sin^{-1}\left[\frac{M_1}{M_2}\sin(\theta)\right] \tag{4.4}$$

or for $M_1 > M_2$, θ_c is double valued:

$$\theta_{CM} = \begin{Bmatrix} \theta + \sin^{-1}\left[\frac{M_1}{M_2}\sin(\theta)\right] \\ or \\ \pi + \theta - \sin^{-1}\left[\frac{M_1}{M_2}\sin(\theta)\right] \end{Bmatrix} \tag{4.5}$$

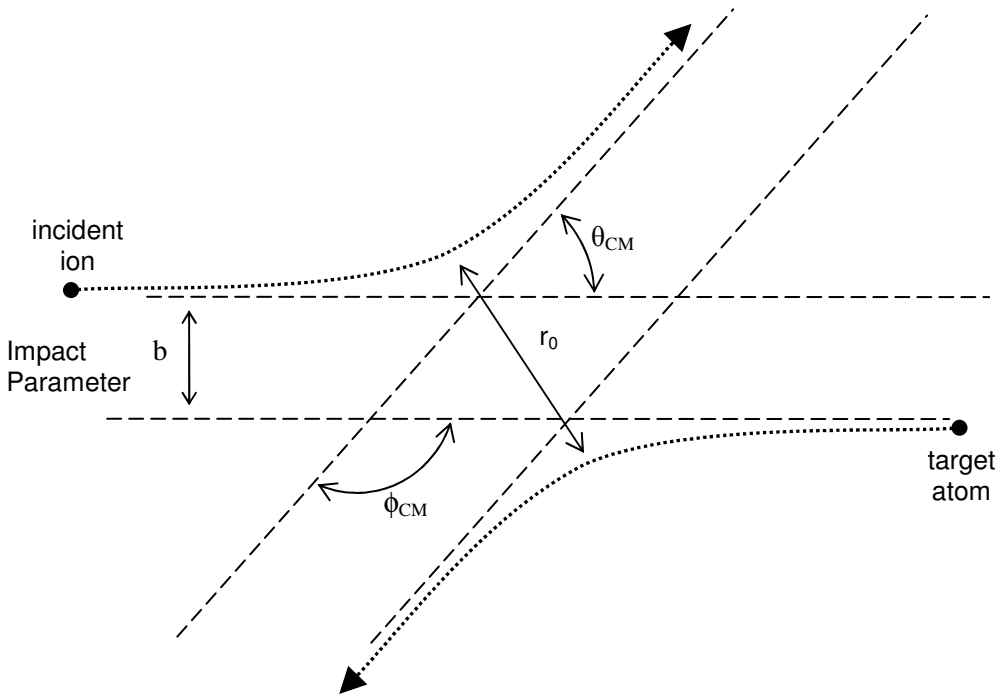

Figure 4.1 Ion-atom scattering in Centre-of-Mass co-ordinates showing Impact Parameter, *b*, distance of closest approach, r_0, and the C of M scattering and recoil angles θ_{CM}, and ϕ_{CM}.

4.1.5 Impact Parameter

The magnitude of the collision is determined by the *impact parameter*, *b*, which is defined as follows. The straight line path of the ion would pass a distance *b* from the nucleus in the absence of the repulsive Coulomb force between the particles (see Figure 4.1). An impact parameter of zero would represent a 'direct hit' or 'knock-on' collision in which the recoil would be in the direction

of the incident ion path, and the post-collision direction of the ion would be either unchanged or backscattered along the incident path.

For a large impact parameter, the ion passes far from the target nucleus, the repulsive Coulomb force is small, and the incident ion suffers little deflection from its original path. The recoil atom receives a small fraction of the incident energy, but has a large recoil angle, ϕ (see Figure 2.2).

Small impact parameters yield a larger deflection for the incident ion, a larger fraction of the incident energy is transferred to the recoil and the recoil's direction is closer to that of the incident ion.

The impact parameter is related to the probability of scattering as a function of angle as described for Rutherford scattering by equations 2.4 and 2.5. The 'glancing' deflection of large impact parameter collisions are more probable than large angle scattering events due to the larger area of the annular ring between b and $b+\delta b$ when b is large (see Figure 4.2). However, these glancing collisions have the least effect on the ion's direction and energy and are the least likely to generate recoils of interest. They are responsible for the small directional deviations referred to as 'multiple scattering'.

Close collisions due to small impact parameters are lower probability events, but are responsible for the ejection of energetic recoil atoms, and the large direction changes of the incident ions which enables them to be scattered into the detection system of the HIERDA experiment.

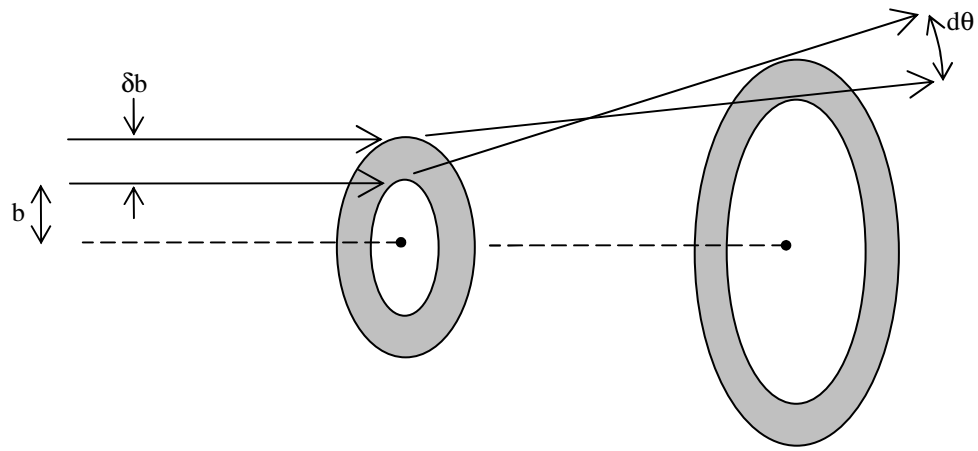

Figure 4.2 Incident particles entering the ring between b and $b+\delta b$ are scattered uniformly into a ring of angular width $d\theta$.

4.1.6 Selection of Target Atom and Impact Parameter

In the MC simulation, the elemental species of the target atom in each binary collision is randomly selected from a stoichiometrically weighted distribution of the elements present in the sample. The magnitude of the scattering event is determined by randomly generating an impact parameter, b, within a $1/r^2$ weighted distribution between 0 and b_{max}, where b_{max} is the largest possible impact parameter based on the average interatomic separation of atoms in the target as calculated from the atomic density assuming an amorphous distribution. For efficiency reasons, b_{max} can be forced to be smaller when coupled with long free flight paths. This will be discussed in detail in section 4.1.8.

The scattering occurs within a plane defined by the post-collision trajectories, however this plane may be oriented at any azimuthal angle with respect to the original ion trajectory with equal probability. Hence another random number is generated between 0 and 2π to determine the azimuthal orientation of the scattering plane.

The randomly generated impact parameter is used to determine the energy transfer and the scattering angles θ and ϕ. These angles, together with the azimuthal orientation, ψ, are used to compute the new ion and recoil trajectories.

For energies above a pre-determined threshold, the unscreened Coulomb (Rutherford) potential is used for computing efficiency reasons and the relationship between θ_{CM} and b is

$$\sin^2\left(\frac{\theta_{CM}}{2}\right)=\left[1+\left(\frac{2bE_c}{z_1 z_2 c^2}\right)^2\right]^{-1} \tag{4.6}$$

At lower energies, the distance of closest approach of the ion to the target atom is greater, and electronic screening cannot be neglected. As discussed in Chapter 2, the influence of charge state further complicates the screening between two atoms. Ziegler, Biersack and Littmark (ZBL) developed an *interatomic potential* function, depending only upon the interatomic separation, describing the force between the particles including the influence of screening by atomic electrons. The screening was described by a fitted *universal screening function*. The complete derivation (available in [17]) is lengthy, but a summary is included below.

The ZBL Universal Interatomic Potential, $V(r)$, is specified as

$$V(r)=\frac{z_1 z_2 e^2}{r}\Phi\left(\frac{r}{a}\right) \tag{4.7}$$

in terms of the ZBL fitted Universal Screening Function, $\Phi(x)$:

$$\begin{aligned}\Phi(x)=0.1818e^{-3.2x}+0.5099e^{-0.9423x}\\ +0.2802e^{-0.4029x}+0.02817e^{-0.2016x}\end{aligned} \tag{4.8}$$

expressed as a function of the reduced separation, x:

$$x=\frac{r}{a} \tag{4.9}$$

for the screening length

$$a = \frac{0.8853 a_0}{\left(z_1^{0.23} + z_2^{0.23}\right)} \tag{4.10}$$

Where a_0 = 0.529 Å is the Bohr radius.

The scattering angle θ_{CM} is then shown to be related to the impact parameter, b by,

$$\cos\left(\frac{\theta_{CM}}{2}\right) = \frac{b + \rho + \delta}{r_0 + \rho} \tag{4.11}$$

Where ρ is a characteristic radius related to distance of closest approach, r_0 (see Figure 4.1)

$$\rho = 2\frac{E_{CM} - V(r_0)}{-V'(r_0)} \tag{4.12}$$

and E_{CM} is the C of M energy from Equation 4.1

$$E_{CM} = \frac{M_2}{M_1 + M_2} E_0 \tag{4.13}$$

r_0 is obtained from the relationship

$$1 - \frac{V(r_0)}{E_c} - \left(\frac{b}{r_0}\right)^2 = 0 \tag{4.14}$$

which relates the Coulomb energy at the distance of closest approach, to the kinetic energy of the system. In a direct knock-on collision, these two quantities are equal.

The δ in Equation 4.6 is a small fitted correction term which ensures that the formula asymptotically approaches the unscreened Coulomb (Rutherford) result in the high energy limit (see [17] for details of the empirical fitting of δ for any given potential function).

4.1.7 Calculation of Post-Collision Trajectories

With the C of M scattering angle θ_{CM} known, the laboratory coordinate scattering angle is

$$\theta = \tan^{-1}\left(\frac{\sin(\theta_{CM})}{\cos(\theta_{CM})+\frac{M_1}{M_2}}\right) \tag{4.15}$$

and with a randomly generated azimuthal scattering angle ψ in [0, 2π), the direction cosine for the ion after the i^{th} collision is

$$\cos(\alpha_i) = \cos(\alpha_{i-1})\cos(\theta) + \sin(\alpha_{i-1})\sin(\theta)\cos(\psi_i) \tag{4.16}$$

with similar expressions for the recoil particle using the simple relationship in Equation 4.3:

$$\phi = \frac{\pi - \theta_{CM}}{2} \tag{4.17}$$

so that the direction cosine of the target atom recoiled in the i^{th} collision is

$$\cos(\alpha_{recoil}) = \cos(\alpha_{i-1})\cos(\phi) + \sin(\alpha_{i-1})\sin(\phi)\cos(\psi_i - \pi) \tag{4.18}$$

The energy transferred to the target atom in the collision is given by

$$\begin{aligned}\Delta T &= \frac{4M_1M_2}{(M_1+M_2)^2}E_0\sin^2\left(\frac{\theta_{CM}}{2}\right)\\ &= \frac{4M_1M_2}{(M_1+M_2)^2}E_0\cos^2(\phi)\end{aligned} \tag{4.19}$$

as in equation 4.2.

4.1.8 Simulation of Electronic Stopping

Between nuclear scattering events, the incident ions, and displaced energetic recoils, are transported in straight 'free flight paths' to the location of the next scatter. Along these paths, the ions are subject to electronic stopping – the transfer of energy to the electrons of the target material. While these energy transfers are in reality discrete events, they are treated in the simulation as a continuous process along the length of the free flight path. The individual energy transfers are

extremely small due to the large difference in masses between the ion and an electron, and the distances between individual electron scatterings very small compared to the free flight path length. The continuous energy loss approximation is justified, and an enormous amount of computation is avoided.

Electronic stopping power is assumed to be a function of the energy of the ion at the beginning of each free flight path interval. The stopping power *dE/dx* is applied over the length of the interval, assuming that the free flight path length is sufficiently short that any *change* in *dE/dx* due to the change in *E* over the interval is negligible.

The length of the free flight together with the maximum impact parameter is chosen to ensure that all collisions with an energy transfer above a threshold, T_{min}, are accounted for. The maximum impact parameter, b_{max}, is chosen to ensure the energy transfer T_{min}, then the flight length L is chosen such that there is one target atom in a cylinder of volume N^{-1}, where N is the atomic density of the sample in atoms/Å^3, and the cylinder has radius b_{max} and length L.

$$\pi b_{\max}^2 L = N^{-1} \tag{4.20}$$

so

$$L = \left[\pi b_{\max}^2 N\right]^{-1} \tag{4.21}$$

For calculation efficiency reasons, the free flight length L is made longer at higher energies in recognition of the reduced scattering cross sections with corresponding reduced impact parameters.

The electronic energy loss over the interval L is

$$\Delta E_e = LNS_e(E) \tag{4.22}$$

where $S_e(E)$ is the electronic stopping cross section. The cross section is based on measured data for H ions, but for the stopping of heavy ions, Ziegler, Biersack and Littmark [17] developed a semi-empirical formalism by scaling against proton stopping powers. The heavy ion scaling rule

was described in detail in section 2.2.4. An analytical function was fitted to existing experimental data for H ions, and a velocity proportional correction applied to improve accuracy for low energy ions. The calculation of the heavy ion electronic stopping proceeds by incorporating the following:

(i) a velocity proportional charge state estimation which accounts for the partial ionisation of the ion due to electron stripping and capture as it penetrates the target;

(ii) a screening length describing the extent of the electron cloud of the ion as its charge state varies; and

(iii) an *effective charge* which deals with the increased energy transfer to target electrons which penetrate the ion's electron cloud.

A detailed description may be found in Chapter 3 of [17]. Bohr Straggling is applied to the energy loss over the interval using Equation 2.14.

This method contains a number of simplifications and assumptions designed to keep the calculation efficient enough for use in Monte Carlo simulation. The limitations of the method are described in detail in [17], and comparisons with experimental data showed the calculation to be accurate to within approximately 10%.

As discussed in Chapter 2, stopping powers are the least well known of the parameters governing the ion path. Discrepancies exist between theory and experimentally measured values and even the validity of the concept of velocity proportional effective charge state has been questioned [97]. A discussion of these inconsistencies at the 16th International Conference on Ion Beam Analysis [98] may be summarised by the statement by one participant: "your gold is not my gold". It was acknowledged that individual sample differences due to manufacturing processes and parameters were the likely cause, and that the variations in measured stopping powers were unlikely to be resolved in the near future.

The implication for MC simulation of HIERDA spectra is that substantially more work needs to be done to develop a reliable formalism for calculating heavy ion stopping powers. Using the present

approach, stopping of heavy ions is generally underestimated, leading to the overestimation of layer thicknesses when spectrum matching between experiment and simulation.

While this may preclude the use of MC simulation for routine analysis of experimental data, the deficiency can be compensated for by the use of overstated layer thicknesses. This enables experimental and simulated spectra to be overlayed for comparison, and the use of Monte Carlo simulation in this study as a tool for understanding the significance of multiple scattering and plural scattering is not compromised.

4.1.9 Application of Monte Carlo Simulation to HIERDA

It remains to be shown that the MC ion transport theory described above can be applied to the study of HIERDA and the effects of multiple and plural scattering.

A preliminary study by Johnston et al [82] showed that these features could be seen in a spectrum even though the statistics achievable with the unmodified code were quite poor. They had trialled large values of T_{min} in an attempt to reduce simulation times, but essential spectral features were lost. The trial did however give some confidence that MC simulation was worth pursuing. In early stages of the present work, statistically reasonable spectra were generated by compiling the results from many simulations run on more than 20 computers. The results were encouraging, however a total CPU time of 53 days for a single spectrum indicated that efficiency enhancement would represent a major component of further work in this area.

It will be shown in the next section that an existing MC Ion Transport code can be adapted to the generation of HIERDA spectra and successfully reproduce the complex features present in the experimental spectra that are attributable to multiple and plural scattering. Chapter 5 outlines a number of techniques and strategies applied to address the issue of computing efficiency.

4.2 Simulation of HIERDA spectra

The complete simulation of the output spectra of HIERDA experiments requires ion transport modelling as described in the preceding section (4.1), coupled with simulation of the recoil atom detection process.

Fortunately, the development of Monte Carlo codes for modelling ion transport in matter has been the subject of a large body of work by several groups since as far back as the 1960's (see for example [99-101]). An existing code has been selected for adaptation to HIERDA simulation based on its history of development which includes *execution speed* as a primary focus. This is based on the very low inherent efficiency of the experimental measurement. A very large number of incident particles are required to generate a sufficient number of detected recoils.

There are a number of different detector systems in use for HIERDA measurements. Research groups have various preferences for the presentation of experimental data, usually based on the detector type and data acquisition system in use at a given facility. At the ANTARES facility at Lucas Heights where the experimental data for this study were acquired (see Chapter 3), the detector in use is a Time of Flight - Energy (ToF-E) telescope. Two dimensional spectra are plotted against ToF and Energy axes and one dimensional spectra are routinely viewed as Time of Flight spectra. In this work, simulation output is manipulated into a form which allows direct comparison with experimental data. Chapter 3 provides a detailed description of the experimental configuration.

4.2.1 *FasTrim* Ion Transport Code

TRIM is a Monte Carlo ion transport code developed as a product of a comprehensive study by Ziegler, Biersack and Littmark [17] of the transport of ions in matter. The primary application for that work was ion implantation studies for materials modification rather than materials analysis.

The parameters of interest were ion range distributions and vacancy production for defect density prediction.

The simulation code developed for this work was built starting with a fast FORTRAN version of TRIM developed by R. A. Brown and H. J. Hay at the Australian National University Department of Electronic and Materials Engineering. Their code, called "*FasTrim*", was developed for implantation and radiation damage concentration profiling [102-104]. The original TRIM code from 1985 was written in FORTRAN and later converted to BASIC for consistency of execution across computer platforms by eliminating variations due to compiler differences. For efficiency reasons, Brown and Hay converted TRIM-88 (version 1.4) back to FORTRAN and implemented a number of programming strategies to improve execution times. Many calculations are optimised in terms of pre-calculated reusable variable combinations to minimise the number of operations performed. Sub-routine calling and parameter passing are minimised by the extensive use of global variables.

The adaptation of FasTrim to this HIERDA application involved some modifications to the code and the addition of various routines to handle those aspects which are HIERDA specific, such as the experimental detection of recoils. Some redundant functionality was identified and removed to reduce processing time. A number of changes required related to the accumulation of statistical data during a simulation. A HIERDA simulation requires such a large number of interactions to be modelled that many calculations were subject to numerical overflows. This serves as an indication of how this exercise is pushing computational limits.

4.2.2 Simulating Ion and Recoil Detection

The simulation generates an output file listing all particles which emerge from the surface of the sample. For each backscattered projectile ion and sputtered recoil atom, the species, energy and

direction cosines are recorded. This list is post-processed to simulate detection by a virtual ToF–E telescope detector of the type described in Chapter 3.

The direction cosines are compared to the limits of the solid angle subtended by the second timing foil of the experimental detector. Only particles which intersect both timing foils will generate a complete time of flight signal. In the simulation, the detector solid angle can be enlarged to improve detection efficiency (see Chapter 5 for more details regarding efficiency improvements).

The energy loss in the carbon timing foils is accounted for, before the corrected energy is converted to a Time of Flight, using the flight length of the telescope. The energy loss in the foils is calculated using the known areal density of the carbon and the stopping powers generated using the same routines as employed in FasTrim. Here the *total* stopping power is used inclusive of both *nuclear* and *electronic* stopping. A program has been written that generates stopping powers in carbon for all ion species at a range of energies from 100 keV – 100 MeV. The results are tabulated in a data file for access by the detection routine.

No attempt is made here to accurately model all aspects of the detector. In particular, the absolute efficiency of the detector is not reproduced i.e. the idealised virtual detector is assumed to be 100 % efficient. The energy of each particle satisfying the solid angle and timing constraints of the virtual detection system is recorded. The energy and timing resolution of the detector have not been modelled. The energy detector signal, used in practice for mass separation, is not required in the simulation. The timing resolution is negligible compared to other energy broadening contributions such as energy straggling and detector solid angle, particularly in light of the use of enlarged solid angles for the virtual detector.

The ToF-E telescope is the only detection system considered in this work. In principle, any detector could be modelled and the scattered ions and recoils could be ‘post processed’ for the relevant detection system. The simulation could therefore be used to compare the output spectra of different

systems, and aid the choice of detector system for a particular application. Implementation of some of the optimisations discussed in the following chapter would require knowing the solid angle and Minimum Detectable Energy of the detector system to be incorporated, prior to running the simulation.

4.2.3 Generating Simulated Spectra

For direct comparison with experimental data, simulated Time of Flight spectra are generated using the bin-width and offset obtained from the experimental Time of Flight calibration (see section 3.2.2).

As the number of detected particles in a simulation is much lower than for the corresponding experiment, simulated data is generally binned more coarsely to reduce statistical noise in the spectrum. A utility program has been created for post-processing the simulation output. It interactively prompts the user for the required experimental parameters, simulates the detection process, and generates Time of Flight spectra for all elements defined in the FasTrim input file.

4.3 Results

To demonstrate the successful application of the Monte Carlo simulation to HIERDA, the program has been applied to two experimental samples. The first is a thin (60 nm) Au layer on a Si substrate to demonstrate the output for a discrete layer. The second is a pure V sample analysed by a $^{81}Br^{8+}$ beam such that the detection angle is beyond the critical angle for scattering. All detected Br ions in this configuration must have been multiply scattered to reach the detector.

The results of the simulations are compared with experimental measurements of both the scattered projectile ions and the recoiled target atoms.

4.3.1 Mono-elemental Au layer on Si Substrate

A well characterised sample consisting of a single thin (60nm) Au layer deposited onto a Si substrate was analysed using 60 MeV ^{127}I ions. This single layer demonstrates the features which will be present in the spectrum of the simplest possible sample structure. The output spectra of more complicated samples will essentially consist of convolutions of these features for more elements and more layers (see Chapter 2).

Figure 4.3 shows the simulation results overlayed with the experimental data for the scattered I (panel (a)) and the recoiled Au (panel (b)). The overall shape of the spectra agree very well although it is apparent that the simulated scattered I spectrum is narrower than the experimental spectrum. The width of the Flight Time spectra represents the energy loss of ions traversing the thickness of the layer. Thus, the insufficient width of the simulated spectrum represents an underestimation of the stopping power of I in Au at these energies within the simulation. This deficiency in stopping powers predicted by TRIM has been previously observed by Elliman and co-workers in a HIERDA depth resolution study [33], and by Climent Font et al. [40]. The deficiency can be readily compensated for by increasing the layer thickness in a simulation. Figure 4.4 shows the simulated spectrum from a 75 nm Au layer, overlayed with the experimental data from the measurement of the 60 nm layer. The widths of the two spectra agree.

In reproducing the shapes of the scattered and recoiled spectra, the simulation is correctly reproducing features attributable to multiple and plural scattering. The surface edge of each spectrum, that is the high gradient at the low Flight Time end, features the high energy 'knee'. This feature is due to the detection of ions and recoils which have been double scattered to reach the detector, and are detected with a higher energy than ions scattered once from the near surface region of the sample. The product of kinematic factors (see Equations 2.1 and 2.2) for two scatters of about 22.5˚ is greater than the kinematic factor for a single 45˚ scatter.

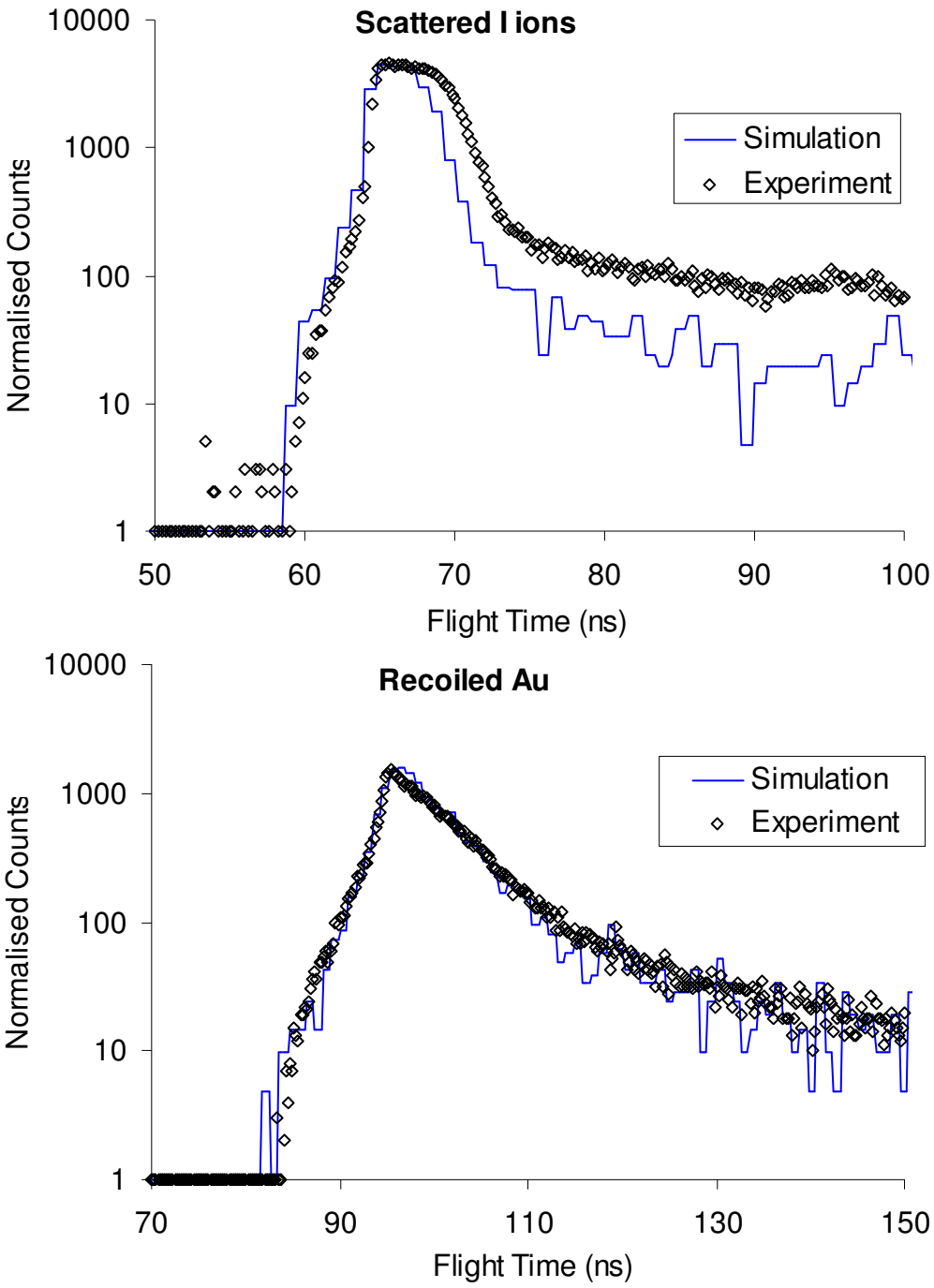

Figure 4.3 Comparison of Experimental and Monte Carlo simulated Time of Flight spectra for a 60 nm mono-elemental Au layer on Si substrate analysed using 60 MeV I ions. (a) Scattered I ions, and (b) Recoiled Au atoms.

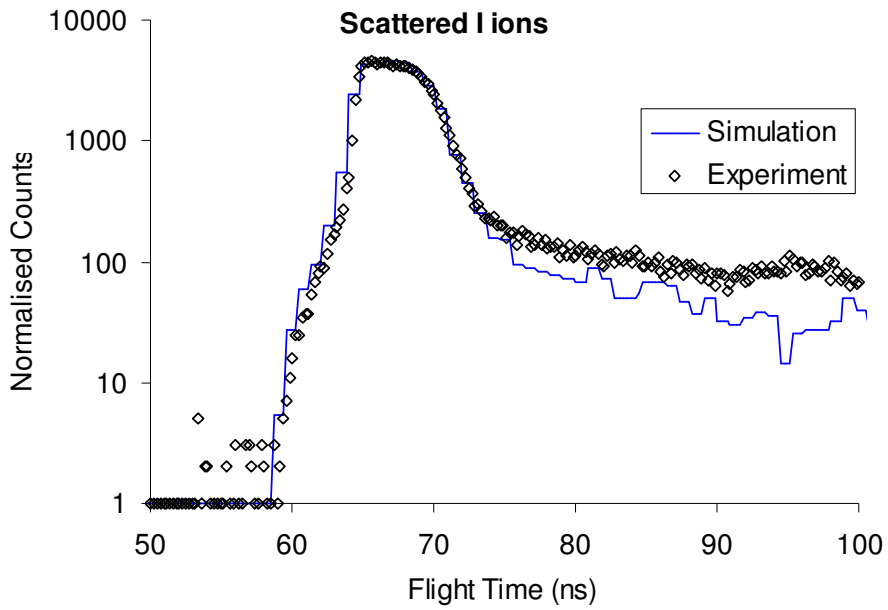

Figure 4.4 Simulated scattered I spectrum from a 75 nm Au layer compared with experimental data from a 60 nm Au layer.

In will be shown in Chapter 6 that the low energy (i.e. long flight time) tailing is also caused by multiple and plural scattering of ions and recoils in the Au layer. Multiple interactions cause these atoms to lose more energy and be detected with a much reduced energy that is not simply related to their origin within the sample. In particular, they are not a result of interactions in the sample beyond the back of the Au layer as their reduced energy would suggest if the energy axis was scaled to depth in the usual manner of slab analysis. As will be shown in Chapter 5, this low energy tailing is not attributable to substrate effects at all. The low energy tailing in the scattered I spectrum beyond flight times of 75 ns is underestimated by the simulation. This cannot be accounted for by substrate modelling, and is probably evidence of some inadequacies in the 'universal' potential used by TRIM.

4.3.2 Scattering of Br from V Beyond the Critical Angle

The second example is chosen to exploit the kinematic relationships shown in equations 2.1 and 2.2 to produce a spectrum of purely multiply scattered particles to demonstrate the ability of Monte Carlo simulation to deal with an extreme case. When the mass of the projectile exceeds the mass of

the target atom, there is a maximum possible scattering angle for the projectile. This is called the *critical angle* for scattering, θ_c, and is given by

$$\theta_c = \sin^{-1}\left(\frac{M_2}{M_1}\right) \tag{4.23}$$

The critical angle is sometimes exploited in ERD measurements to avoid the need for a range foil to stop detection of scattered projectiles [10]. It is assumed that scattered projectiles cannot be scattered into the detector and therefore do not need to be controlled for. Experimental measurements will show that this is not necessarily the case for HIERDA, as some projectiles may be multiply scattered into the detector. Traditional 'slab' analysis would not predict *any* scattered yield, and this serves as a good test case for the Monte Carlo model.

An experimental configuration consisting of a solid V target analysed by a ^{81}Br beam is chosen so that the critical angle of 39˚ is less than the detection angle of 45˚. Figure 4.5 shows a comparison of experimental data with simulated spectra for scattered and recoiled ions from 60 MeV ^{81}Br ions on V. The recoiled spectrum shows good agreement with experimental data and is used to normalise the two data sets. A comparison of experimental data and simulation for the backscattered Br spectrum shows a similar magnitude and shape, but the simulation exceeds the experimental data for low energy ions with flight times above 110 ns.

Overestimation of low energy tailing may be due to the relative detector efficiency between the simulation and the actual Time of Flight detector. The simulated detector is 100 % efficient – all particles reaching it with sufficient energy not to be rejected based upon timing cut-offs, are recorded. As described in ToF-E detector efficiency studies by Zhang and Whitlow et al. [105], the real detector will suffer some nuclear scattering in the timing foils and other components of the detector structure which will remove some ions from the line of the detector resulting in no Time or Energy signal being generated. As this scattering will preferentially occur with the lower energy particles due to the higher cross sections, the net ratio of high to low energy detections will be

increased. This will not happen in the simulated detector so the ratio will be slightly lower. This does not account for the underestimation of the tailing in the spectrum of I scattered from Au.

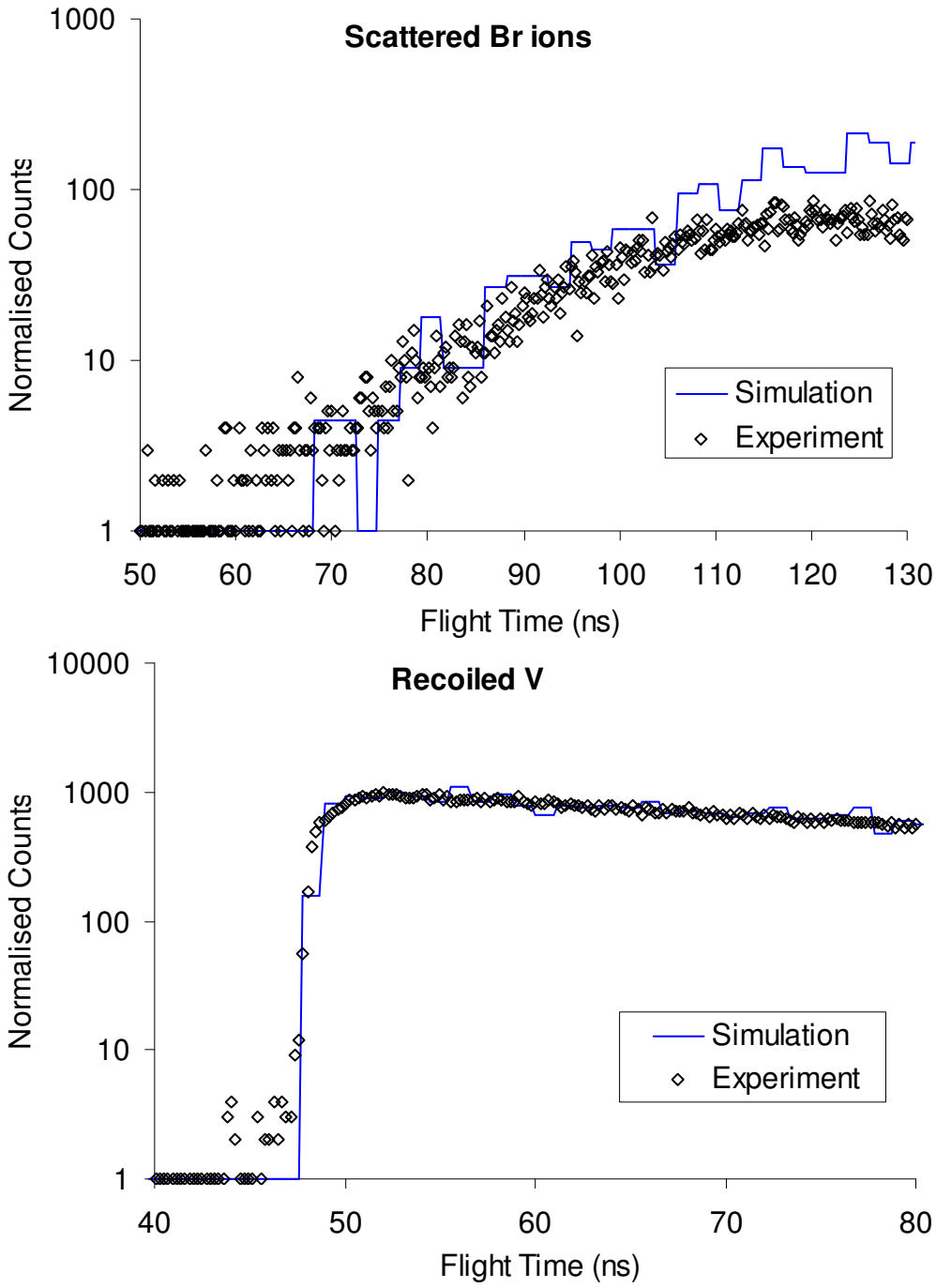

Figure 4.5 Comparison of Experimental and Monte Carlo simulated Time of Flight spectra for a solid V target analysed using 60 MeV ^{81}Br ions beyond the critical angle for scattering. (a) Purely multiply scattered Br ions, and (b) Recoiled V atoms.

4.4 Conclusion

It has been shown that a Monte Carlo ion transport simulation based on the widely known TRIM code, can be modified and applied to the simulation of output spectra from Heavy Ion Elastic Recoil Detection Analysis experiments. The fundamental spectral shape is very well reproduced including features that can be attributed to multiple and plural scattering in the experimental sample. There are some differences in the width of the main peak in the case of the I projectiles scattered from the Au sample which indicate a deficiency in stopping power as used in the simulation for some ion species and energy ranges. This can be easily compensated for by adjusting layer thicknesses in the simulation. The magnitude of low energy tailing is overestimated for Br ions multiply scattered from V beyond the critical angle, and underestimated for I ions scattered from Au. This tailing is correctly modelled for recoiled atoms in both cases.

The simulation correctly reproduces the *shape* of each spectrum which is predominantly defined by the contribution from multiple and plural scattered ions and recoils which is the subject of this study. This correlation indicates that the simulation is appropriately modelling the complex histories of these particles, and is able to include these effects in a way which cannot be achieved using conventional analytical model 'slab' analysis techniques.

To use Monte Carlo simulation to reproduce and identify the multiple and plural scattering contribution to spectra, will require supplemental programming to identify and record parameters which classify particles and individual events within the histories of these particles. This additional processing burden will result in even longer simulation times which are already so unwieldy as to render the MC approach impractical for anything more than simplified, very specific investigations. Thus the need to improve the efficiency of the calculations became a major focus of this work. In the following chapters, techniques developed to reduce processing time will be described, and the code used to investigate the discrimination and identification of multiple scattering contributions to spectra.

Chapter 5

Efficiency improvements

One of the greatest impediments to successfully simulating HIERDA measurements using MC methods is processing time. A HIERDA experiment consists of a large number of incident ions directed at a sample, and each ion then undergoes many scattering events during its passage through the sample. Simulating the entire experiment requires an enormous number of calculations to be performed. Many of these calculations are relatively time consuming operations such as solving the scattering integral or determining heavy ion stopping coefficients from data in a lookup table. It is therefore important to (a) perform calculations as efficiently as possible, and (b) minimise the time spent processing events that do not contribute to the output results.

The FASTRIM code contains a number of *programming* strategies to increase the speed of calculation. These include pre-calculation of some algebraic combinations of variables, loading lookup tables into RAM, and the choice of fast subroutines for generating random numbers. FASTTRIM also employs some *simulation* strategies to reduce the number of calculations required to model each ion path. These include the use of variable length straight line free flight paths (described in 4.1.2 and 2.2.4) and calculating stopping of heavy ions by scaling against proton stopping power (described in 4.1.8).

The original application of TRIM to ion implantation required that every ion path was followed in detail to an arbitrarily low energy threshold to generate the implantation depth profiles required. The application of the code to a different experimental activity, while responsible for the dramatic

increase in calculations required, allows the possibility of employing other techniques to improve the efficiency of the MC simulation. A number of efficiency improvements to the FasTrim code have been developed to improve the practicability of using MC simulation to generate HIERDA spectra and to study the contributions of Multiple and Plural Scattering.

5.1 Ion Tracking Reduction

Many of the ions incident upon the sample during a HIERDA measurement do not contribute to the output spectra. The close collisions which result in large deflections and the ejection of energetic recoils are low probability events for medium to high energy ions. Most ions of the analysing beam will not have such interactions until near the end of their range in the sample when their energy is very low and this scattering merely influences their final resting place within the sample. Of those that do have significant scattering events, few will generate an ion or recoil that reaches the sample surface, and fewer still will actually reach the detector. The detector subtends only a very small solid angle at the beam spot on the sample, so only a small fraction of possible scattering paths will ultimately lead in the direction of the detector. Even an ion which does exit the sample surface travelling in the direction of the detector must do so with an energy above the *minimum detectable energy* of the detection system in use.

Ideally in the simulation, to minimise calculation time, only ions which contribute to the output spectrum would be followed. However, the paths of ions in the simulation are governed by the same forces as those acting upon the real ions and are subject to the same statistical distribution of outcomes such as direction of scatter, and fraction of energy transferred in each collision. Consequently there are many simulated ion paths initiated which do not lead to detector interaction events. To reduce the total processing time of the simulation, the time spent following those ions that don't contribute to the measured output can be reduced.

It is necessary to identify conditions which may be used to classify individual ions as being of interest or not based on their likelihood of generating a detection event. Broadly, an ion or recoil must either be (i) travelling towards the detector with sufficient energy to reach it and be detected, or (ii) it must be kinematically possible for the ion to be scattered into the direction of the detector with enough energy remaining to reach the detector and for the detection event to occur. Parameters which may be used to assess this likelihood include:

(i) The instantaneous direction of the ion's trajectory

(ii) the kinetic energy of the ion

(iii) the position of the ion – in particular its depth in the sample

(iv) the mass of the ion

(v) the masses of other atomic species in the sample

5.2 Substrate Modelling

Typical samples analysed using HIERDA are thin layered structures manufactured on or implanted into substrates such as Si or SiO_2. To ensure analysis of the entire depth of interest of the sample, the beam species and energy must be chosen such that the range of the incident ions in the sample is sufficient to reach the greatest depth of interest (allowing for the elongated path lengths associated with the grazing angle geometry) with enough energy to scatter and still reach the surface again, or to generate a recoil which can reach the surface. Thus, many ions traverse the depth range of interest in the sample and are simply embedded into the substrate. The fraction of the path in the substrate may be quite long and therefore time consuming in the simulation. Exclusion of the bulk substrate from the simulation can reduce the processing time required, with little loss of information. A thin layer of substrate can be included for the purpose of studying interfacial diffusion or to provide information regarding the thickness of overlying layers. Ions which penetrate beyond this depth can be considered to have been 'transmitted' beyond the sample and the next ion is initiated.

Consider the role of the substrate for the 60 nm thick Au layer on Si substrate sample analysed with 60 MeV I. The range of 60 MeV I in Au is 4.37 μm, approximately 27 times the 157 nm path length through the 60 nm Au layer at the incident angle of 67.5°. In the experiment, most ions will be implanted deep into the Si substrate, and in the simulation most of the processing time will be spent on the paths within the Si. Figure 5.1 and Figure 5.2 show comparisons between the experimental data and two simulations. In the first simulation, the substrate is modelled as a thick (500 nm) layer, and in the second simulation as a thin (1 nm) layer to examine the influence of the substrate on the scattered I (Figure 5.1) and recoiled Au (Figure 5.2) spectra. As before, the Au layer is made 75 nm thick in the simulations to correct for stopping power deficiencies.

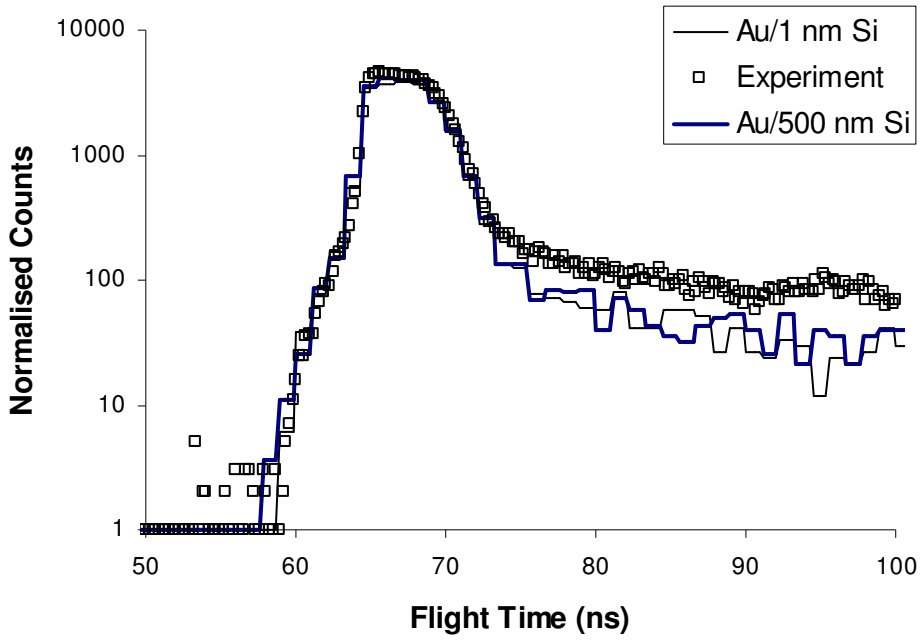

Figure 5.1 Scattered I from 60 nm Au layer: comparison of simulations with (i) 1 nm, and (ii) 500 nm Si substrate modelled.

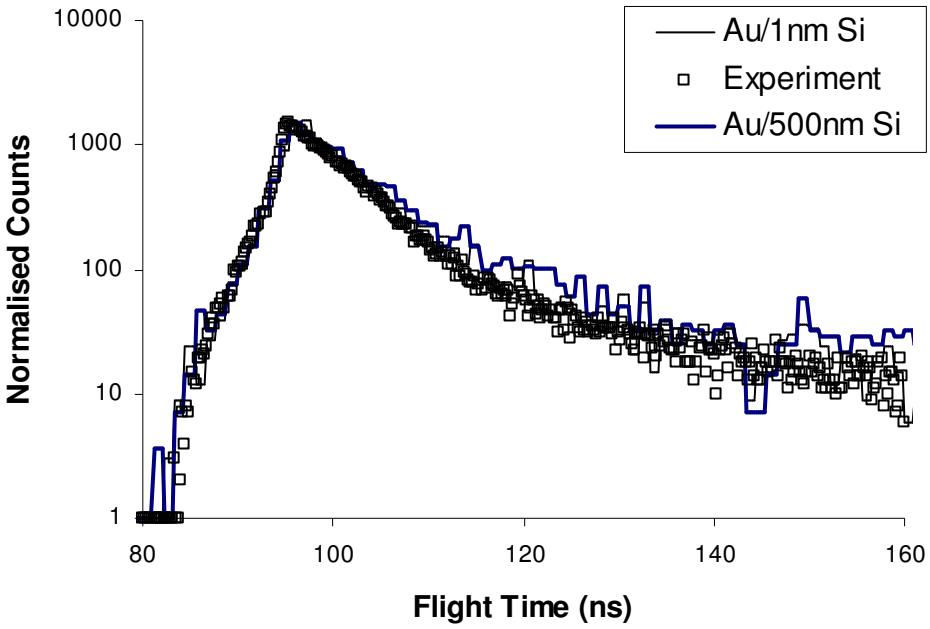

Figure 5.2 Recoiled Au from 60 nm Au layer: comparison of simulations with (i) 1 nm, and (ii) 500 nm Si substrate modelled.

The two simulations are in agreement confirming that the bulk Si substrate contribution to the scattered I and recoiled Au spectra is negligible. This result for HIERDA simulation is in contrast to a finding by Li and O'Connor [80] who found that in MC simulation of medium energy Heavy Ion Backscattering Spectrometry (HIBS), the substrate contributed to the yield of backscattered C, Ne, Si, Ar, and Kr ions for energies between 10 and 100 keV. HIBS at these energies is used to detect trace quantities of heavy ion impurities on Si wafer surfaces. The cross sections for backscattering are sufficiently high, even for light target elements such as Si, for the substrate to contribute to the backscatter spectrum in the absence of overlying layers. In HIERDA experiments, the incident energy of the beam is high enough that significant scattering of the heavy ions from the light substrate is rare until the ions are deep in the sample with reduced energy, and unlikely to re-appear at the surface.

Modelling the Si substrate as 1 nm thick instead of 500 nm reduced processing time from 5776 s to 1133 s per 10^6 ions – a time reduction of 80 %. This range reduction technique also allows for the

implementation of another efficiency enhancement involving significant path prediction based on impact parameters. This technique will be described in sections 5.4 to5.6.

5.3 Ion Transport Cut-off Energy

Ions are transported through the sample, losing energy via electronic and nuclear stopping, until their energy reaches a cut-off energy E_{fin}. By default, E_{fin} is set at the lowest displacement energy, E_d, of any element in the sample, but may be set higher by the user. At very low energy, ions are no longer capable of generating detectable recoils, and tracking of the ion may be abandoned.

There is a processing time advantage in setting E_{fin} as high as possible. As the ion energy decreases near the range the scattering cross section increases (Eqn 2.4) and the modelled free flight path length decreases. This results in more collisions and stopping intervals being calculated per unit path length and hence is the most time consuming part of the ion path simulation.

We exploit the *minimum detectable energy* (MDE) of the Time of Flight detection system (section 3.1.2), and the kinematic relationship between particles (Equations 2.1 and 2.2) to set a highest possible cut-off energy $E_{fin}(Z)$ for each ion species present in the simulation. The MDE for a particle of mass M is given by

$$MDE(M) = \frac{ML^2}{2T_d^2} \tag{5.1}$$

where T_d is the time delay applied to the 'STOP' signal generated at the first timing foil of the ToF telescope and L is the flight length between the two timing foils.

The MDE's for I, Au, and Si are 6.3 MeV, 9.8 MeV, and 1.4 MeV respectively for the experimental T_d setting of 160 ns. We cannot, however, set $E_{fin}(Z)$ at these values as it is kinematically possible for an I ion of less than 6.3 MeV to generate a Si recoil with energy higher

than its MDE, and we would risk losing Si recoil data from the simulation. For example, a 6 MeV I ion can generate a Si recoil at an angle of 45° with an energy of 1.8 MeV which is above the MDE of Si and may contribute to the spectrum.

We therefore determine the lowest energy, E_{MDE}, at which the atom can transfer the MDE to a lighter species present. The maximum energy transfer occurs for a 'knock-on' collision (i.e. $\phi = 0$ in Equation 2.2) and the kinematic factor is

$$\Lambda_0(M_1, M_2) = \frac{4M_1M_2}{(M_1 + M_2)^2} \tag{5.2}$$

The energy required for an atom of mass M_1 to generate a MDE recoil of mass M_2 is

$$E_{MDE}(M_1, M_2) = \frac{MDE(M_2)}{\Lambda_0(M_1, M_2)} \tag{5.3}$$

For each atom species, the cut-off energy $E_{fin}(Z)$ is set to the minimum of (i) its own $MDE(Z)$, and (ii) the smallest energy $E_{MDE}(M_Z,M_i)$ at which it can generate a detectable recoil.

The presence of light elements in the sample has the effect of lowering E_{fin} for all ions and therefore increasing the simulation time. We allow the user to specify a parameter, Z_{min}, the atomic number of the lightest element in the sample for which a recoil spectrum is to be generated. The values of $E_{fin}(Z)$ will be set higher and the simulation will run faster. This can expedite the process of matching layer thicknesses based on the heavier recoil spectra. The lighter recoil spectra can be included in subsequent runs to produce a complete simulation.

Table 5.1 compares the simulation times for several choices of ion transport cut-off energy, and compares them with the time savings available by optimising the cutoff for each ion species based on the atoms present in the sample.

By default, E_{fin} is set for each atom species to be equal to the displacement energy, E_d, of the atom in the lattice. Typical values of E_d are 13 eV for Si and 20 eV for Au. The simulation time using

default values of E_{fin} is 718.6 seconds per million incident ions modelled. Raising E_{fin} to 50 keV which is lower than the MDE for all atom species, reduces the simulation time to 48.5 s – a reduction of 93 %. Raising E_{fin} further, to 1.4 MeV equal to the MDE for Si which is the lightest element present in the sample, reduces the simulation time to 25.5 s per 10^6 ions.

Table 5.1 Simulation time comparison for several choices of ion transport cut-off energy E_{fin}. The modelled experiment is 60 MeV I incident at 67.5° upon 75 nm Au on 1 nm Si substrate.

Spectra generated	**Selection of cut-off energy, E_{fin}**	**Simulation time per 10^6 ions (s)**	**Time reduction relative to E_{fin} = 1.4 MeV (%)**
I, Au, Si	Default values: displacement energy, E_d of Si = 13 eV, E_d of Au = 20 eV	718.6	n/a
	E_{fin} set manually to 50 keV (i.e. < MDE for all elements) for all ions and recoils	48.5	n/a
	E_{fin} set manually to 1.4 MeV (= *MDE(Si)*) for all ions and recoils	25.5	-
	E_{fin} calculated at *optimised* values for each element	21.0	18 %
I, Au	E_{fin} set manually to 6.3 MeV (= MDE(I)) for all ions and recoils	16.2	36 %
	Z_{min} set to 79 (Au). E_{fin} calculated at *optimised* values for I and Au	15.0	41 %

Optimising E_{fin} for all elements based on Si being the lightest element present yields a simulation time of just 21.0 s per 10^6 ions. Excluding the Si recoil spectra from the simulation allows a further 29 % time reduction to 15.0 s per 10^6 ions.

Clearly, significant time savings are available through the use of intelligently chosen values of the ion transport cut-off energy. The greatest time savings are achieved by excluding the lowest energy ion transport, with diminishing reductions as E_{fin} is increased further.

5.4 Significant Path Prediction Based on Impact Parameters

The ion paths of interest in the simulation are those which include significant scattering of the incident ion, or the generation of an energetic recoil. Incident ions which penetrate the sample without producing a recoil, and recoiled atoms which do not get detected consume processing time without contributing to the output. If these ion paths can be identified early, processing time can be reduced by abandoning their simulation.

Ions that might generate a detectable scattered or recoiled ion may be predicted by generating in advance, the impact parameters (see Figure 4.1) which will define its path. This list is interrogated for the presence of a small enough impact parameter to cause a scattering event of interest. If not present, the ion is not tracked.

The implementation of this efficiency enhancement is handled differently for incident ions and recoil atoms based on the primary event of interest for each. For incident ions we are most interested in the displacement of energetic recoil atoms. Once a recoil has been generated, we are interested in whether its trajectory is toward the detector or could become so after further scattering.

5.5 Impact Parameter Interrogation for Significant Ions

As shown in section 5.2, the Si substrate does not contribute significantly to the output spectrum of recoiled Au atoms. The sample may therefore be represented by the 75nm Au layer on a thin (e.g. 1 nm) Si layer to represent the layer interface. In this arrangement, most incident ions will traverse

the sample without a significant scattering event. To generate a detectable recoiled or scattered ion of interest, an incident ion will certainly need to have at least one collision in which there is a substantial energy transfer to a target atom. Such heavy impacts are rare events; in the Au layer example, fewer than 2% of ions will have an impact in the Au layer involving an energy transfer of 1 MeV or greater.

To implement this ion tracking efficiency improvement, we need to consider the following :

- How much energy needs to be transferred to cause a recoil of interest?
- What value of the impact parameter, b, provides this energy transfer?
- How many impact parameters need to be considered for each ion?

5.5.1 Determine the Minimum Energy Transfer Threshold

FastTrim was used to report energy and nuclear energy transfer information for 10,000 ions *transmitted* through a 75 nm Au layer with no substrate. Characterising the transmitted ions yields a set of necessary conditions for those ions which are not simply transmitted i.e. have experienced a significant scattering event.

Most 60 MeV I ions penetrate the Au layer, and are transmitted with a mean energy of approximately 56 MeV (Figure 5.3) unless they have had at least one collision with $\Delta E \geq 1$ MeV. More than 99 % of transmitted ions have energy $E \geq 53$ MeV, and none of these have had a 1 MeV energy transfer. We conclude that an energy transfer of 1 MeV is a suitable minimum requirement to have a collision of interest, and choose this as the energy transfer threshold for impact parameter interrogation. This can be generalised to the MDE of the lightest sample species present in compound or multi-layered samples.

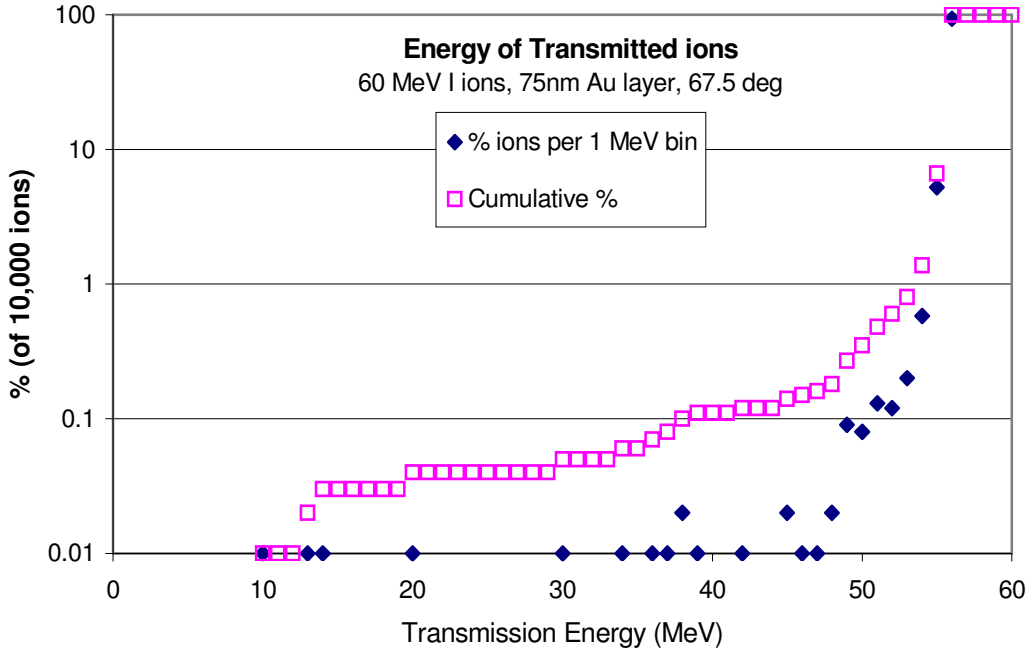

Figure 5.3 Energy distribution of 60 MeV I ions transmitted through 75 nm Au layer

5.5.2 Critical Impact Parameter

The largest significant impact parameter that can cause an energy transfer of 1 MeV or greater to a target atom must be determined.

For each binary collision, the impact parameter, b, is determined by a random number R generated in the interval (0,1]. The impact parameter is weighted with an r^2 probability distribution in the range (0, b_{max}]

$$b = b_{\max} * \sqrt{R} \tag{5.4}$$

where b_{max} is the largest allowable impact parameter for the current layer, and is made smaller than half the interatomic spacing to ensure the minimum energy transfer, T_{min}, in each collision (refer to section 4.1.8).

The amount of energy transferred for a given impact parameter increases with decreasing incident energy for energies above the local maximum of the Energy Transfer vs Incident Energy curve (see Figure 5.4). This means that larger impact parameters become more significant as ion energy decreases, so the critical impact parameter must be determined for the lowest energy that an ion will have in the Au layer i.e. the energy that the ions will have at the back of the layer in the absence of a large interaction (53 MeV in this example). The critical impact parameter, b_c, which causes a 1 MeV energy transfer for 53 MeV I ions in Au is b_c = 0.63 fm. Impact parameters smaller than or equal to b_c = 0.63 fm occur with a probability of 0.000243 equal to the random number that gives rise to it in Equation 5.4 (see Figure 5.5).

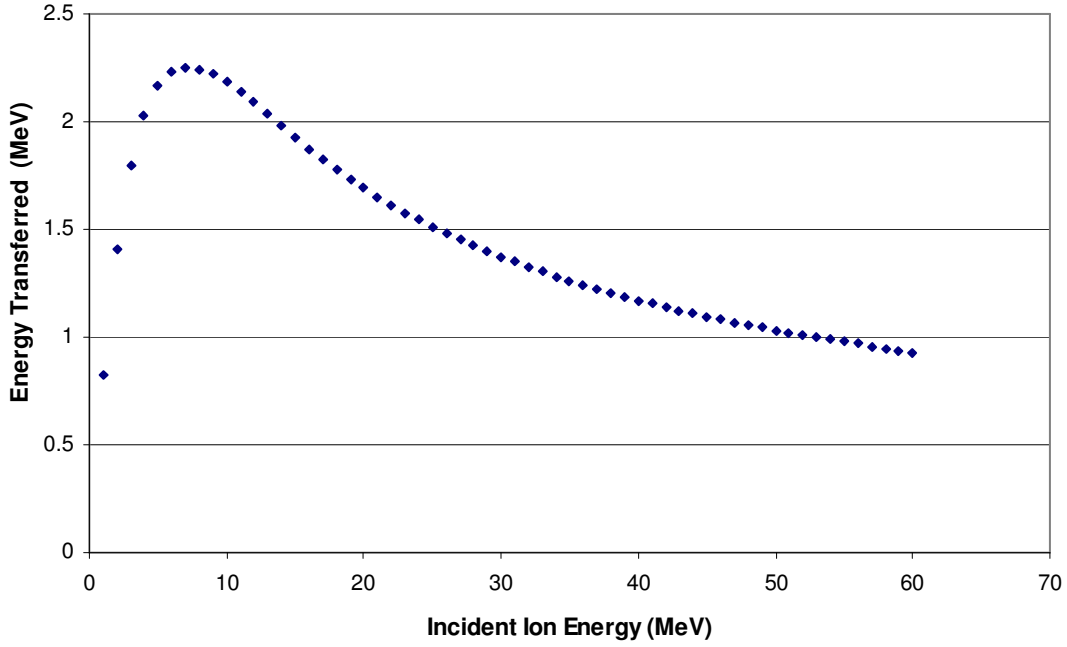

Figure 5.4 Energy transfer to Au target atom for incident I ions at 0-60 MeV for an impact parameter b = 0.63 fm (R = 0.000243)

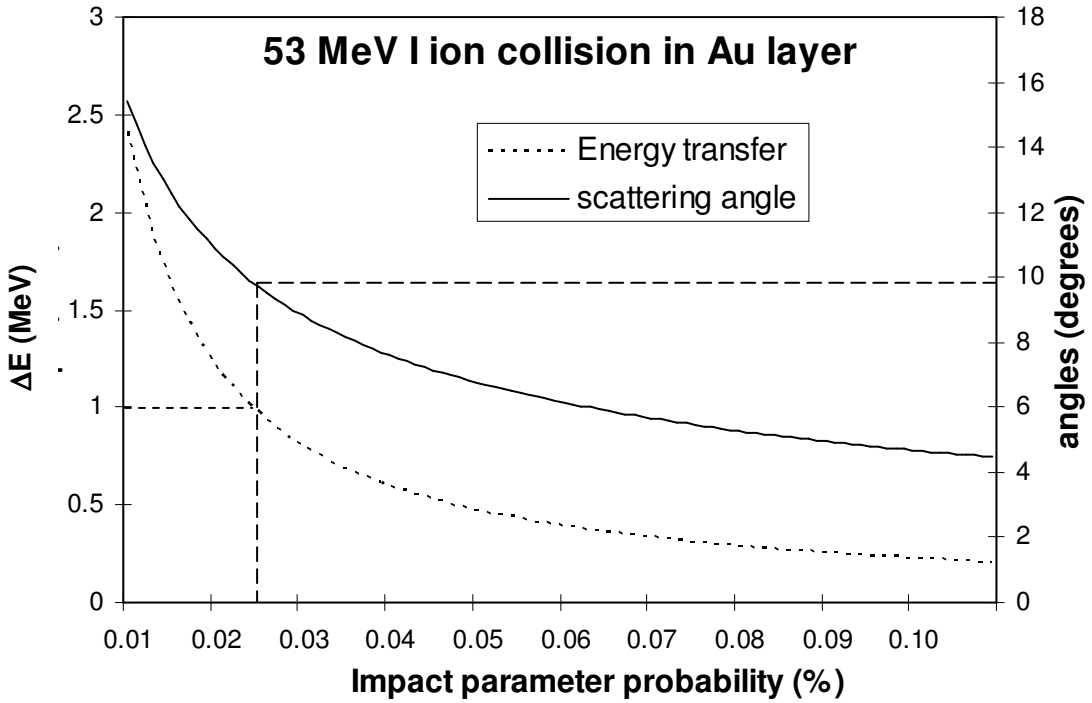

Figure 5.5 Energy transfer and Scattering angle as a function of impact parameter probability for 53 MeV Iodine ion collisions in Au layer. Collisions of greater than 1 MeV energy transfer, and scattering angle larger than 10º occur with a probability of 0.0243 %

The nuclear scattering Energy Transfer curve features a local maximum analogous to the Bragg Peak of the electronic Stopping Power curve. As long as the layer or sample is sufficiently thin, un-scattered ions will reach the back of the layer with energy greater than E_{max}, the energy at which the Energy Transfer vs Incident Energy graph has its local maximum. In these cases the critical impact parameter b_c, is set using the energy at the back of the layer. For thick layers, the energy at the layer back may be less than E_{max} and therefore not lead to the largest significant impact parameter. In this case, we determine the impact parameter using E_{max}.

The energy transferred in a single collision having impact parameter b, is given by

$$\Delta E = \frac{\Lambda E}{1 + (1 + b(1+b))(2\varepsilon b)^2} \tag{5.5}$$

for the screened Coulomb potential (i.e. Rutherford scattering with electronic screening modification (see 2.2.3), where Λ is the kinematic factor from equation 2.2 and $\varepsilon = EF$ is a reduced dimensionless energy. F is a function of the masses and charges of the two particles only.

$$F = \frac{M_2}{Z_1 Z_2 (M_1 + M_2) \times 14.41} \times \frac{0.8854 \times 0.5292}{Z_1^{0.23} + Z_2^{0.23}} \tag{5.6}$$

Equation 5.5 may be expressed as

$$\Delta E = \frac{\Lambda E}{1 + cE^2} \tag{5.7}$$

which has a turning point at

$$E_{\max} = \frac{1}{\sqrt{c}} \tag{5.8}$$

where

$$c = 4b^2 (1 + b + b^2) F^2 \tag{5.9}$$

In practice, the critical impact parameter search is implemented, at the programming level, using the random number variable, R, to avoid time spent calculating b for every random number generated. The turning point is not readily located algebraically as the correspondence between R and b is scaled against b_{max} (equation 5.4) as the energy E changes, to ensure the T_{min} condition is met (see 4.1.8 for details). The critical impact parameter is determined using a binary search algorithm incorporating a gradient test to locate the local maximum. For 53 MeV I, the search takes 13 iterations to calculate b_c = 0.00635 (R=0.00243) for the Au layer and 16 iterations for b_c = 0.00303 (R=0.0000831) for the 1 nm Si layer. The time taken is negligible.

Having determined the critical impact parameter, b_c, the impact parameters that will define an ion's path are generated in advance, interrogated for the presence of one smaller than b_c, and the ion only tracked if one is present.

5.5.3 Number of Impact Parameters to be Interrogated

Most ions will traverse the sample in approximately a mean number of free flight path jumps, dependent upon the incident energy, the ion species, and target atom species present. Each jump is followed by a collision. This defines the number of impact parameters that should be generated and interrogated in advance. Due to the stochastic nature of the ion paths, this number should be increased by an amount sufficiently large to account for some ions having a larger number of interactions while still not undergoing an event of interest.

Fastrim was modified to report collision and energy information for ions transmitted through the 75nm Au layer. The number of collisions was reported for each transmitted ion, and the impact parameter and energy transfer for its largest collision. The average number of free flight path jumps (and collisions) was 59 (Figure 5.6). 99.8% of transmitted ions had fewer than 90 collisions. Any ion which had more than 90 collisions also had a scattering event in which more than 1 MeV was transferred. We conclude that any ion which has not had a large impact within its first 90 scattering events will pass through the sample and not be of interest. We generalise this to 50 % higher than the mean number of free flight path jumps taken by the ions to traverse the sample.

The impact parameter testing is disabled if the ion energy, sample thickness, and composition are such that the number of free flight paths required for an ion to traverse the sample is more than $\Pr(b \leq b_c)^{-1}$, as such an impact parameter will probably occur. The additional processing time spent interrogating the impact parameter list will rarely result in time savings from discarded ions.

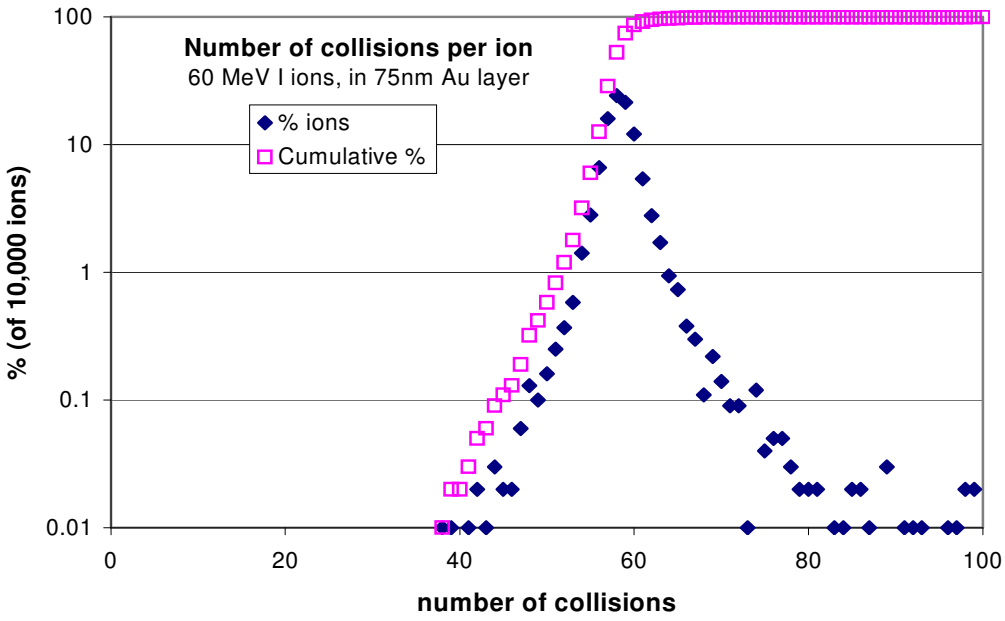

Figure 5.6 Number of collisions and free flight paths modelled per layer traversal for 60 MeV I ions transmitted through 75 nm Au layer.

5.5.4 Results

In the 75 nm Au layer example, fewer than 2% of incident ion paths need to be followed, and processing time was reduced by a factor of 13. The time reduction factor is less than 50 because ion paths which include one or more large angle scattering events require more processing than simple transiting ions; an energetic recoil is generated and needs to be followed, the scattered ion's path through the sample may be longer, and its lower energy will result in more scattering events modelled per unit path length.

In much thicker samples, the number of impact parameters to be interrogated is larger and therefore the probability of ions being discarded is reduced. However, even in the relatively thick samples studied in this work the efficiency improvements are significant. For both the 326 nm Ta_2O_5 sample analysed with 97.5 MeV I ions, and the Ag double layer sample (166 nm Ag / 50 nm a-CH / 165 nm Ag / Si substrate) analysed with 82.5 MeV I, over 95 % of incident ions could be discarded.

5.6 Impact Parameter Interrogation for Significant Recoils

A similar treatment to that used for incident ions may be applied to those recoil atoms generated in a direction away from the sample surface. Clearly a recoil that is travelling deeper into the sample cannot reach the detector unless it experiences a significant change of direction in one or more scattering events.

Note that recoils are treated differently to incident ions. The event of interest for an ion is the production of a recoil i.e. a substantial energy transfer to a target atom. Once a recoil atom is generated, we are interested in its detection, therefore for a recoil travelling deeper into the sample, the event of interest is a substantial direction change. Impact parameters are interrogated on the basis of scattering angle.

Impact parameters are generated for the present layer only. If no small impact parameters are present, then the recoil will either (i) reach the next layer boundary (which may be transmission behind the sample), or (ii) stop in the sample. In the former case, the recoil is then jumped to the next layer boundary via an extended free flight path, and the next layer dealt with.

5.6.1 Minimum Direction Change Threshold

Recoils travelling deeper into the sample are easily identified by a simple test for a positive direction cosine relative to the depth axis of the sample coordinate system. For these recoils, a direction change of at least 22.5º is required for the recoil to reach the surface and have a possibility of being detected. [Note: here we consider the usual symmetrical orientation of the sample, and the experimental configuration of the HIERDA instrument at ANSTO's ANTARES

accelerator facility (refer to Chapter 3) which has a beamline-detector angle of θ_{det} = 45º. Other experimental configurations can be easily handled, as can asymmetric incident and exit angles which are sometimes used to enhance recoil yield.]

Allowing for plural scattering, this direction change may be achieved via two or more scattering events. We consider some fraction of the required direction change to be the minimum deflection needed from at least one scatter. The occurrence of two similar sized direction changes is frequent enough to produce an artefact in the HIERDA spectrum: the high energy "knee" (see section 4.3). We allow for three events of approximately one sixth of the detection angle, and set the critical scattering angle for recoils, θ_c, to

$$\theta_c = \frac{\theta_{\text{det}}}{6} = \frac{22.5}{3} = 7.5° \tag{5.10}$$

5.6.2 Critical Impact Parameter

Consider a recoil atom moving through a sample layer which may have more than one element present (i.e. a compound layer). We must test for the presence of impact parameters small enough to produce direction changes of 7.5º or more. As for the energy transfer from incident ions in section 5.5.2, the scattering angle for this recoiling atom will be greater at lower energies and for higher atomic number Z_2 of the target atom from which it is deflected. So the largest significant impact parameter is determined by considering collisions with the heaviest target species present at the lowest energy that the recoil could have in the layer; that is, the transport cut-off energy E_{fin}.

Table 5.2 gives impact parameters for Au, V, and Si recoiling atoms being further deflected by 7.5º or more, at a range of energies from 20 MeV down to their cut-off energies E_{fin} (as determined by the presence of Si in a typical HIERDA measurement).

We can see that across this range of energies and mass ratios, deflections of 7.5 degrees or greater can be achieved by impact parameters in the order of 1 to 10 fm. These are relatively large fractions of the maximum possible impact parameters of 145 fm, 137 fm, and 153 fm for Au, V, and Si respectively, as determined by the inter-atomic separations and the T_{min} condition (section 4.1.8). Significantly, for lower energy atoms moving in a heavy matrix, the relevant impact parameters are of a similar size, regardless of the species of the moving atom, occuring with a probability in the order of 0.1 %. Allowing for the modelled free flight path length being equal to the interatomic separation, we should then *expect* such deflections to occur approximately every 1000 atom spacings i.e. about 0.25 nm, for low energy heavy recoils. In lighter substrates such as Si, such scattering is only 10 times less frequent. For heavy species, recoil energies as high as 20 MeV only reduce the scattering frequency by an order of magnitude, although this is more like two orders of magnitude for lighter species.

The glancing geometry of HIERDA configuration, designed to enhance stopping by increasing the path length through the sample, means that a significant percentage of paths of all but near surface region recoils will be plurally scattered. As we shall see in Chapter 6, this high frequency of substantial deflections will have significant ramifications for the influence of plurally scattered recoils on the output spectra.

Table 5.2 Critical Impact Parameters for 7.5º deflection of recoiling target atoms subsequently scattered by other atoms of the sample. Also shown are the energy transferred and the probability of an interaction of at least this size.

Incident species	Target species		Incident Energy (MeV)			
			20	**10**	**5**	E_{fin}
Au		b_c *(fm)*	2.89	4.99	8.07	10.65
E_{fin}=3.2 MeV	Au	ΔE	341 keV	170 keV	85 keV	54 keV
		$Pr(b \leq b_c)$	4.00×10^{-4}	1.19×10^{-3}	3.10×10^{-3}	5.40×10^{-3}
		b_c *(fm)*	0.89	1.70	3.05	4.30
	V	ΔE	1.4 MeV	686 keV	343 keV	219 keV
		$Pr(b \leq b_c)$	4.22×10^{-5}	1.54×10^{-4}	4.98×10^{-4}	9.93×10^{-4}
		b_c *(fm)*	0.42	0.33	0.62	0.90
	Si	ΔE	6.6 MeV	3.3 MeV	1.7 MeV	504 keV
		$Pr(b \leq b_c)$	1.35×10^{-6}	4.66×10^{-6}	1.62×10^{-5}	1.93×10^{-4}
V		b_c *(fm)*	0.95	1.81	3.31	8.30
E_{fin}=1.53 MeV	Au	ΔE	88 keV	44 keV	22 keV	7 keV
		$Pr(b \leq b_c)$	4.29×10^{-5}	1.56×10^{-4}	5.23×10^{-4}	3.28×10^{-3}
		b_c *(fm)*	0.29	0.56	1.10	3.24
	V	ΔE	341 keV	170 keV	85 keV	26 keV
		$Pr(b \leq b_c)$	4.38×10^{-6}	1.71×10^{-5}	6.50×10^{-5}	5.62×10^{-4}
		b_c *(fm)*	0.17	0.34	0.68	2.08
	Si	ΔE	620 keV	310 keV	155 keV	47 keV
		$Pr(b \leq b_c)$	1.27×10^{-6}	5.03×10^{-6}	1.95×10^{-5}	1.84×10^{-4}
Si		b_c *(fm)*	0.59	1.15	2.17	6.31
E_{fin}=1.4 MeV	Au	ΔE	49 keV	24 keV	12 keV	3 keV
		$Pr(b \leq b_c)$	1.66×10^{-5}	6.26×10^{-5}	2.24×10^{-4}	1.89×10^{-3}
		b_c *(fm)*	0.18	0.35	0.69	2.28
	V	ΔE	188 keV	94 keV	47 keV	13 keV
		$Pr(b \leq b_c)$	1.65×10^{-6}	6.50×10^{-6}	2.53×10^{-5}	2.79×10^{-4}
		b_c *(fm)*	0.11	0.21	0.42	1.44
	Si	ΔE	341 keV	170 keV	85 keV	24 keV
		$Pr(b \leq b_c)$	4.85×10^{-7}	1.92×10^{-6}	7.57×10^{-6}	8.87×10^{-5}

5.6.3 Number of Impact Parameters to Interrogate

In the absence of a suitable scattering event, the energetic recoil will either (i) continue to the next layer boundary, or (ii) stop in the current layer of the sample. The number of impact parameters to be generated is equal to the number of free flight paths to be modelled before one of the above occurs. Since the modelled free flight path length is always made equal to the interatomic spacing for recoils, this is equivalent to comparing the recoil's *range* and the path length to the boundary, and dividing the lesser by the interatomic distance. The mean projected range of a recoil with energy E_r is approximately

$$R = \int_0^{E_r} \frac{dE}{S_T(E)} \tag{5.11}$$

where $S_T(E_r)$ denotes the *total* stopping power allowing for both electronic and nuclear energy transfer i.e. $S_T(E_r) = S_e(E_r) + S_n(E_r)$. Equation 5.11 is an approximation as the integral actually gives the mean *path length* which needs to be corrected for directional deviations to yield the forward projected range.

In the programming implementation the relevant range is the 'range to cut-off energy', R_{fin},

$$R_{fin} = \int_{E_{fin}}^{E_r} \frac{dE}{S_T(E)} = \int_0^{E_r} \frac{dE}{S_T(E)} - \int_0^{E_{fin}} \frac{dE}{S_T(E)} \tag{5.12}$$

since the transport would not be followed beyond this. For the purposes of interrogating the impact parameter list, it is sufficient to acknowledge that there may be a larger number of intervals modelled before the boundary or E_{fin} is reached.

To implement a fast range estimation, a lookup table is generated for range as a function of energy for each atom species in each layer of the sample. The range is calculated for a logarithmically separated list of energies identical to that used for stopping power interpolation. The integral is approximated numerically using Simpson's Rule for quadratically interpolating the stopping power data. The appropriate stopping power is the sum of the electronic and nuclear stopping rather than the exclusively electronic stopping normally applied over the free flight intervals.

The range table is then scaled to the number of free flight paths and collisions to be modelled before reaching the cut-off energy, by applying equation 5.12 and dividing by the interatomic separation. This interval-scaled range can then be compared to the distance to the next layer boundary. The lesser of the two defines the number of impact parameters to be searched.

Recoils generated in a direction close to parallel to the sample surface may have very long paths within their current layer. The high potential for time saving over a large number of steps is offset by a higher probability of occurrence of an impact parameter meeting the criteria of 5.6.2 if there are a large number of them to be generated. As for the incident ion case, if the number of parameters to be tested is greater the reciprocal of the corresponding probability, the recoil is followed without prior interrogation of its parameter list.

5.6.4 Jump to Layer Boundary

Since layer compositions may differ significantly, multi-layered samples are dealt with one layer at a time. The presence or absence of heavy elements will have a large influence on the efficiency gains available in each layer. The relevant impact parameters may vary by an order of magnitude, and their probability of occurrence by two orders or more (refer to Table 5.2). Large angular deflections are much less likely in low Z layers and there is greater scope for acceleration of recoils through these layers.

Consequently, the impact parameter list is only generated for the remainder of the path through the current layer – either to the layer boundary or to the energy cut-off point within the layer if this will occur first. In the absence of a small enough impact parameter, a recoil of the latter type will be abandoned immediately, while the former are jumped to the next layer boundary via an extended free flight path interval. If this jump to the next layer boundary would result in the atom being transmitted, it is abandoned instead.

5.6.5 Results

The reduction in processing time available by impact parameter testing for recoils is relatively small in distinct contrast to that achieved by applying the same method to incident ions. The simulation time for the 75 nm Au layer sample was reduced by only 6.9 %. An identical simulation was run for three other metals showing that the gains are somewhat better for lighter target materials. In each case the sample modelled was a 75 nm thick mono-elemental layer on 10 nm of Si, and the cut-off energy was dictated by the MDE of the principle target layer. Table 5.2 summarises the timing results and the number of recoils in each simulation eligible for treatment by this method.

The small time reductions of between 6.9 % and 12.9 % indicate that the overhead cost in predicting these events is comparable to the time taken to follow these recoils explicitly, and that substantial direction changes are relatively frequent events, particularly for heavy ions. In the Au layer simulation, almost half of the Au recoils tested will be subject to a scatter of greater than or equal to 7.5º.

Of all recoils displaced (with energy higher than the cut-off value in these simulations), more than half were generated with an initial direction deeper into the sample and therefore eligible for this treatment. The slightly increasing fractions for heavier targets reflect the higher energy of forward scattering combined with the higher cut-off energy of heavy recoils. A small percentage of recoils are abandoned early due to the absence of a re-direction before stopping in the layer. A significant fraction – 54 % of Au recoils and up to 85 % for Al recoils – would have been transmitted through the layer without a 7.5º scatter and not contributed to the output spectrum.

The paths of many recoils, particularly heavy ions, are likely to feature many scattering events with significant direction changes, even for the thin samples usually analysed by HIERDA which are typically a few tens or hundreds of nanometres thick.

Table 5.3 Time reductions achieved by impact parameter testing of recoils. Times are given in seconds per 10^6 incident ions modelled. The number of recoils that the test was applied to is also shown. See text for a detailed description.

	Al	V	Ag	Au
No Recoil Testing (s/10^6 ions)	7.0	10.4	11.8	16.7
With Recoil Testing (s/10^6 ions)	6.1	9.4	10.9	15.5
Time Reduction (%)	12.9 %	9.1 %	7.6 %	6.9 %
Recoils generated deeper into sample (%)	55	56	58	59
Recoils stopped in layer without 7.5° scatter (%)	9	11	7	6
Recoils transmitted through layer without 7.5° scatter (%)	85	79	68	54

It can also be seen from Table 5.2 that these relatively common large deflections can be achieved at very little cost in energy when the sample atom is equal in mass or heavier than the moving recoil. Thus plural scattering may have a large influence on the number of recoils reaching the detector and their path lengths, without necessarily being responsible for their removal from the experiment in the process.

5.7 Conclusion

The efficiency improvements described in Chapter 5 have enabled simulation time for our Au layer test case to be reduced from around 53 days at the beginning of this work, to approximately 4 hours. The time savings achieved as a result of the optimisations described in this chapter are to an extent beam and sample dependent, as are the simulation times themselves. Thick samples and low beam energy yield longer simulation times, but consequentially have the most to gain from efficiency enhancements. The simple Au layer sample is simulated almost three orders of magnitude faster using these techniques. The time reduction factors for the thick Ta_2O_5 sample and the double layered Ag sample are 490 and 430 respectively.

Simulations require about 10^9-10^{10} incident ions to be modelled to produce output spectra with sufficient statistics to enable spectral comparisons with experimental data. With these efficiency gains, it is feasible to use this form of Monte Carlo simulation to study Plural Scattering in HIERDA. The relative gains achieved via a detailed analysis of ion and recoil paths highlight the importance of understanding the influence of plural scattering on spectra. The impact of these processes on the simulation time is representative of their frequency within the experimental procedure.

The identification and characterisation of Plural Scattering is necessary before the contribution to the output spectra can be meaningfully quantified. In Chapter 6, we consider a suitable definition of *plural scattering* for ions and recoils, and decompose their contribution to output spectra.

Chapter 6

Multiple and Plural Scattering

The quantitative evaluation of output spectra from HIERDA experiments is dependent on a clear understanding of the contribution from plurally scattered ions. Monte Carlo simulation offers a unique opportunity to separate counts in the spectrum based upon their scattering history within the sample, as the complete history of each ion reaching the detector has been modelled explicitly.

6.1 Characterisation of Scattering

The large number of scattering events that each ion undertakes makes the handling of the full record of scattering histories unwieldy. Even with all optimisation techniques employed, a simulation of 10^9 incident particles will involve simulating around 10^{10} scattering events and in the order of hundreds of modelled interactions per detected ion or recoil. To keep the data burden manageable, a record is kept of the magnitude of the most significant direction changes in the scattering history of all ions reaching the detector. This information is used to characterise the paths of plurally scattered counts contributing to the output spectra.

Recorded with the species, direction, and energy of each detected ion is a list of the 10 largest direction changes in its scattering history. At each interaction, the scattering angle is compared with the list prior to that point, and inserted where appropriate. The history of a recoiled target atom incorporates the incident ion's history prior to generation of the recoil (see Figure 2.9).

Figure 6.1 shows a frequency distribution of the largest and 2nd, 3rd, 4th and 10th largest direction change for each scattered I ion and recoiled Au atom reaching the virtual detector.

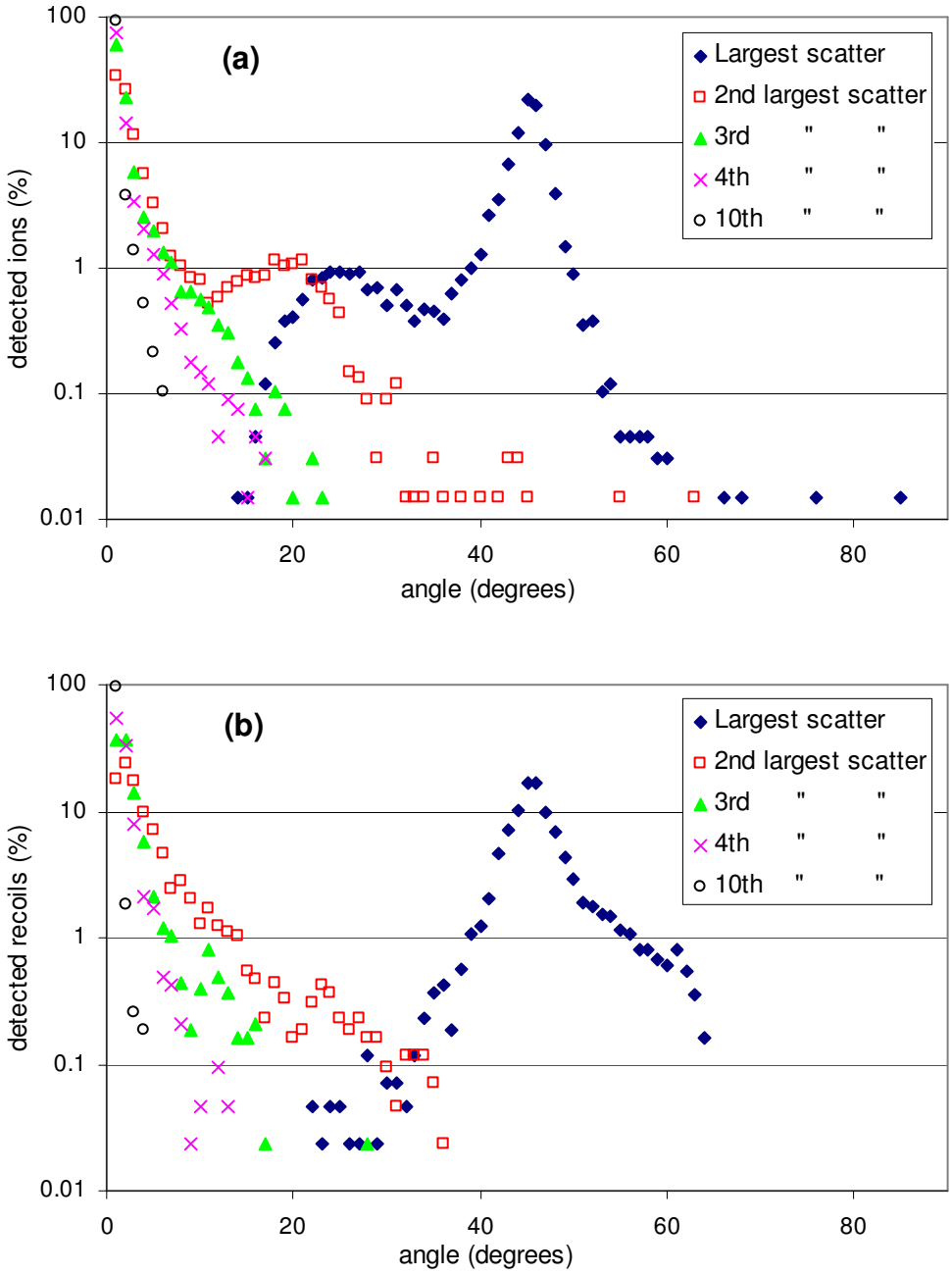

Figure 6.1 Angular distribution of the largest and 2nd, 3rd, 4th, and 10th largest scattering deflections in the paths of (a) scattered 60 MeV I ions and (b) recoiled Au atoms.

The distribution of largest deflections of Iodine ions (Figure 6.1 (a)) shows the expected single scattering distribution around 45˚, equivalent to the experimental detection angle relative to the analysing beam, broadened by the small angular contribution from multiple scattering. This shows that many ions reaching the detector do so after a deflection of a few degrees greater or less than 45˚ and that the remainder of the direction change is provided by small angular deflections. Also present is the distribution below 40˚ and the long tail beyond 50˚ corresponding to the plurally scattered counts. It is interesting to note that there are even a few counts having primary scatters larger than 55˚, and requiring a corresponding secondary scatter of 10˚ or more, reaching the detector with sufficient energy to be measured.

The distribution of second largest deflections exhibits a long tail extending beyond 60˚ and a local maximum near 20˚. This local maximum together with the corresponding feature in the largest scatter data, describes the double scatters – those having two nearly equal deflections to reach the detector. The product of kinematic factors for these two events is greater than that for a single 45˚ scatter (see Section 2.6.2), and the ions are detected with an energy greater than that from a single scatter occurring in the surface layer. This gives rise to the characteristic high energy 'knee' on the surface edge of the HIERDA spectrum. The separation of these two local maxima is due to there being a pair of events of similar magnitude, the larger of which is counted in the first distribution.

Figure 6.1 (b) shows similar distributions for the recoiled Au data. The double scattering is not as well defined and the large angle tailing does not extend beyond 64˚, although the region above 51˚ is an order of magnitude greater than for detected Iodine ions. i.e the single scattering peak at 45˚ is skewed towards larger angles.

The third largest and fourth largest distributions show the presence of counts having had 3 or 4 events greater than 10˚-20˚. The tenth largest distribution shows the existence of detected ions and recoils with up to 10 events greater than a few degrees. Approximately 6 % of detected ions and

2 % of recoils had 10 deflections greater than 1˚. It is clear that a significant percentage of scattering paths are complicated by multiple events of significant magnitude.

6.2 A definition of Plural Scattering

The separation of the plurally scattered component of the spectrum requires the choice of a threshold value of the second largest deflection angle, beyond which the ion will be deemed plurally scattered. The distinction is somewhat arbitrary, and constitutes the differentiation between large angle plural and small angle multiple scattering. The small angle end of the second largest deflection data corresponds to those counts whose largest direction change was near 45˚. The first channel represents counts that did not have a secondary scatter greater than 1˚ and may be considered 'singly scattered'. The lower end of this ramp features counts with a secondary event of 10˚ or greater and these would be appropriately considered 'plurally scattered'. The distinction clearly lies somewhere between. The half-height of this edge is at approximately 3˚, and this is the condition chosen to denote plural scattering.

6.3 Plural Scattering contribution to spectra

Figure 6.2 shows the simulated output spectra with separated contributions from ions that have had n=1, 2, …, 5 scatters greater than 3˚. It can be seen that the high energy 'knee' feature on the leading edge of the spectrum, and the low energy tailing, are due entirely to plural scattering. The single scattered data subsets, i.e. n=1, show the shape of the spectra that would be generated by a conventional analytical 'slab' analysis technique with only a multiple scattering correction applied. The high energy knee and the plural scatter tailing would not be predicted, making the interpretation of the output difficult and in some cases practically impossible. Attempting to account for the low energy tailing is likely to lead the experimenter to erroneously deduce the presence of Au deep into the substrate.

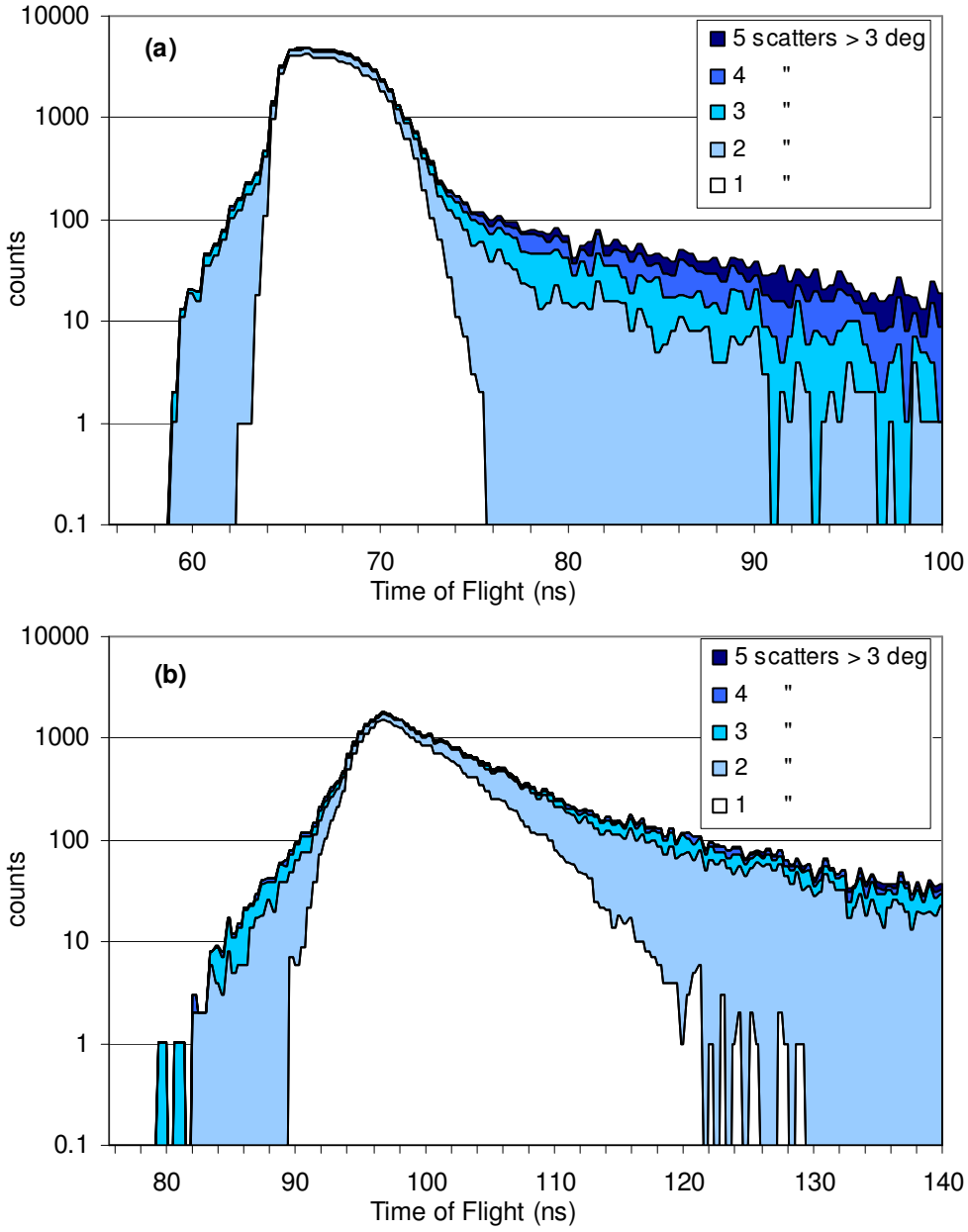

Figure 6.2 Simulated spectra showing contributions to spectral shape from ions having 1, 2, …, 5 scattering events for (a) scattered 60 MeV I ions and (b) recoiled Au atoms.

Low energy tailing is a feature consistent with interfacial diffusion between layers. Mixing at layer interfaces during deposition or annealing is a phenomenon of interest to materials scientists, and is likely to be one of the conclusions sought from the HIERDA measurement. The sample description simulated is a mono-elemental Au layer on a Si substrate with a discrete interface between the two. The MC simulation shows that such tailing will be present in the measured spectra even in the

absence of layer mixing. Thus, incorrect interpretation of the measurement data may occur when using any simulation which does not take plural scattering into account. The high energy knee at the sample surface could not be reproduced at all, making accurate spectrum matching impossible.

There is also a plural scattering contribution to the yield in the main body of the spectrum which is not easily seen due to the log scale used in Figure 6.2. The same data is re-ordered in Figure 6.3 to show this contribution and the Time of Flight distributions of the plurally scattered ions. The spectral shape can be seen in secondary and tertiary scattered ions (Figure 6.3 (a)), and persists right down to the 5^{th} degree plural scatters for recoils (Figure 6.3 (b)). The fact that these distributions appear to be a function of the sample structure perhaps offers some hope for their eventual analytical representation.

Analytical simulations are also unlikely to correctly predict the total yield in the spectrum if plural scattering is not accounted for. The full energy peak region in each of the spectra of Figure 6.3 shows a substantial plural scattering contribution. In the peak channels of the recoiled Au spectrum, which represents the surface region of the sample, 12 % of the counts are plurally scattered. This is the region of the spectrum where the plural scattering contribution is at its *lowest*.

This has implications for the stoichiometric interpretation in the case of compound materials, as the plural scattering cross sections are a function of atomic mass and therefore the relative contributions from plural scattering will not be uniform for heavy and light ions. Figure 6.4 shows the simulation data for the 326 nm Ta_2O_5 sample with the plural scattering breakdown. It can be seen that the relative contributions from plural scattering are different between the ions and recoils of different atomic mass. The spectrum of scattered ions, being the heavier particles in this case, is more heavily influenced by the plural scattering contribution than are the recoil spectra. The overall shape of the spectrum is strongly dependent upon both the single and plural scatter components. The traditional trapezoidal shape of the spectrum is formed by the plural scattered counts. In the absence of these, the spectral shape would degenerate to a more triangular profile. Plural scattering

is a likely occurrence for ions penetrating beyond the near-surface region, and the fall off in intensity with depth merges almost indistinguishably with the low energy tailing at the back of the layer.

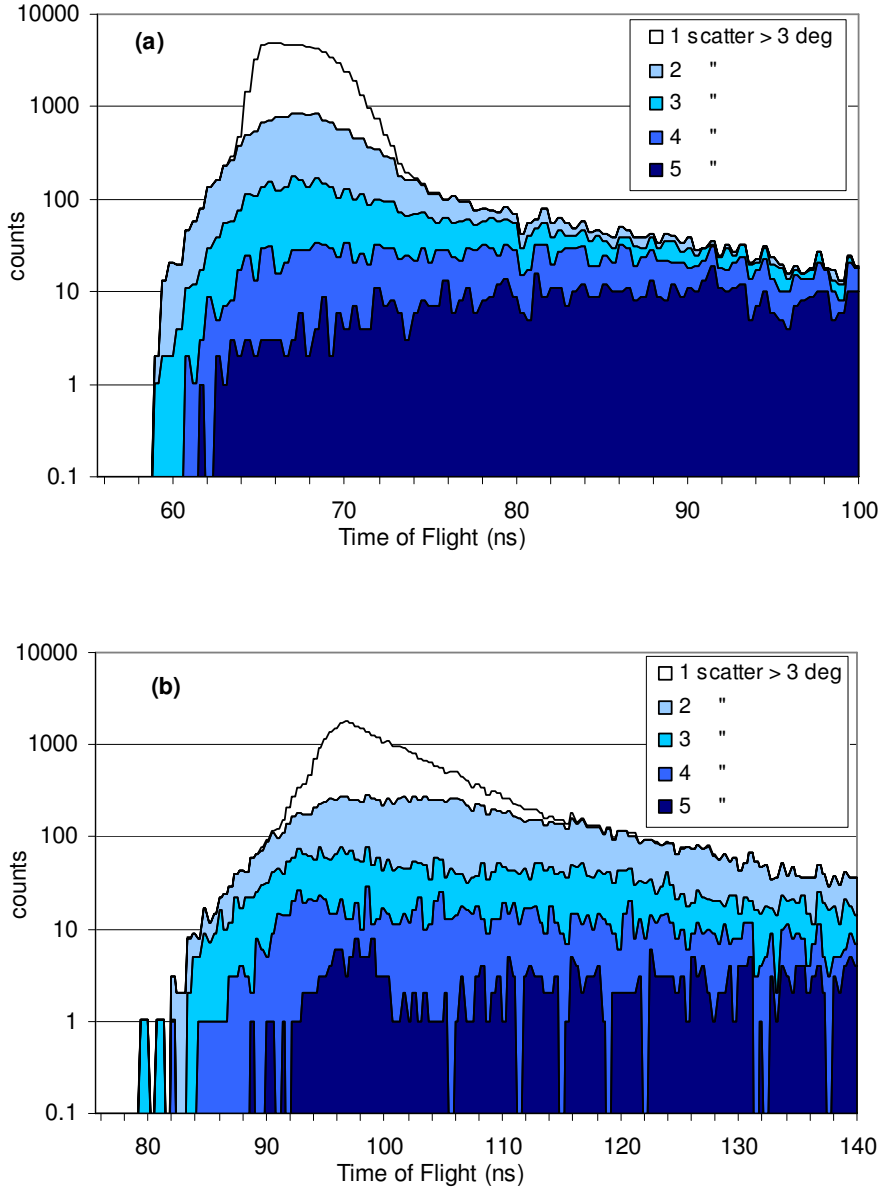

Figure 6.3 Simulated spectra showing ToF distributions of ions having 1, 2, …, 5 scattering events for (a) scattered 60 MeV I ions and (b) recoiled Au atoms.

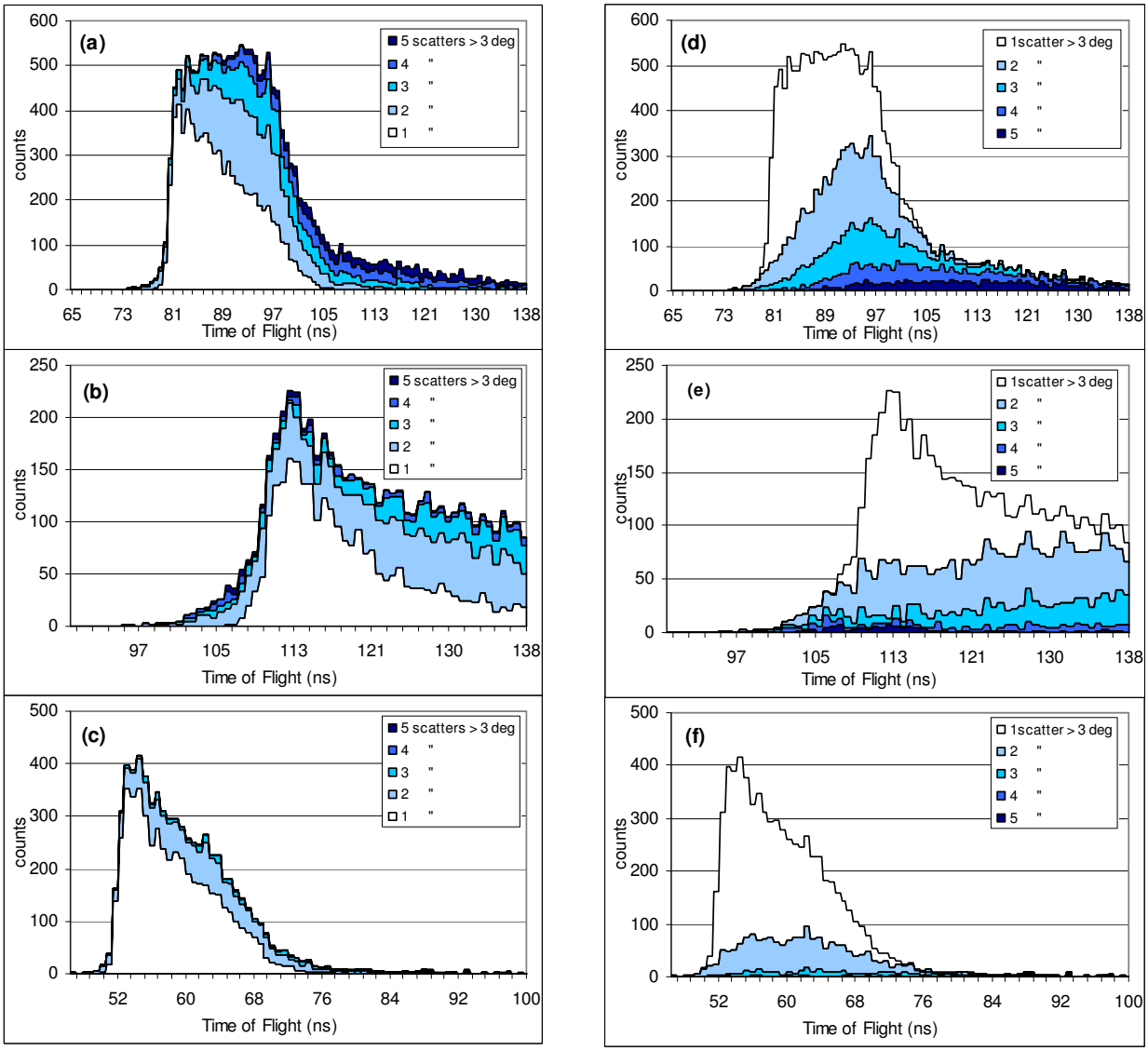

Figure 6.4 Simulated spectra showing contributions to spectral shape and ToF distributions from ions having 1, 2, …, 5 scattering events for (a,d) scattered 40 MeV I ions, (b,e) recoiled Ta, and (c,f) recoiled O atoms.

An analytical simulation apparently correctly predicting the trapezoidal shape of the spectrum as is usually seen in Backscattering and Recoil Spectrometry, would do so only by neglecting two types of events: some ions initially scattered toward the detector in a single scatter event will subsequently be scattered away from the detector; and some ions initially directed away from the solid angle of the detector may be scattered into it by subsequent events. The probability for plural scattering increases at lower energies, so these events are more prevalent for ions from deeper in the sample which normally contribute to the lower energy (longer flight times) region of the peak. Geometrical asymmetry dictates that ignoring these two effects will not balance out. The solid angle available for the latter is greater than for the former, and asymmetry of both the kinematic factor and the scattering yield with respect to the detection angle make the net effect even more complex. In general, the spectral shape will not be correctly predicted by the analytical simulation.

The situation is less severe for the recoiled Ta and O spectra. In these, the single scatter component exhibits a similar shape to the overall combined spectrum. In the case of the recoiled Ta spectrum, the plural scatter contributions are almost uniform across the peak, increasing only slightly with decreasing energy (longer flight times). In the recoiled O spectrum, the double scattered counts, and to a lesser extent the triple scatters, show some correlation with peak shape. The higher order scatters are almost uniform but of negligible magnitude within the peak, although they form the low energy tail.

Figure 6.5 shows the plural scattering breakdown for detected particles in the Bromine-Vanadium simulation (described in section 4.3.2) where the detection angle of 45˚ is beyond the critical angle for scattering of Br from V (θ_c=39.6˚). It can be seen that almost all of the scattered Br spectrum is the result of plural scattering consisting of 2 or more events. Interestingly, there is a component of the spectrum which may be regarded as singly scattered i.e. those ions which have been detected after having no more than 1 scatter greater than 3˚. This reflects the fact that the critical scattering angle is only 5.4˚ less than the detection angle. Thus it is possible for ions to achieve this additional direction change with several additional scatters smaller than 3˚. These ions would reasonably be

regarded as single scatter ions that have been influenced by small angle multiple scattering. However their presence would not be predicted using slab analysis, even by an analytical simulation with a multiple scattering correction included.

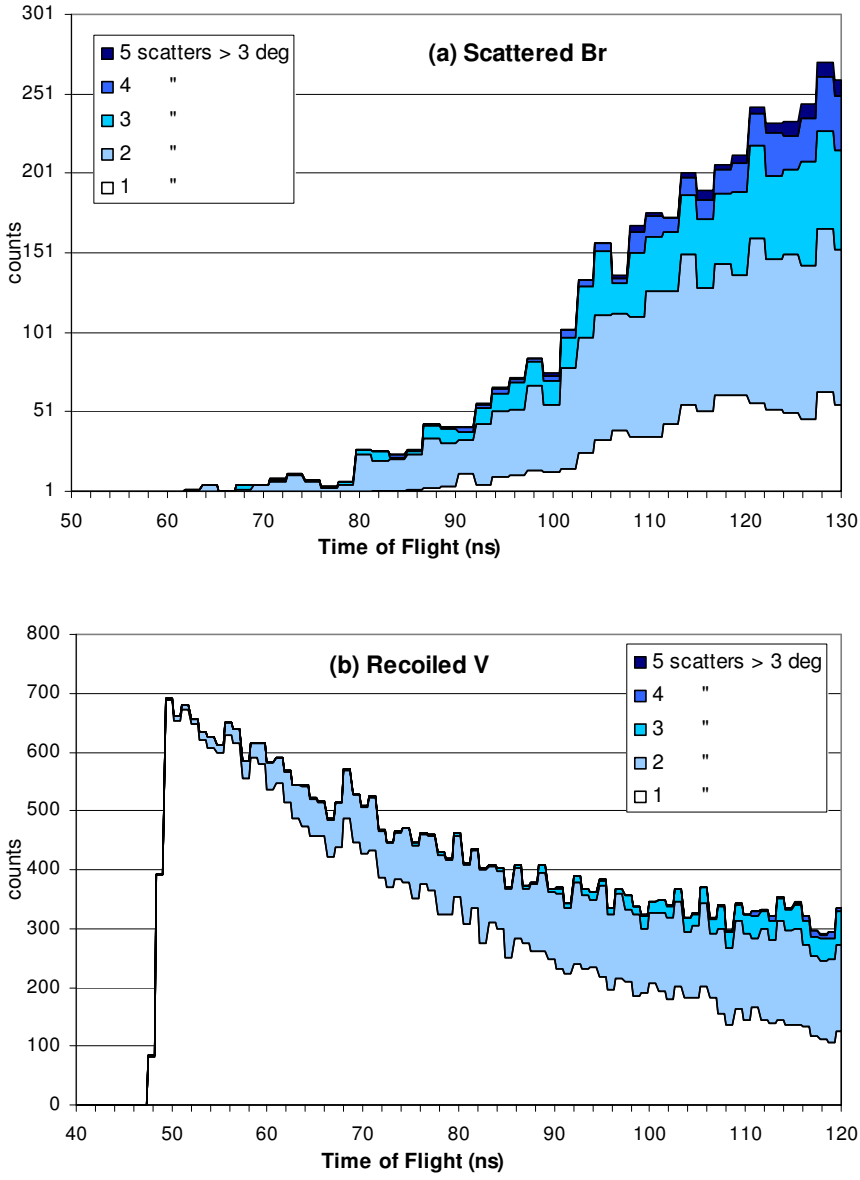

Figure 6.5 Simulated spectra for Bromine on Vanadium showing contributions to spectral shape from ions having 1, 2, …, 5 scattering events for (a) 60 MeV Br ions scattered beyond the critical angle, θ_c= 39.6˚, and (b) recoiled V atoms.

6.4 Path Complexity in Plural Scattering

It is clear from the two preceding sections that there are many complicated paths which lead to ions and recoils reaching the detector. A plurally scattered path leading to a detector at 45˚ from the beam-line may involve two deflections of similar magnitude, a large deflection together with one or more small deflections, or a more complex combination of these. We are interested in the degree of complexity of paths and the frequency with which different complexities occur.

In Figure 6.6 we illustrate the varying degrees of complexity of the paths of I ions and Au recoils reaching the detector. In panel (a), the 10 largest scattering angles are shown for each of 100 randomly chosen ion histories. Each curve represents the data for a single ion. Panel (b) shows similar data for 100 recoils. The majority of paths resemble our idealisation of single scattering, having a 45˚ scatter with the remainder of the path slightly perturbed by the multiple scattering process. The point **P** marks the plural scattering condition discussed in section 6.2, i.e. a second direction change of 3˚ or greater. The curves which pass above **P** are the plurally scattered paths.

There are 28 such curves in this sample of 100 ions. Several of these appear as double scatters having the third and subsequent events down in the small angle multiple scattering region. Most exhibit a complex plural scattering history with some having up to 10 or more significant direction changes. In the simulated spectra shown in Figure 6.2 (a) and Figure 6.3 (a), 27% of scattered I ions detected with a Time of Flight < 100 ns suffered plural scattering of greater than 3˚.

The recoil paths depicted in Figure 6.6 (b) appear to be less convoluted than those of the ions in panel (a). The distinctive curves of those recoils having a high degree of plural scattering are not as blatantly separated from the conventional multiple scattering region as they are for the ions. It is interesting to note, however, that there are 40 curves which lie above the point **P**. i.e. for the entire simulated spectrum shown in Figure 6.2 (b) and Figure 6.3 (b), 40 % of recoiled Au atoms having a ToF < 140 ns, satisfied the 3˚ plural scattering condition. Plural scattering is more probable for

the recoiled Au atoms due to their lower kinetic energy, and the increased scattering cross section of higher Z elements.

Plural scattering complexity plots are shown in Figure 6.7 for the scattered I and recoiled Ta and O from the 326 nm Ta_2O_5 sample. As was shown in Figure 6.4, plural scattering features strongly for both the scattered I and the recoiled Ta. In Figure 6.7 (a), plurally scattered paths of every degree of complexity are visible and 71 of the 100 ion paths lie above the point P signifying the plural scattering condition i.e. the majority of detected ions were plurally scattered. The higher incidence of plural scattering in this example is due to the increased thickness of the sample, and to the lower energy of I ions scattered from Ta. As Ta is closer in mass to I than Au is, more energy is transferred to Ta in the binary collision.

The recoiled Ta spectrum is similarly dominated by plural scattering. Again, 71 % of paths lie above the point P. Interestingly, there is a distinct grouping of paths that would be classified as double scatters, having two large deflections greater than 20˚. Many of these can be seen to have had a significant third deflection. The recoiled O spectrum is far less influenced by plural scattering due to the lower interaction cross section of the lighter element. 26 % of detected O recoils were plurally scattered.

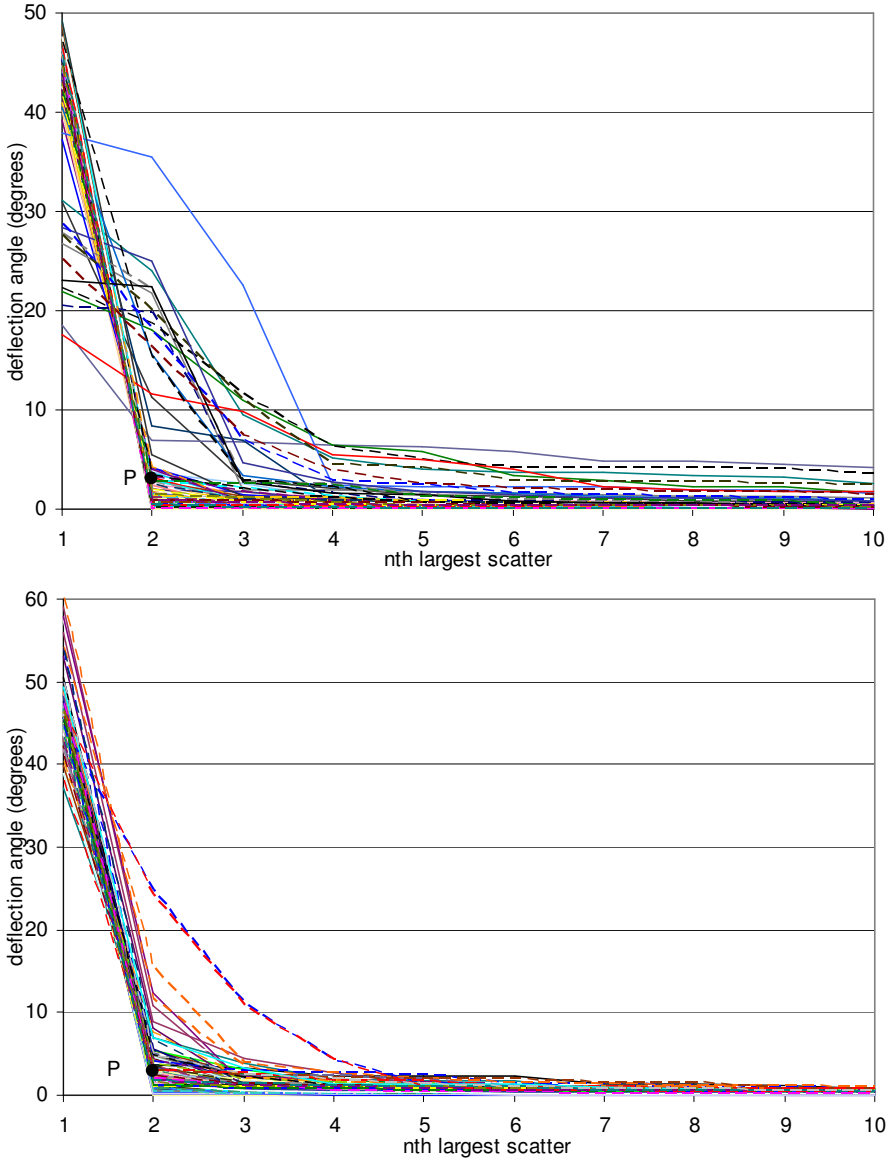

Figure 6.6 The 10 largest scattering angles in the paths of (a) 100 randomly selected I ions; and (b) 100 randomly selected Au recoils reaching the detector. The point P indicates the plural scattering condition of a second scatter greater than 3˚.

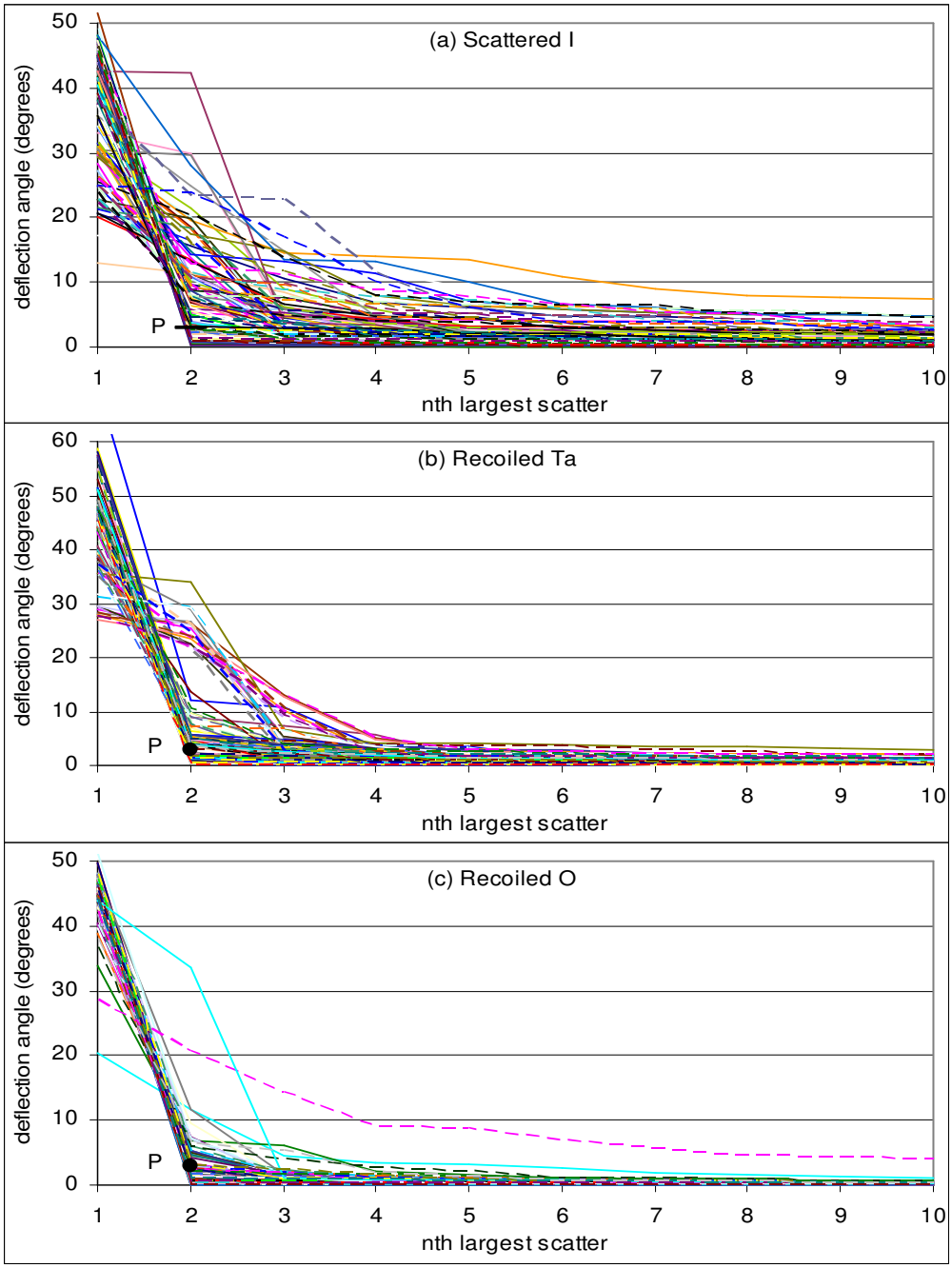

Figure 6.7 The 10 largest scattering angles in the paths of (a) 100 I ions; (b) 100 Ta recoils; and (c) 100 O recoils reaching the detector. The point P indicates the plural scattering condition of a second scatter greater than 3˚.

6.5 Conclusion

We have shown that Monte Carlo simulation can be used to analyse the paths of detected ions and recoils in HIERDA. By interrogating the scattering histories of individual particles, we can discriminate between multiple scattering and plural scattering, although the distinction is subjective. With a suitable definition of plural scattering, the contribution to the output spectra of plurally scattered ions and recoils can be separated from that of single scattering, showing that certain features of the typical HIERDA spectrum are due to plural scattering. This enables comparison with predictions by analytical simulations and shows that those not incorporating plural scattering are unlikely to predict the correct shape of experimental spectra and that errors in sample description are a likely consequence. The plural scattered component of a spectrum may be further broken down into contributions by particles with different degrees of complexity of their paths within the sample.

In the two examples studied, a significant contribution to output spectra was shown to exist from ions and recoils having up to 5 significant deflections in their paths. Contributions were observed from particles having up to 10 deviations greater than 3°.

Chapter 7

Resolving Overlapped Signals in HIERDA

Monte Carlo simulation has so far been applied to the problem of generating HIERDA spectra and correctly accounting for features caused by multiple and plural scattering. While these influences affect the depth resolution of the technique [33, 69, 70], HIERDA also suffers from decreasing mass resolution for very heavy ions that is a consequence of the poor energy resolution of Si detectors for heavy ions [2, 45]. The Time of Flight–Energy (ToF-E) detection system described in Chapter 3 is dependent upon the energy signal for its elemental separation. This energy and mass resolution problem is further aggravated by energy calibration shifts associated with radiation damage of the Si detector [48, 106].

As a consequence, signal overlap can occur in cases where signals from recoils of similar atomic mass cannot be resolved. Mass-overlapped signals in HIERDA have been identified as a problem by several groups. Johnston et al. [45], Persson et al. [52], and Stannard [5], have published strategies for dealing with isotopic separation of overlapped elemental energy spectra. A particular class of problem involves the interference between the scattered beam signal and those of recoiled target atoms. If the sample contains elements of similar atomic mass to the beam ion, then the finite mass resolution of the detection system may result in their signals overlapping (see for example, the case of overlapping scattered Ag and recoiled In reported by Shrestha and Timmers [57]). This ambiguity makes data interpretation difficult [50, 52, 107, 108], but is a problem amenable to treatment using the Monte Carlo simulation developed in this work since the calculation of the scattered ion spectrum is a feature of the code.

In this chapter we present an example of the latter case in which a sample containing Ag is analysed using an I beam. The Ag and I are sufficiently close in mass that their output signals partially overlap in the Time vs. Energy plane and cannot be reliably separated. In the simulation, the scattered ion spectrum can be unambiguously separated from the recoil signal and is used to show an example of the error likely to occur if an attempt is made to graphically divide the experimental data.

7.1 Scattered Ion Spectra

Time-of-Flight/Energy detection was developed to overcome the mass-depth ambiguity inherent in recoil spectrometry. However energy detector resolution imposes a mass separation limitation significant for heavy atoms - particularly for recoil species heavier than the beam species where transferred energy decreases with increasing mass.

Recoil-projectile ambiguity remains in the context that the beam species may also be present in the sample. This is normally controlled by using a heavy beam species and exploiting the critical scattering angle for a heavy incident ion scattering from a lighter atom, ensuring that the detection angle lies beyond the critical angle. However, as was shown in Chapter 4, multiply scattered ions may still reach the detector, and particularly when analysing multi-elemental samples, it is not always possible to use a beam species heavier than, or different from, all species present in the sample. In some cases, it is possible to avoid the problem by exploiting the scattering kinematics to enhance the energy differential between species, or to increase the energy of detected particles thereby improving the resolution of the energy detector. In some facilities, the detection angle is also variable offering another degree of freedom. Different detection angles, higher incident energies and heavier analysing ions are not always available, so eliminating mass-overlapped signals is not always possible.

In the code, each atomic species is unambiguously identified, and beam ions are explicitly identified independently of the same species present in the sample. The contribution of scattered ions and recoils of the same species may be generated independently and summed for direct comparison with the overlapped experimental data. In the case of signal overlap between the scattered ion and a recoil species, MC simulation that includes the scattered ion spectra allows for the validation of the simulated recoil spectra by directly quantifying the contribution from the scattered ions.

All of the efficiency enhancements implemented in this code have been designed to retain all detected particles and to maintain the ability to generate the scattered ion spectra. Experimentally, these have been shown to contain valuable information in cases where the signals of very heavy recoils overlap [45]. These spectra are also important in cases where the scattered beam signal interferes with the signals of recoiled target atoms [57].

The inclusion of the scattered ion spectra comes at a cost in terms of processing time due to several factors. The ions themselves must be transported in the code, and some restrictions are placed on which variance reduction techniques can be employed. The MCERD code of Arstila [8, 9] exploited a number of techniques at the expense of the ability to generate the scattered ion spectra. The ‘forced interaction’ technique, achieved by artificially reducing impact parameters, takes advantage of the association between the small impact parameters required to produce recoils, and the low probability of these occurring randomly. The inclusion of the ion spectra requires a larger range of impact parameters to be allowed reducing the benefit that can be gained. The ‘secondary particle enhancement’ technique is further restricted in that it is necessary to maintain the correct ratios between recoil production and scattered ion yield. Since the publication of this work [91], MCERD has been modified and now includes simulation of the scattered ion spectrum [9].

7.2 Experimental Configuration and Sample Description

A sample containing Ag is analysed by an 82.5 MeV I beam in the experimental configuration described in detail in Chapter 3. The sample is a double layer of Ag with an intermediate amorphous hydrocarbon layer. The surface layer of Ag is 166 nm thick, the intermediate hydrocarbon layer is 50 nm, and the buried Ag layer is 165 nm. The layers are deposited on a Si substrate (see Figure 7.1)

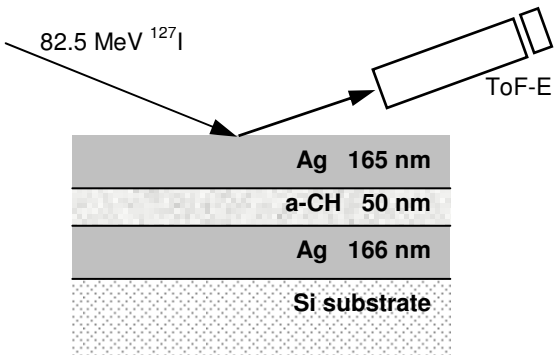

Figure 7.1 Sample consisting of double Ag layers with intermediate amorphous hydrocarbon layer, analysed with an 82.5 MeV ^{127}I beam.

This sample is one of a set of double metal layer samples that have previously been used by Szilagy and co-workers to study the influence of multiple scattering on depth resolution in hydrogen profiling by ERDA [69, 70].

7.3 Results

Figure 7.2 shows the two dimensional Time of Flight versus Energy spectrum from a measurement of the double Ag layer sample, analysed with an 82.5 MeV ^{127}I beam. The recoiled Ag and scattered I signals are prominent, although it is difficult to distinguish the two peak regions along each elemental arc corresponding to the two Ag layers. The signal intensity between these regions is only slightly lower than the peaks due to pronounced multiple scattering as a result of the high

cross sections for scattering of Ag and I in Ag, and the high energy transfer between particles of similar mass. The intermediate hydrocarbon layer is relatively thin and has a low total areal density so the tailing effects at its upper and lower interfaces overlap substantially almost obscuring the gap between the Ag layers.

Also visible in this plot are the signals from the Si substrate, some O contamination on the Si surface prior to layer deposition, and the C in the intermediate layer. The H signal from the intermediate layer cannot be seen due to the Energy pulse height gain and Time Delay settings chosen optimally for heavy element detection.

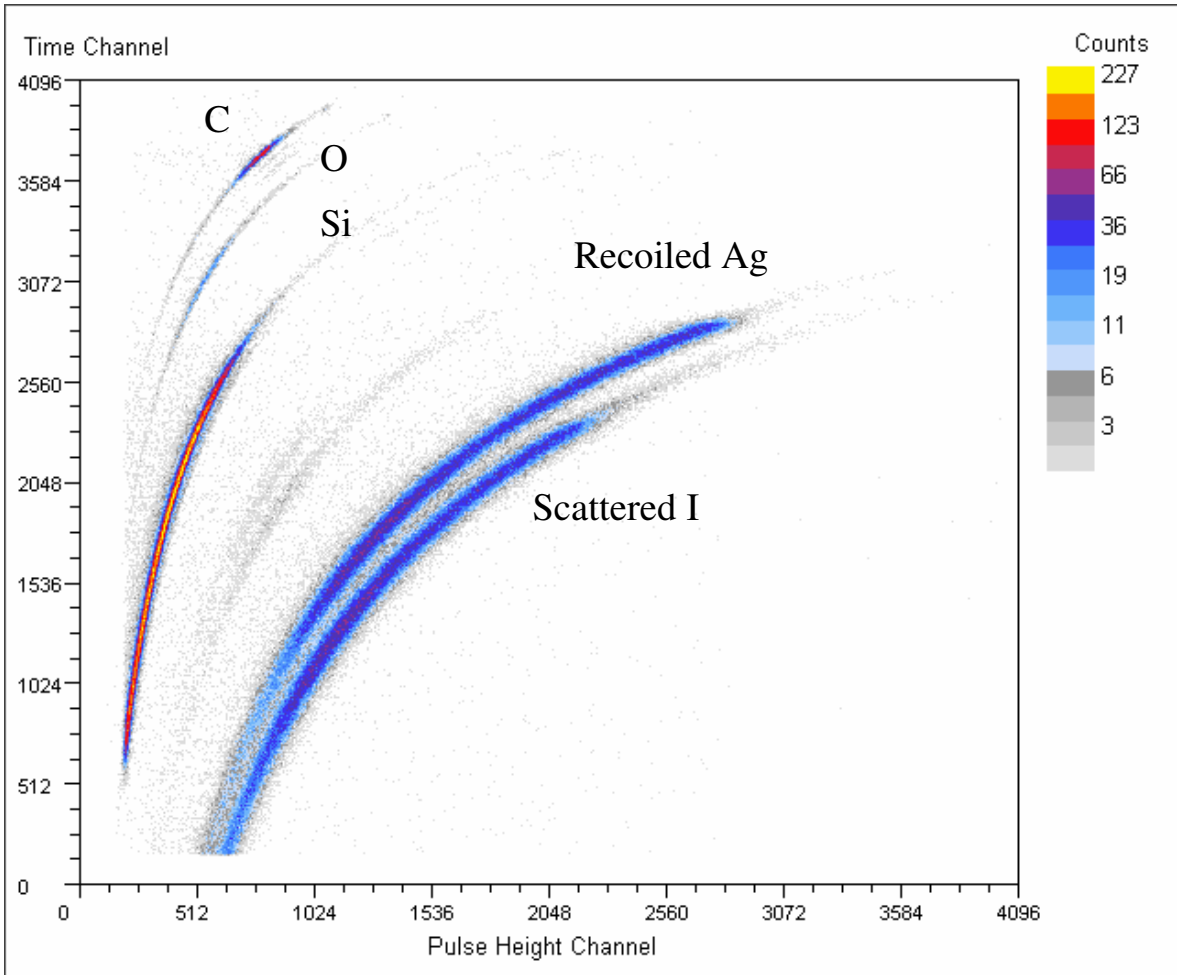

Figure 7.2 Time of Flight vs Energy histogram of the Ag/a-CH/Ag/Si sample measured using an 82.5 MeV I beam showing the overlapping Scattered I and Recoiled Ag signals.

7.4 Discussion

The scattered I signal overlaps the recoiled Ag signal making it difficult or impossible to separate the data into elemental subsets for generating the individual Time of Flight projections. An attempt to do so will result in the loss of some counts which should have been included in each projection, and/or the inclusion of counts belonging to the profile of a different element. Therefore the absolute yield in each extracted profile could not be considered to accurately represent the sample.

The Monte Carlo simulation can be used to overcome this problem. The simulated data can be precisely separated to yield the two profiles, and the correlation with experimental output can be validated against the *sum* of the two spectra. The subset of data containing these two sets of points (see Figure 7.3) is cut from the Time vs Energy plane and projected to the Time of Flight axis. The two corresponding simulated spectra are superimposed into a single projection to be compared with the experimental data.

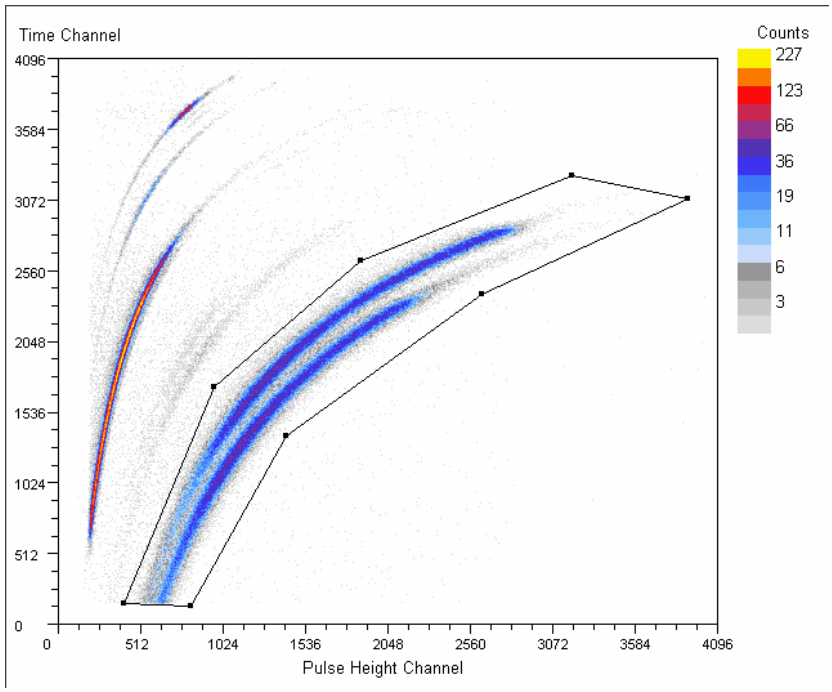

Figure 7.3 The 2-dimensional Time of Flight versus Energy histogram for the Ag double layer sample showing the geometrical cut of the combined I and Ag signals.

The results of this procedure are shown in Figure 7.4 displaying excellent agreement. This indicates that the sample specification in the model is representative of the real sample. This would not be the case if an attempt had been made to match the individual profiles using inaccurately separated experimental data.

An attempt to separate the recoiled Ag and scattered I spectra and compare them with the simulation is shown in Figure 7.5 The simulation appears to underestimate the Ag yield in the 65-85 ns region, and to overestimate the I yield in the 75-90 ns region. However, the excellent agreement between the experimental and simulated data in the combined spectrum (Figure 7.4) indicates that the error is in the process of separating the overlapped experimental contributions.

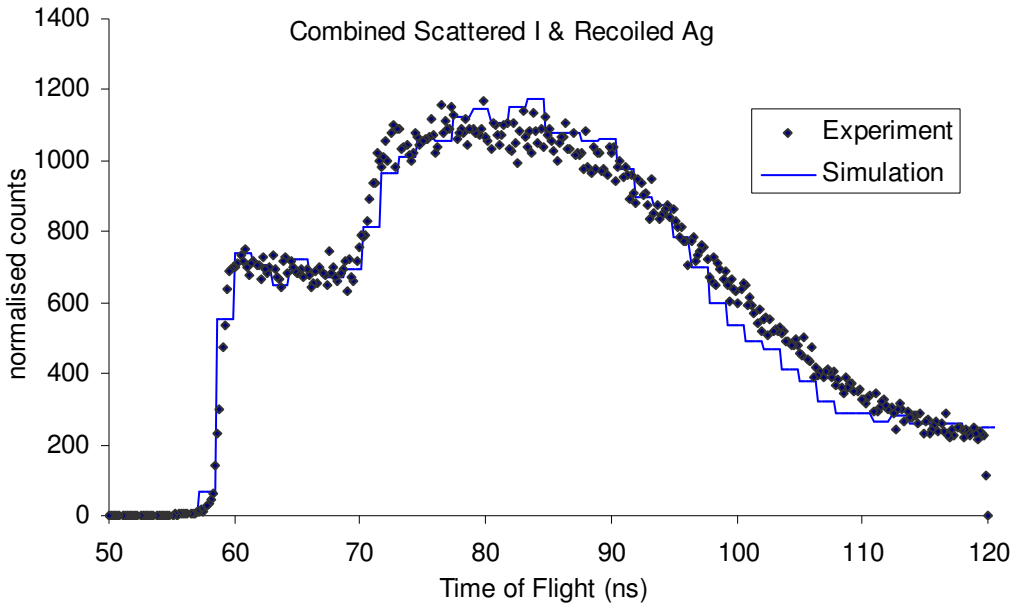

Figure 7.4 The Time of Flight projection of the scattered I and recoiled Ag signals, extracted as a single combined subset of the ToF-E histogram, compared with MC simulated spectrum.

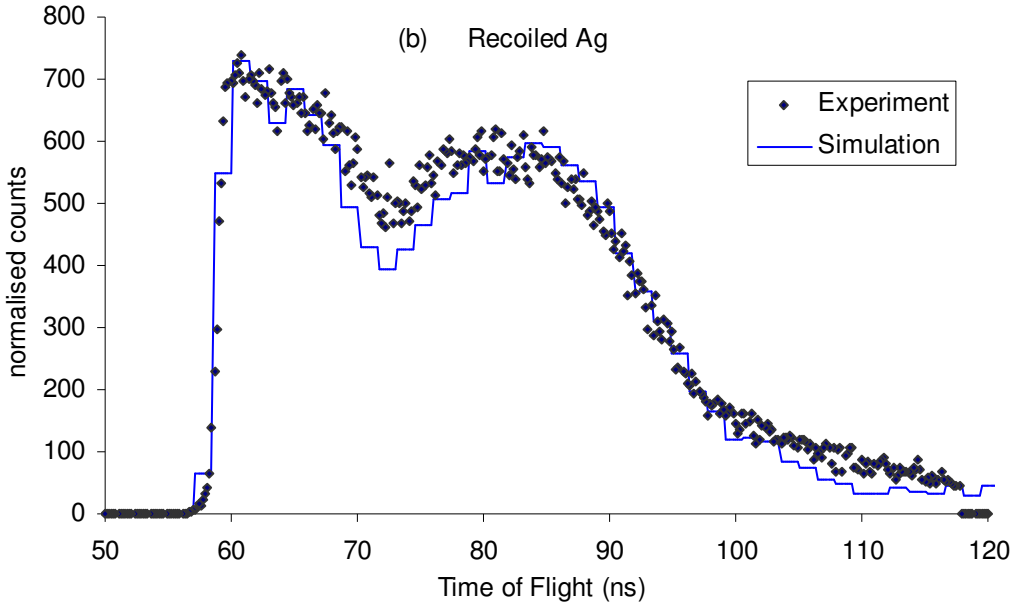

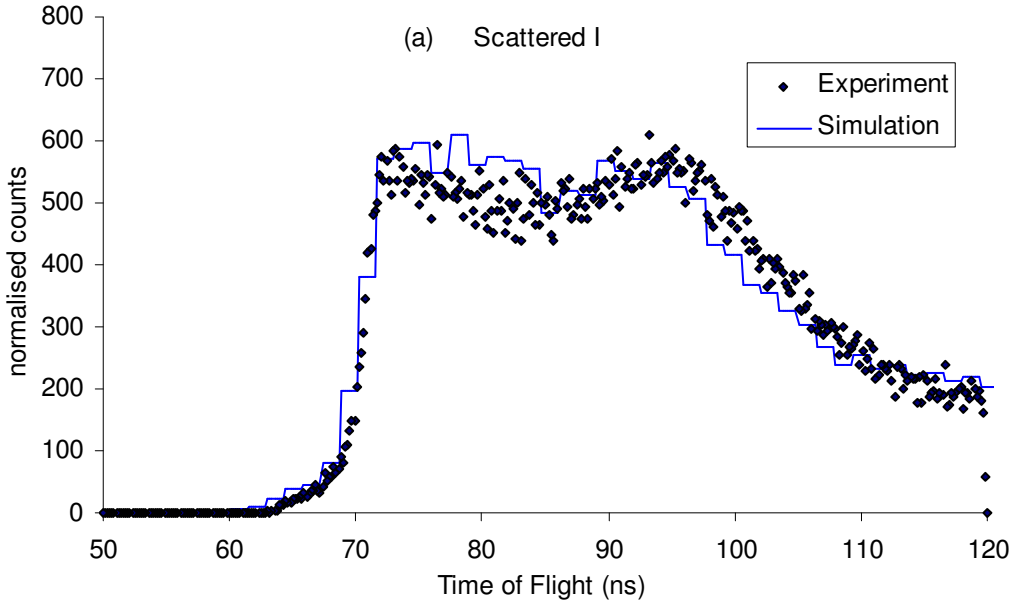

Figure 7.5 Time projections for the (a) Scattered I and (b) Recoiled Ag signals compared with MC simulation. The apparent discrepancies in the 70-85 ns region are due to the impossibility of separating the individual signals in the experimental data.

If the comparison of the combined spectrum had not been made, then the discrepancies seen in Figure 7.5 could lead to the adjustment of the sample description in the model to obtain a better match. This process would result in an incorrect description of the experimental sample.

It is also possible that a satisfactory match might not be achievable in a situation such as this. In an attempt to increase the recoiled Ag yield in the 70 – 80 ns range corresponding to the hydrocarbon layer, a Ag component might be assumed or some other density increase introduced. Either of these would be likely to increase the scattered I yield in that region contrary to the decrease required by the over-estimation apparent in Figure 7.5 (a).

In this example, the region of the Ag spectrum in question is entirely generated by multiple and plural scattered atoms, as there is no Ag in the intermediate layer. The counts here are due to the overlap of the tailing features from the two layers. Consequently it would be extremely difficult, if not impossible to correctly match this region using a simulation technique that did not include these effects.

The scattered I spectrum can also be shown to be heavily influenced by plural scattering. The regions corresponding to the two layer peaks are poorly resolved. Using the technique described in Chapter 6 for the breakdown of plural scattering contributions to spectra, we can see that more than 60 % of the counts in the I spectrum, and over 40 % of the Ag counts have been significantly scattered more than once (Figure 7.6).

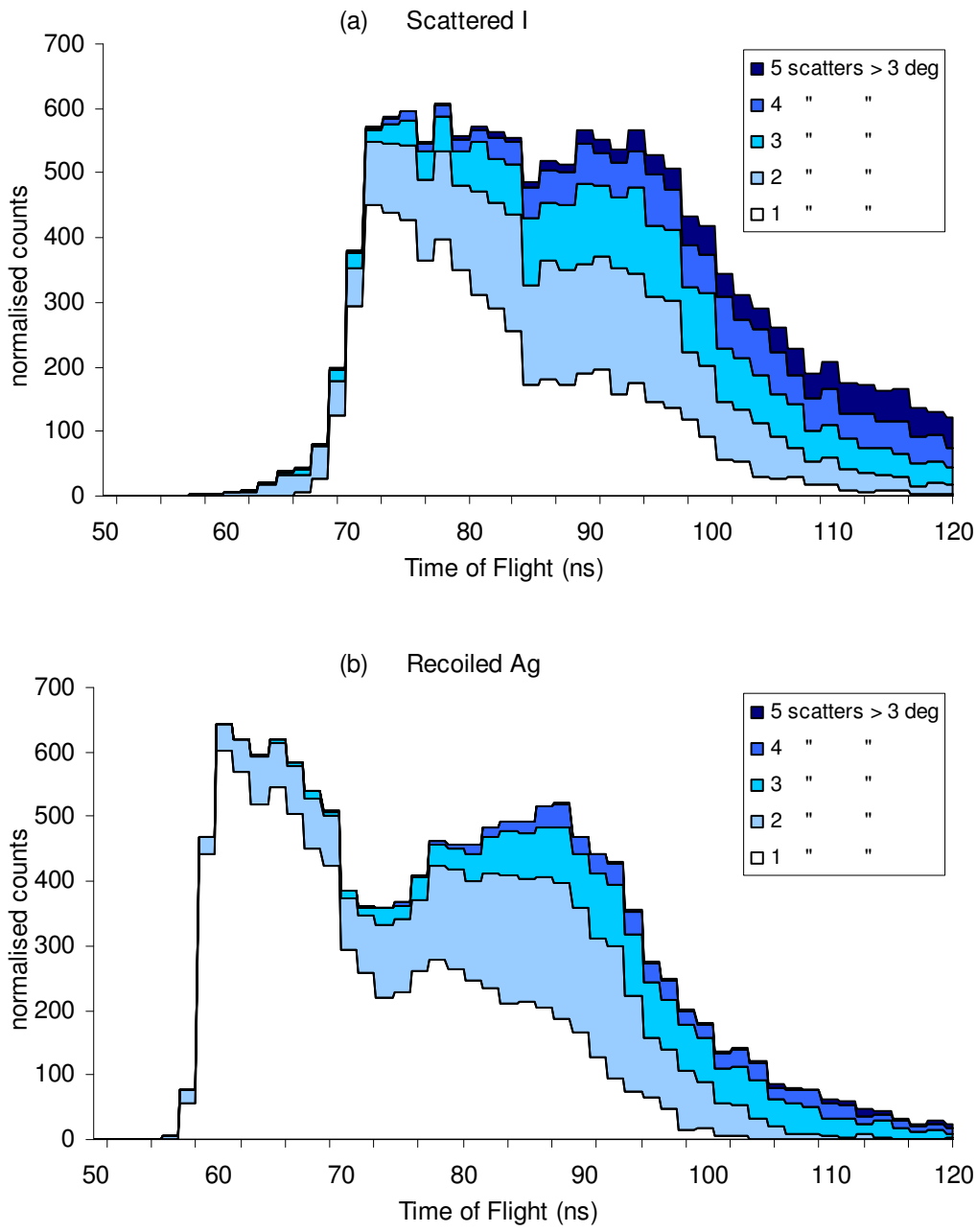

Figure 7.6 MC simulated Time spectra showing plural scattering contributions to spectral shape from ions having 1, 2, …,5 scattering events for (a) scattered 82.5 MeV I ions and (b) recoiled Ag atoms.

7.5 Conclusion

Overlapping signals in the output spectra of HIERDA experiments can make accurate data interpretation difficult because the contributions from atoms of different species cannot be experimentally separated. This can lead to an incorrect sample description during the process of simulation and matching. Problems of this type are amenable to treatment using Monte Carlo simulation. In cases where one of the interfering signals is that of the scattered incident ions, it is necessary that the simulation of the ion spectrum is included in the code. The signals from individual atomic species can be explicitly separated in the simulation and this allows individual elemental profiles to be generated even when they cannot be distinguished experimentally.

An example has been presented in which the scattered ion signal and a recoil target species signal overlapped. Using the Monte Carlo code, the individual profiles were calculated, and a procedure presented for validating the simulation results by spectrum matching against the summed spectra of the overlapped signals. The error likely to occur if the spectra were matched using incorrectly separated experimental profiles was also shown.

In the following chapter, we consider another experimental ion beam problem in which large angle scattering of incident ions is responsible for dominant features in output spectra. Once again, Monte Carlo simulation and its explicit modelling of individual interactions allows for the analysis of individual ion contributions. In this case, the viability of nano-aperture masking of a focused ion beam will be tested and optimised prior to experimental investigation of its applicability to Ion Beam Lithography.

Chapter 8

Ion Transmission through Nano-Apertures

The formation of a very small beam spot by collimating a focused ion beam with a nano-aperture mask is a problem made complex by large angle scattering. The effectiveness of aperture collimation is limited by ion scattering and straggling in the walls and near-aperture region of the mask. Transmitted ions will have altered direction and energy if their passage through the aperture included scattering interactions in the mask material. The net effect will be a beam broadening at the aperture exit analogous to the penumbra seen in radiotherapy and optical collimation of non-point sources. In this chapter, Monte Carlo simulation is used to conduct a feasibility study for the proposed use of apertures for ion beam localisation for an ion beam lithography application. The results are relevant to a wider range of ion beam applications involving nanometre beams.

8.1 Introduction

Ions and the energy they impart to a target can be manipulated to modify materials in a controlled way. Nano-fabrication refers to the manufacture of three-dimensional structures on the sub-micron scale (see the review by Watt et. al for examples [109]). Focused ion beams have been employed in nano-machining – the shaping of material by ablation or 'sputtering' of surfaces by low energy ions (see review article by Reyntjens and Puers [110]). A process known as 'Ion Beam Lithography' (IBL) exploits the damage track induced by the passage of penetrating ions to render the damaged material susceptible to chemical etching. A notable example is the fabrication of photonic devices by proton beam writing at the National University of Singapore [111-114]. An attractive feature of

ion beam technologies for sub-100 nm lithography is the absence of a fundamental diffraction limit as in optical lithographic techniques. Another established technique, Electron Beam Lithography (EBL), is limited by pronounced broadening of the electron beam with depth due to electron scattering in the sample. This makes EBL unsuitable for the production of high aspect ratio structures.

Current work by Alves and co-workers [115, 116] seeks to approach the lower spatial limits of the IBL technique by etching single ion damage tracks, the dimensions of which are in the order of 20 nm. Small numbers of co-located or closely spaced ion tracks are also being considered. High energy (E > 1 MeV/amu) ions are used as they evenly deposit energy over a long range in a straight damage path. Etching the latent damage tracks allows the creation of high aspect ratio structures with a resolution potentially in the order of 10 nm by tailoring the dose threshold in the etching process [115]. High precision placement of these ions is necessary. One potential technique to enable this is the use of a nano-aperture mask.

Schenkel et. al. have described some success with the use of nano-apertures for the localisation of single low energy (10 – 15 keV) ^{31}P ions implanted into Si. Arrays of ^{31}P in Si with spacing in the order of 100 nm at an accuracy of +/- 10 nm, have been described as a suitable candidate [117] in the development of a solid state quantum computer based upon the spin states of single atoms in the model proposed by Kane [118]. Interactions with the aperture walls are inferred from charge exchange measurements of transmitted ions, but they have not studied the associated momentum transfer and angular distributions that will influence the final rest positions of the ions within the substrate. The effectiveness of an aperture mask is less certain for high energy ions required for applications such as that of Alves.

There are two main methods for the precision delivery of ions to sub-100 nm resolution: focusing by means of electric or magnetic lenses or by collimation with apertures. For MeV ions, focusing is generally preferred because of the difficulty of making the required high aspect ratio nano-

apertures in a mask that is otherwise opaque to the beam. However, focusing ions to sub-100 nm beam spots entails considerable technical complexity [115] and substantial investment in necessary hardware. Sub-100 nm focusing has only been achieved in one laboratory [119], and is not generally reproducible. With the advent of methods for making sub-100 nm high aspect ratio apertures [116, 120-122], this collimation approach is increasingly attractive.

Ion scattering and straggling through the walls of the aperture and the fact that all materials are partially transparent to MeV ions will limit the spatial resolution for the delivery of ions regardless of the diameter of the aperture itself. The magnitude of beam-spread beyond the aperture, and the effect on the energy distribution of transmitted ions can be modelled with Monte Carlo ion transport simulation, which this work has shown to be a useful technique for studying problems in which individual ion histories are important.

The ions of primary interest are the fraction which are not transmitted directly through the aperture, but have a trajectory that intersects the aperture wall, or are incident upon the mask near the aperture and subsequently scatter into the aperture so that they are transmitted through the mask albeit with altered direction and reduced energy.

8.2 Monte Carlo Simulation of Nano-Aperture Collimation

The Monte Carlo simulation code for modelling the passage of ions through a nano-aperture mask, is based upon the code described in detail in Chapter 4 of this thesis. Modifications were made to allow the geometry of the mask to be represented, as the original TRIM code and HIERDA adapted code assume the sample to be laterally homogeneous. These changes are described below. Most of the efficiency enhancements described in Chapter 5 are not used as they are specific to the HIERDA simulation and are not applicable to transmission experiments and inhomogeneous samples.

8.2.1 Ion Transport Modelling Changes

The original code modelled ion transport in a 2-Dimensional projection for efficiency reasons. The present code models the ion transport in 3-D which is required to correctly model all possible individual ion paths that intersect the aperture.

The direction cosine transformations for calculation of scattered particle trajectories are as described by Peplow [123] for efficiency, as no coordinate system transformations are required. For a particle with an initial unit direction vector Ω = [u, v, w], scattered through a polar angle θ and an azimuthal angle ϕ, the new direction is given by:

$$\Omega' = \begin{bmatrix} u' \\ v' \\ w' \end{bmatrix} = \begin{bmatrix} u \cdot \cos(\theta) + \cos(\phi) \cdot \sin(\theta) \cdot \dfrac{u \cdot w}{\sqrt{1 - w^2}} + \sin(\phi) \cdot \sin(\theta) \cdot \dfrac{-v}{\sqrt{1 - w^2}} \\ v \cdot \cos(\theta) + \cos(\phi) \cdot \sin(\theta) \cdot \dfrac{v \cdot w}{\sqrt{1 - w^2}} + \sin(\phi) \cdot \sin(\theta) \cdot \dfrac{-u}{\sqrt{1 - w^2}} \\ w \cdot \cos(\theta) + \cos(\phi) \cdot \sin(\theta) \cdot \dfrac{w^2 - 1}{\sqrt{1 - w^2}} + \sin(\phi) \cdot \sin(\theta) \cdot \dfrac{0}{\sqrt{1 - w^2}} \end{bmatrix} \tag{8.1}$$

and in the particular case where |w| ≈ 1 i.e. the direction vector is approximately parallel to the *dependent* coordinate axis (in this case the transverse or Z axis),

$$\Omega' = \begin{bmatrix} u' \\ v' \\ w' \end{bmatrix} = \begin{bmatrix} \sin(\theta) \cdot \cos(\phi) \\ \sin(\theta) \cdot \sin(\phi) \\ \dfrac{w \cdot \cos(\theta)}{|w|} \end{bmatrix} \tag{8.2}$$

As the sample is not laterally homogeneous, ion positions relative to the aperture central axis are tracked explicitly. Incident ions may be made incident at any point relative to the aperture. Position coordinates are recorded for transmitted ions together with direction cosines and energy.

8.2.2 Geometry

The mask is modelled as one or more planar layers, with a cylindrical void to represent the aperture. Ions that enter the aperture are transported, without electronic energy loss or nuclear scattering, to the point at which the trajectory again intersects with the aperture wall or is transmitted beyond the back surface of the mask. The points of intersection of the trajectory and the aperture wall are determined by equating and solving the parametric equations for a cylinder and a line of any free flight segment which enters the aperture.

8.2.3 Finite Source Definition – The Beam Spot

The ions of interest are those which do not simply pass unimpeded through the aperture, but have a trajectory that intersects the aperture wall, or are incident upon the mask near the aperture and subsequently scatter into the aperture and are transmitted through the mask. Thus it is important to model a realistic ion beam spot size and distribution.

In the original TRIM code, incident ions were modelled as an infinitesimal beam spot. The present code allows the finite size of the beam spot over the mask to be specified as an input parameter. The beam flux profile may be specified as Uniform, to approximate the local flatness in the centre of the beam, or as Gaussian. A Gaussian beam profile is parameterised by the standard deviation, σ, where

$$\sigma = \frac{FWHM}{2\sqrt{2\ln(2)}} \approx \frac{FWHM}{2.3548} \tag{8.3}$$

for the Normal distribution, and FWHM is the Full Width at Half Maximum for the beam being modelled. The full extent of the beam diameter is 12 standard deviations.

The simulated ion beam can be offset from the central axis of the aperture, and ions can be initiated with incident angles consistent with the ion beam that delivers the ions to the mask. In this way, issues related to the alignment of the aperture with the beam can be investigated. Alignment is an

important experimental issue for the high aspect ratio apertures required to ensure the mask is opaque to high energy ions.

8.3 Experimental Configuration

Nano-scale apertures have been drilled by Focused Ion Beam systems in silicon cantilevers. Similar masks have been used by Luthi et al. [124] for nano-stencil deposition, and by Schenkel et al. [125] for low energy single ion doping. These structures are attractive for use as a nano-stencil due to the potential for sub-1 nm control of the position of the aperture in the cantilever above the substrate as well as precision mapping of location markers on the substrate by Scanning Probe Microscopy. Scanning electron microscopy (SEM) images of apertures in silicon cantilevers [124, 126] show a radius of the order of 100-200 nm can be achieved. We therefore apply our model to high-aspect ratio apertures in Si masks.

The mask is modelled as a uniform Si layer with a 100 nm radius cylindrical aperture through a layer whose thickness is typically 10 – 30 μm, chosen to be approximately twice the range of the incident ions used in each case. Thus these collimating apertures have a high aspect ratio - in the order of 1:100. The MC simulation is applied to various ion-energy combinations and aperture sizes to demonstrate their effects on the transmission spectra. In practice, the ion beam is delivered onto the mask by a focused ion beam system, such as a nuclear microprobe, where the beam spot will be much larger than the aperture. For these simulations the beam is modelled with a radius of 1 μm. To obtain insights into the influence of ion energy, mass and range, simulations have been run for 2 MeV and 4 MeV He ions, which have been investigated by Alves for ion beam lithography, and for 8 MeV F and 71 MeV Cu ions which have been considered as candidates for single ion lithography [116, 127].

8.4 Results and Discussion

In each simulation, 10^7 incident ions were modelled, except for 71 MeV Cu which used 10^6 ions due to the much longer simulation times associated with high energy heavy ions. The ion beam was modelled as a 1 μm beam spot, comparable to those readily available experimentally. For each transmitted ion, the simulation calculates the energy, position and direction cosines at the point of exit from the mask. The effectiveness of the collimator may be characterised by these parameters. The spatial map or radial plot of ions emerging from the back of the mask indicates the frequency and spread of those ions which penetrate some portion of the mask in the lower region of the aperture. The angular distribution is relevant as it describes the extent to which the effective collimated beam spot size will be amplified by projection from the back of the mask to the target surface. The energy distribution describes the efficacy of transmitted ions for energy deposition in the target.

8.4.1 Effectiveness of Collimation

Figure 8.1 shows the results of simulations of 2 MeV He (Figure 8.1 (a)), 8 MeV F (Figure 8.1 (b)), and 71 MeV Cu (Figure 8.1 (c)) through a 100 nm radius aperture. The spatial distribution and mean energy of transmitted ions are shown as a function of radial distance from the centre of the aperture. The distribution of transmission angles from the sample normal is also shown.

8.4.2 Spatial Resolution

The spatial distributions (the solid lines in Figure 8.1 (a, b and c (ii)) display very steep sided features corresponding to the edges of the aperture, and show this aperture to be highly effective for each ion-energy combination modelled. There is some tailing extending out to approximately 4 aperture radii, although the intensity reduces to less than 0.5 % beyond 2 radii and below 0.07 % at 4 radii, in all three cases. Some statistical noise is evident near the centre of the intensity

distributions due to the reducing area of the evenly spaced radial bins, and is more pronounced for the 71 MeV Cu due to the fewer ion histories processed.

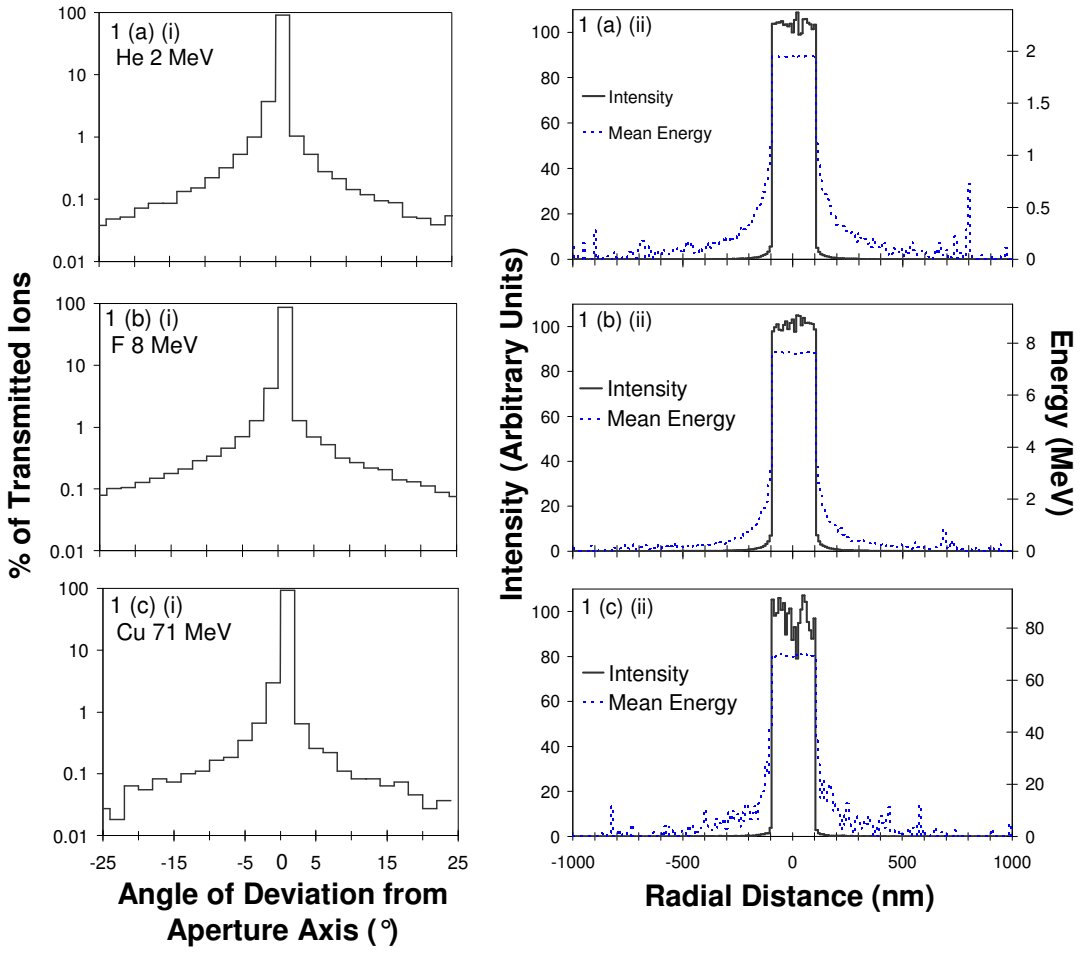

Figure 8.1 Transmission of (a)(i,ii) 2 MeV He, (b)(i,ii) 8 MeV F and (c)(i,ii) 71 MeV Cu through a 100nm radius nano-aperture.

To parameterise these distributions and the effectiveness of the collimation, the following quantities are defined: the percentage of transmitted ions which exit the aperture while retaining their full energy is denoted by T. Of all transmitted ions, a fraction, S_{out}, are scattered *out* of the aperture, and S_{in} are scattered *in* to the aperture spot with reduced energy. The mean energy of these inwardly scattered ions is $\bar{E}_{in}$. For single ion applications, the radial intensity, direction, and energy plots are interpreted as probability distributions. The quantity T is the probability that a transmitted ion will be an *ideal* outcome i.e. transmitted unimpeded through the aperture to the

target. S_{out} is the probability that a transmitted ion will be outside the intended area; S_{in} that it will be in the intended area but deficient in energy; and $\bar{E}_{in}$ the expected energy for these latter ions. Table 8.1 summarises these quantities for each ion-energy system.

Table 8.1 Distribution parameters for several ion-energy systems: percentage of ions transmitted with full energy, T, percentage of transmitted ions scattered *out* of the aperture, S_{out}, scattered into the aperture, S_{in}, and the mean energy of the latter ions, $\bar{E}_{in}$

Ion / Energy		Aperture Radius (nm)	T (%)	S_{out} (%)	S_{in} (%)	$\bar{E}_{in}$ (MeV)
He	2 MeV	100	86.4	3.51	10.1	0.99
F	8 MeV	100	82.2	4.54	13.2	3.24
Cu	71 MeV	100	90.3	2.15	7.59	31.6
He	2 MeV	40	92.8	2.42	4.79	1.02
He	4 MeV	100	89.8	3.16	7.00	2.11

For a 1 μm radius ion beam centred on a 100 nm radius aperture (1% of the beam area), the total percentage of ions transmitted is 1.15 %, 1.22 % and 1.09 % for He, F and Cu respectively. These numbers are greater than 1 % indicating the small degree to which ions scattering in the walls of the aperture are transmitted. Of the transmitted ions, 82 – 90 % will be at full energy within the spot, with 71 MeV Cu having the highest result; 2.2 – 4.5 % will be outside the spot; 7.6 – 13.2 % inside the spot with a reduced mean energy of 40 – 50 % of the incident energy. In each case, the 71 MeV Cu featured the result most consistent with effective collimation of energetic ions, with the exception of the slightly greater fractional energy loss than the 2 MeV He. The 8 MeV F exhibited the least effective collimation in each case.

A comparison between He at 2 MeV and at 4 MeV shows that all four parameters listed in Table 8.1 are more favourable for the higher energy ions. The greater potential for mask penetration is offset by the reduced scattering cross sections in the case where the mask thickness is made twice the range of the ions.

8.4.3 Angular Resolution

From the angular distribution data in Figure 8.1 (a, b and c)(i), it is evident that the great majority of ions are transmitted along the axis of the beam. A log scale is used to show the tailing. 91 % of He and F ions, and 96 % of Cu ions will emerge within ± 2˚ (the values in column *T* of Table 8.1 specify the fraction with no deflection at all). The angular range containing 99 % of transmitted ions is ± 14˚, ± 22˚, and ± 9˚ for He, F, and Cu respectively. While the distributions are very similar to each other, scattering of 8 MeV F in the mask results in the greatest distribution of exit angles and so is once again the least effectively collimated.

8.4.4 Energy Resolution

The energy distributions show the mean energy per transmitted ion as a function of position. The average ion energy for those transmitted in the beam spot is lower than the beam energy due to the effect of ions scattered *into* the spot with reduced energy. For multiple ion applications, this will influence the control of the total dose deposited into the target.

The conspicuous features of the energy distributions are the few high energy counts far from the aperture. These are single ion strikes following large angle scattering in the mask. While these are the counts that contribute the greatest deviations from the intended location of the ions, they are extremely rare events. Of the 10^7 incident 2 MeV He ions, there are 79 beyond the tailing region at four aperture radii with E > 100 keV; compared to 111,481 within the aperture radius, i.e. only 0.07 % of the transmitted ions. The energy tailing is more pronounced for the He, than for F and Cu which are comparable, although the single ion strikes are more significant for the high energy Cu.

8.4.5 Aperture Size Considerations

The influence of scattering on effectiveness of collimation using apertures is expected to worsen for smaller apertures. To test this, a 40 nm aperture is compared to a 100 nm aperture for collimation of 2 MeV He ions. The results are plotted in Figure 8.2.

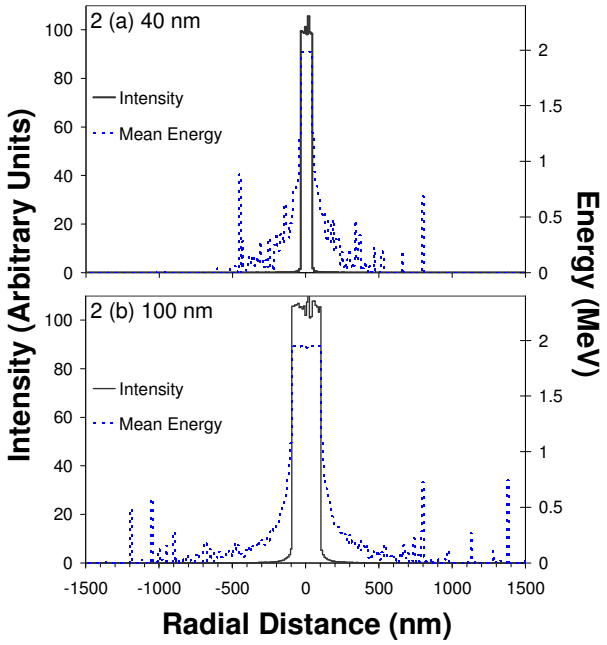

Figure 8.2 Transmission of 2 MeV He ions through (a) 40nm and (b) 100nm radii nano-apertures

The spatial resolution remains excellent, and the energy spread is comparable in the two models, although slightly wider for the larger aperture, this represents a substantially wider spread relative to the aperture size. The single ion scattering effect is somewhat more pronounced for smaller apertures, with individual ion variations being more conspicuous within the tailing continuum. Individual ion strikes of significant energy occur much farther from the aperture for the larger aperture. For the 40 nm aperture, the number of counts outside four radii and E >100 keV is 59 compared to 16,596 counts within the spot, i.e. 0.36 %. This is approximately 5 times greater than for the 100 nm case (0.07 %). However the parameters listed in Table 8.1 show that the smallest aperture is the most effective, providing the greatest probability of obtaining full energy ions within

the collimated beam spot (T = 93 %), the lowest probability of scattered ions within the spot (S_{in}= 4.8 %), and a low probability of ions outside the spot (S_{out}= 2.4 %).

8.4.6 Alignment of Beam to Aperture

Alignment of the beam with the aperture in the mask is critical to its performance as a collimator. It is expected to be difficult to achieve perfect alignment experimentally due to the high aspect ratio of the apertures. The proposed technique involves 'rocking' the sample within the beam until the energy of the transmitted signal is a maximum. Ions which transit a small portion of the mask before or after passing through the aperture (see path A in Figure 8.3) will have reduced energy. Ions which enter the aperture at an angle to the normal and scatter (path B in Figure 8.3) are expected to undergo more significant energy loss.

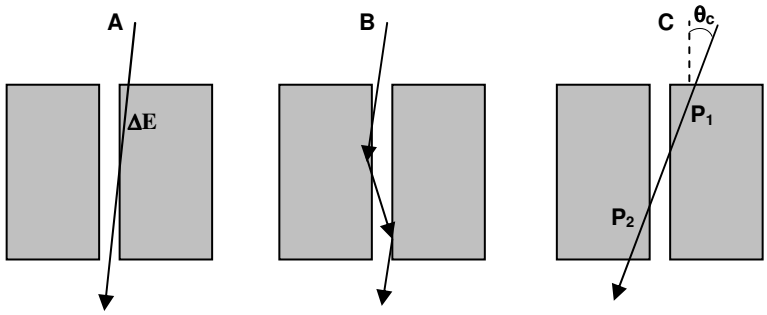

Figure 8.3 Transmission of ions through an aperture for a misaligned beam, showing (A) ions with reduced energy due to electronic energy loss traversing the mask material, (B) scattered transmitted ions, and (C) the mask closure angle, θ_c, at which the path length through the material (P_1+P_2) equals the ion range.

Figure 8.4 illustrates the transmission distribution for 2 MeV He at three different incident angles. The mask 'closure angle', θ_c, is chosen as a characteristic angle of the system. This is the angle at which the path length through the mask at the edges of the aperture becomes equal to the ion range (see Path C in Figure 8.3). Plots corresponding to ions of normal incidence and half θ_c are also presented. The range of 2 MeV He in Si is estimated to be 7.27 μm (calculated using SRIM 2006 [30]). As the mask is intended to be twice the range thickness, it has been modelled as 15 μm thick. The closure angle for this system is approximately 1.5˚.

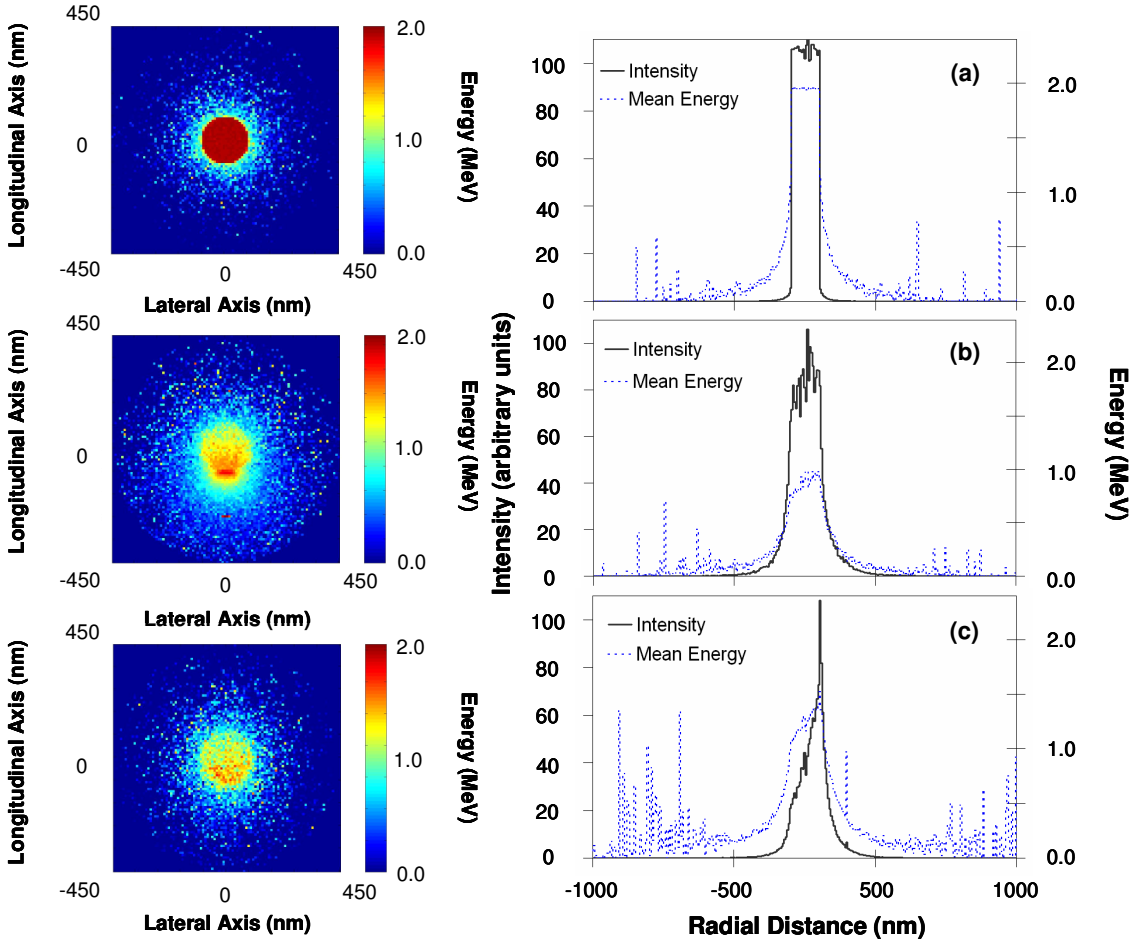

Figure 8.4 Transmission of 2 MeV He ions through a nano-aperture of 100nm radius at 3 incident angles (a) normal (b) $\theta_c/2$ and (c) θ_c (see text).

Notice that the mean transmitted ion energy is lower in and around the spot for the half-closure angle, $\theta_c/2$, than for the full closure angle, θ_c. In the half closed case, there will be a significant contribution from directly transmitted ions that have penetrated a thickness of Si shorter than their range, and have suffered the corresponding energy loss. In the closed case, no ions will be directly transmitted. All transmitted ions must have had a scattered path that incorporates a substantial passage through the void of the aperture. The scattering will reduce the ion energy but the aperture passage will be free of electronic stopping. The resulting transmission energy spectrum is not reduced in the spatial averaging by a large number of low energy directly transmitted ions, as occurs in the half closed case.

The simulations in Figure 8.4 show the skewing of the transmission spot, and the broadening of the scattered distributions illustrates the importance of the alignment between the beam and aperture axis. The reduction of the peak energy at greater angles verifies the experimental alignment technique of tilting the sample until the energy peak is a maximum.

The above results provide confidence that collimation of ion beams using small high aspect ratio apertures will be very effective for the aperture sizes considered in this simulation study. The resolution is not likely to be prohibitively restricted by scattering induced spread.

8.5 Experimental Trial

A preliminary experimental trial was conducted by Taylor et al. [126] to validate the use of a nano-aperture for beam collimation, and results compared with simulations similar to those described above. The experimental apparatus and procedure is described in detail in [126], and is briefly summarised here.

Apertures were machined in a 10 μm thick Si AFM cantilever using a focused ion beam of keV Ga ions. The mask was positioned over a polymethyl methacrylate (PMMA) coated PIN photodiode

acting as an active substrate detector for ion counting and energy response via ion beam induced current (IBIC) measurements during irradiation. The PMMA coating allows AFM imaging of the surface after etching to examine the extent of lateral spread of the ions. The apertures were irradiated with a 1 μm beam spot of He at 1.5 MeV to ensure that the mask thickness of 10 μm was approximately twice the ion range, which is 5.26 μm for 1.5 MeV He in Si.

SEM images of the apertures (see Figure 8.5) showed them to be conical with diameters of approximately 1.2 μm at the irradiated surface tapering to approximately 200 nm. The two apertures labelled (i) and (ii) in Figure 8.5 are considered here. The energy spectrum of transmitted ions is shown in Figure 8.6 together with intensity plots for five energy sub-regions. Region (e) shows that the full energy peak is partially associated with transmission through the apertures and partly with background. The latter are ions that pass outside the cantilever edges, as the detector is much broader than the cantilever, and are recorded at all positions of the mask. Slit scattered ions also contribute to the background in region (b). Regions (c) and (d) show that more high energy ions were transmitted through the upper aperture than the lower aperture.

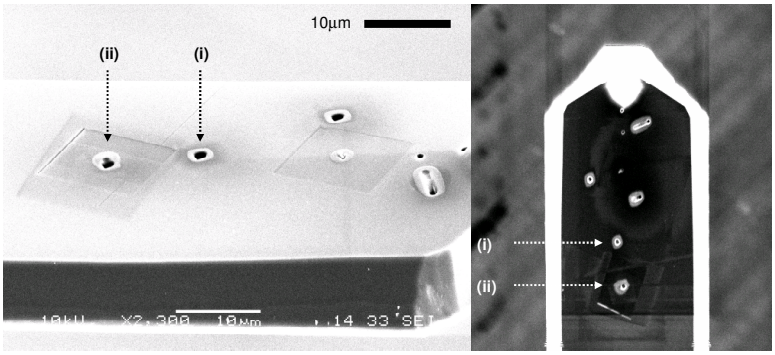

Figure 8.5 SEM images of upper and lower surfaces of the FIB drilled cantilever indicating apertures (i) and (ii).

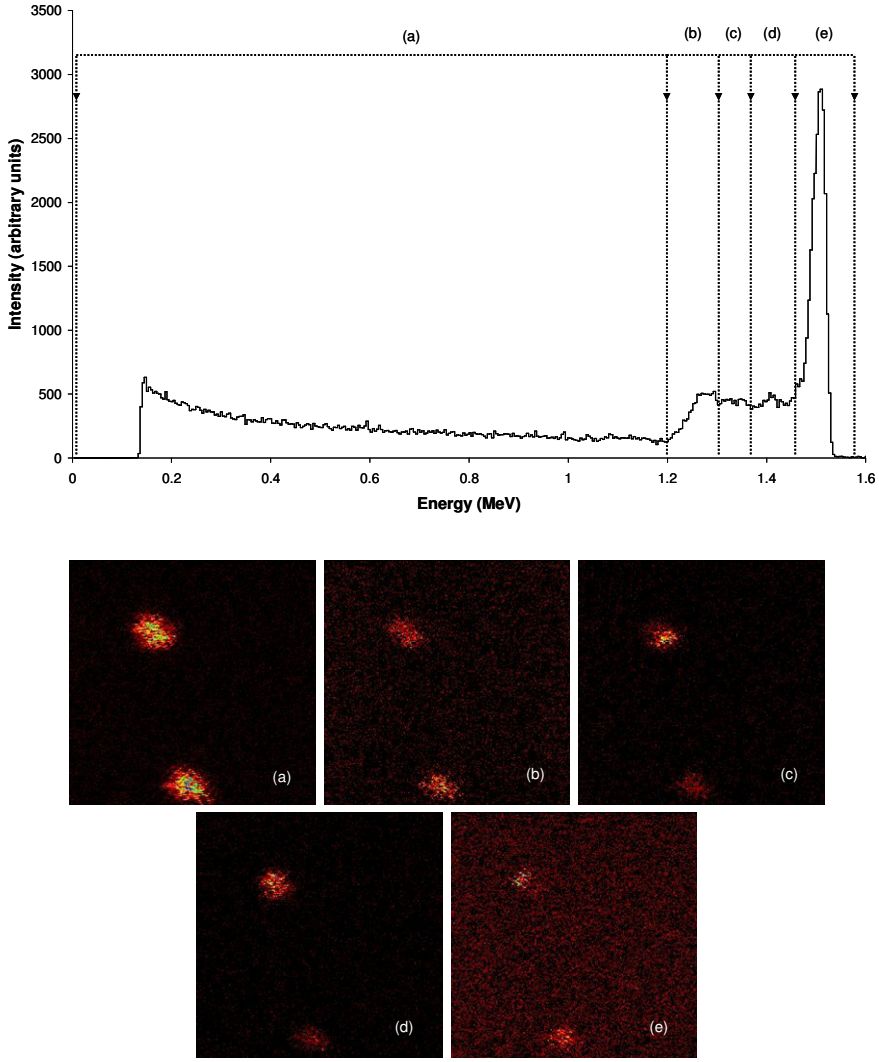

Figure 8.6 Energy spectrum (top) of transmitted ions for the two apertures labelled in Figure 8.5, and intensity maps (bottom) for the five energy sub-ranges (a)-(e) shown.

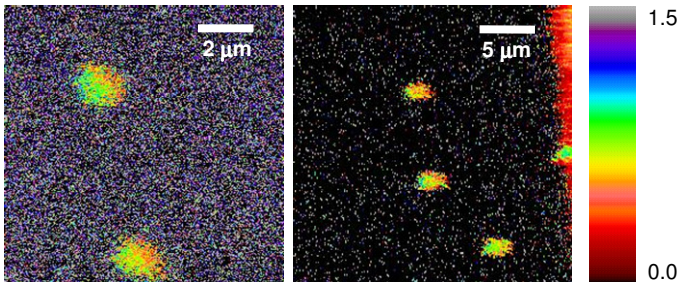

Figure 8.7 Mean energy of transmitted ions for the two apertures labelled in Figure 8.5 (left) and an alternative three aperture group (right). The colour palette is energy in MeV.

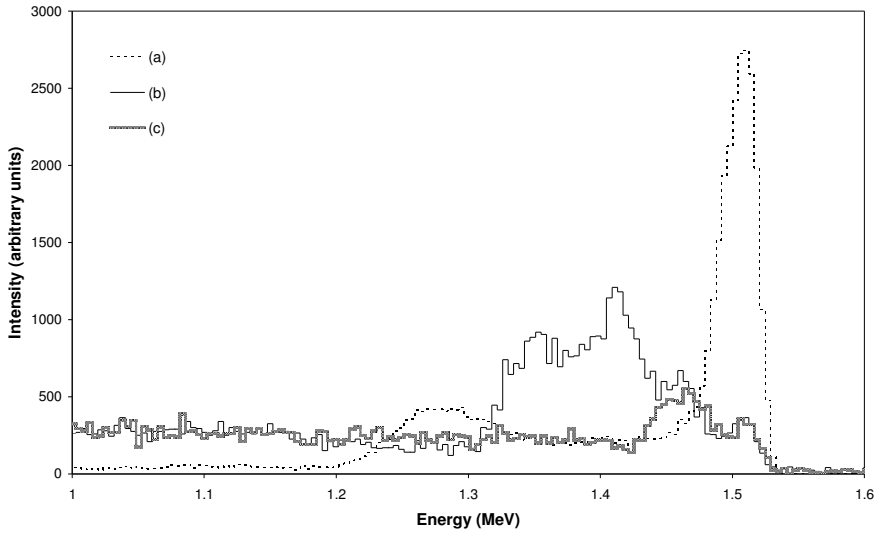

Figure 8.8 Energy spectrum of transmitted ions for the two apertures labelled in Figure 8.5: (a) is background, (b) is the upper hole of Figure 8.7, and (c) is the lower.

The mean energy of transmitted ions is shown in Figure 8.7. Individual spectra for geographical sub-regions are shown in Figure 8.8, corresponding to the two collimated beam spot regions and the remaining background.

The mean energy plot in Figure 8.7 displays the skewness predicted by the MC simulation for misaligned apertures as shown in Figure 8.4. This indicates that the apertures were not correctly

aligned with the beam during irradiation. Later AFM imaging of the PMMA surface after etching showed the exposed spots to be triangular [126] indicating that the apertures were probably not drilled normal to the surface of the Si cantilever.

The intensity plots of Figure 8.6 show that a larger number of ions were transmitted through the upper hole than the lower. There are more counts in energy windows (c) and (d), and similar numbers in the other windows. This can also be seen as the net integral across the spectrum in the individual spectra of Figure 8.8. This intensity difference shows that the upper hole is better aligned than the lower hole. The individual spot spectra shown in Figure 8.8 show that the mean energy of transmitted ions within the spot is somewhat below the incident ion energy due to scattered ions, as predicted in the simulations. Of particular interest, Figure 8.8 also shows that the ions transmitted through the lower, poorer aligned hole are distributed around a higher mean energy than those of the upper, better aligned hole. This is also accurately predicted by the simulation. As discussed in section 8.4.6 above, this is because at angles in the order of the closure angle, transmitted ions must have been scattered with a significant portion of their path lying within the aperture void.

8.6 Conclusion

Monte Carlo simulation has been used to examine the feasibility of using nano-scale apertures in Si cantilevers to collimate MeV ions for applications requiring small beam spot resolution. Intensity, energy, and angular distributions were calculated to quantify the degree to which scattering within the mask would limit the spatial resolution achievable.

The distributions for several ion-energy combinations were shown to be very similar, suggesting that systems may be scaleable for appropriate choices of ion, energy, aperture size and mask thickness. The intensity, energy and angular distributions show that the masking process works well – it is the diameter of the nano-aperture that determines the resolution obtainable. The steep

intensity gradients at the aperture edge coupled with sharp energy reduction are the desired features for applications such as ion beam lithography. Exploitation of these characteristics enables tailoring of lithographic processes where there exists a threshold damage density below which etching does not occur.

Single ion applications would benefit from a high probability of obtaining a full energy ion within the desired location, and low probability of a scattered ion with low energy or undesired location. High energy ion transmissions more than a few aperture radii from the spot are extremely rare. Heavier ions at higher energies exhibited more effective collimation for a given aperture size. However, there is still a probability in the order of 10 % of a transmitted ion not being correctly collimated.

For He ions, the probability of obtaining full energy ions within the spot increases for smaller apertures, and can also be improved by using a higher incident energy. The lower absolute energy of transmitted He ions scattered outside the aperture allows the lithographic etching process to be more easily tailored to be insensitive to the energy deposited by them. For the ion beam lithography work of Alves and co-workers, the imperfect collimation probability of 10 % for heavy ions is unacceptable. The sharper edge of the energy deposition profile together with greater dose differential achievable with larger numbers of light ions, makes this option more attractive. Based upon the results of this simulation study, Alves is pursuing the use of nano-aperture collimated He ion beams in preference to single high energy heavy ions.

Key qualitative predictions of the simulation have been confirmed in preliminary measurements including evidence of misalignment of the aperture with the beam in the trial measurements. Future work will employ the sample rocking technique, or the beam rocking technique described in [128-130] for beam-aperture alignment.

Chapter 9

Conclusion

The aim of this work was to investigate the effects of large angle scattering in Heavy Ion Elastic Recoil Detection Analysis, and in collimation of ion beams using a nano-aperture mask. Large angle plural scattering was shown to be a significant problem in the analysis of HIERDA spectra. The effects are generally more pronounced than in other IBA techniques due to the high scattering cross sections associated with heavy ions. As a consequence, the output data are difficult to interpret. The use of nano-scale apertures for collimating ion beams to very small spot sizes, is of contemporary interest to ion beam users, in the fields of materials analysis, materials modification and device construction. Ion scattering in the nano-aperture mask plays a major role in the effectiveness of the mask, ultimately limiting the resolution obtainable for a given aperture. This work has provided insights into these processes, and described techniques for quantifying their contributions to experimental results.

Monte Carlo ion transport simulation has been shown to be a useful tool for studying systems in which individual events are significant, and the events are governed by stochastic processes. Large angle scattering of energetic ions in matter is such a problem. A Monte Carlo ion transport simulation code has been adapted to the two problems described above in order to: (i) study and quantify the effects observed in experimental HIERDA results, and (ii) to aid in the experimental design of nano-aperture masking systems and guide the research direction regarding the choice of ion beam system used.

The Monte Carlo simulation was shown to satisfactorily reproduce the fundamental spectral shape of the measured spectra for several samples analysed by HIERDA. Features that can be attributed to multiple and plural scattering are very well reproduced. Some discrepancies exist relating to the deficiency of existing heavy ion stopping data, but these can be satisfactorily compensated for in the simulation process. Thus the simulation can be considered a valid method of studying these effects, in a way that cannot be achieved by conventional analytical techniques.

The computational cost associated with Monte Carlo simulation of the extremely large number of interactions involved in these problems is enormous. Several efficiency enhancement strategies have been developed and described which have enabled the simulation times to be reduced by two to three orders of magnitude for the systems studied here. The reduction in processing time exhibits a strong dependence on the beam–sample system modelled.

Using the Monte Carlo code, it has been shown that the contribution of plural scattering to output spectra can be identified and sub-divided on the basis of the number and magnitude of the scattering events occurring in the individual ion histories. This requires a user defined parameter to distinguish ‘large angle scattering’ from ‘small angle scattering’ which is somewhat arbitrary given that there is no sharp distinction between the two concepts. The complex features in the HIERDA spectra have been shown to be the result of large angle plural scattering, and that if not properly accounted for may lead to inaccurate interpretation of results.

The simulation has been applied to the interpretation of experimental data suffering from mass-overlapped signals. This is an important problem which has been identified by several authors in published work. It has been shown that the individual elemental spectra can be unambiguously separated in the simulated output, which can in turn be directly compared to the un-separated experimental data for interpretation.

The effectiveness of nano-aperture collimation was studied for a variety of ion-energy combinations. Intensity, energy, and angular distributions of transmitted ions were calculated to quantify the degree to which scattering within the mask limits the spatial resolution achievable. Aperture size and ion energy effects were also considered. The simulation was used to predict the effect of misaligning the aperture and the beam, and the result has subsequently been observed experimentally.

Transmitted ion distributions showed that while the higher energy heavier ions studied are more effectively collimated than lower energy lighter ions, there is still a significant probability of transmission of heavy ions with substantial residual energy, beyond the perimeter of the aperture. For the intended application, ion beam lithography, these ions may be problematic if the local dose surrounding the single ion track exceeds the clearing dose for the resist. The etching process can be tailored to be insensitive to the lower energy deposition rate of the He ions. The results indicate that medium energy He ions are the more attractive option, as the residual energy of scattered transmitted ions can be more readily managed by customising the etching process. Continuing research in this area is proceeding in this direction as a result of the conclusions from this work.

9.1 Future Considerations

The future application of Monte Carlo simulation to investigations of heavy ion scattering problems continues to be limited in part by the deficiencies in the current collections of measured heavy ion stopping powers. Large discrepancies exist between stopping powers estimated using various predictors and those observed experimentally. Significantly more study is required in these areas to reduce the uncertainty associated with the parameters which must be incorporated into MC simulation codes. The suitability of the ZBL universal interatomic potential [17] to describe high energy heavy ion scattering in HIERDA is yet to be fully tested. An alternative potential function, applicable to a more limited range of conditions relevant to applications such as HIERDA, may be more appropriate.

The application of MC simulation to routine interpretation of experimental data is an obvious future goal. To be practical, simulation times must be reduced to something approaching the experimental measurement times – perhaps in the order of 15 minutes. This will require evolutionary increases in computing power, combined with further efficiency enhancement techniques. The latter will likely involve excluding very low probability, highly convoluted plural scatter paths which have been included in this work but whose contributions to sample analysis could be safely neglected. An example is the strategy of forcing scattering events to be in the direction of the detector, and this is the basis of the MCERD simulation code of Arstila [8].

The ion beam lithography work of Alves [116] is continuing, with attention being focused on the use of He ion beams rather than single heavy ions, as a direct result of findings of the simulation work discussed in this thesis. Future simulation development will incorporate a more realistic conical shape for the apertures modelled in recognition of the tapered walls typical of nano-scale holes machined by focused in beam drilling.

References

1. Walker, S.R., Johnston, P.N., Bubb, I.F., Stannard, W.B., Cohen, D.D., Dytlewski, N., Hult, M., Whitlow, H.J., Zaring, C., and Ostling et, a., *Mass and Energy Dispersive Recoil Spectrometry of Mocvd Grown Alxga1-Xas.* Nuclear Instruments & Methods in Physics Research, Section A (Accelerators, Spectrometers, Detectors and Associated Equipment), 1994. **353**(1-3): p. 563-567.
2. Hult, M., Bouanani, M.E., Persson, L., Whitlow, H.J., Andersson, M., Zaring, C., Ostling, M., Cohen, D.D., Dytlewski, N., Bubb, I.F., Johnston, P.N., and Walker, S.R., *Empirical Characterisation of Mass Distribution Broadening in Tof-E Recoil Spectrometry.* Nuclear Instruments and Methods in Physics Research Section B: Beam Interactions with Materials and Atoms, 1995. **101**(3): p. 263-266.
3. Stannard, W.B., Johnston, P.N., Walker, S.R., Bubb, I.F., Scott, J.F., Cohen, D.D., Dytlewski, N., and Martin, J.W., *Heavy Ion Recoil Spectrometry of Barium Strontium Titanate Films.* Nuclear Instruments & Methods in Physics Research, Section B (Beam Interactions with Materials and Atoms), 1995. **B99**(1-4): p. 447-449.
4. Stannard, W.B., Johnston, P.N., Walker, S.R., Bubb, I.F., Scott, J.F., Cohen, D.D., Dytlewski, N., and Martin, J.W., *Stoichiometric Analysis of a Barium Strontium Titanate Film by Heavy Ion Recoil Spectrometry.* Integrated Ferroelectrics, 1995. **9**(1-3): p. 243-250.
5. Stannard, W.B., Doctoral Thesis, Royal Melbourne Institute of Technology (RMIT), Melbourne, Australia, 2000
6. Tesmer, J.R. and Nastasi, M.A., eds. *Handbook of Modern Ion Beam Materials Analysis.* 1995, Materials Research Society.
7. Davies, J.A., Lennard, W.N., and Mitchell, I.V., *Ch 12. Pitfalls in Ion Beam Analysis*, in *Handbook of Modern Ion Beam Materials Analysis.*, J.R. Tesmer and Nastasi, M.A., Editors. 1995, Materials Research Society.

8. Arstila, K., Sajavaara, T., and Keinonen, J., *Monte Carlo Simulation of Multiple and Plural Scattering in Elastic Recoil Detection.* Nuclear Instruments and Methods in Physics Research Section B: Beam Interactions with Materials and Atoms, 2001. **174**(1-2): p. 163-172.

9. Arstila, K., Knapp, J.A., Nordlund, K., and Doyle, B.L., *Monte Carlo Simulations of Multiple Scattering Effects in Erd Measurements.* Nuclear Instruments and Methods in Physics Research Section B: Beam Interactions with Materials and Atoms, 2004. **219-220**: p. 1058-1061.

10. Barbour, J.C. and Doyle, B.L., *Ch 5. Elastic Recoil Detection.*, in *Handbook of Modern Ion Beam Materials Analysis.*, J.R. Tesmer and Nastasi, M.A., Editors. 1995, Materials Research Society.

11. Assmann, W., Davies, J.A., Dollinger, G., Forster, J.S., Huber, H., Reichelt, T., and Siegele, R., *Erda with Very Heavy Ion Beams.* Nuclear Instruments and Methods in Physics Research Section B: Beam Interactions with Materials and Atoms, 1996. **118**(1-4): p. 242-250.

12. Forster, J.S., Currie, P.J., Davies, J.A., Siegele, R., Wallace, S.G., and Zelenitsky, D., *Elastic Recoil Detection (Erd) with Extremely Heavy Ions.* Nuclear Instruments and Methods in Physics Research Section B: Beam Interactions with Materials and Atoms, 1996. **113**(1-4): p. 308-311.

13. Davies, J.A., Forster, J.S., and Walker, S.R., *High-Energy Heavy Ion Beams in Materials Science.* Nuclear Instruments and Methods in Physics Research Section B: Beam Interactions with Materials and Atoms, 1998. **139**(1-4): p. 120-127.

14. L'Ecuyer, J., Brassard, C., Cardinal, C., Chabbal, J., Deschenes, L., Labrie, J.P., Terreault, B., Martel, J.G., and St.-Jacques, R., *An Accurate and Sensitive Method for the Determination of the Depth Distribution of Light Elements in Heavy Materials.* Journal of Applied Physics, 1976. **47**(1): p. 381-382.

15. Pascual-Izarra, C. and Garcia, G., *An Efficient Method for Stopping Force Determination.* Nuclear Instruments and Methods in Physics Research Section B: Beam Interactions with Materials and Atoms, 2004. **225**(3): p. 383-391.

16. Weijers, T.D.M., Duck, B.C., and O'Connor, D.J., *The Development of a Stopping Power Predictor for Ions with Energies of 0.1-1.0 Mev/U in Elemental Targets.* Nuclear Instruments and Methods in Physics Research Section B: Beam Interactions with Materials and Atoms, 2004. **215**(1-2): p. 35-47.

17. Ziegler, J.F., Biersack, J.P., and Littmark, U., *Stopping and Range of Ions in Solids.* Stopping and Range of Ions in Matter. Vol. 1. 1985: Pergamon Press.

18. Rauhala, E., *Ch 2. Energy Loss*, in *Handbook of Modern Ion Beam Materials Analysis.*, J.R. Tesmer and Nastasi, M.A., Editors. 1995, Materials Research Society.

19. Ziegler, J.F., *Handbook of Stopping Cross-Sections for Energetic Ions in All Elements.* 1980: Pergamon Press.

20. Chu, W.K., Mayer, J.W., and Nicolet, M.A., *Backscattering Spectrometry.* 1978: Academic Press Inc.

21. Zhang, Y., *High-Precision Measurement of Electronic Stopping Powers for Heavy Ions Using High-Resolution Time-of-Flight Spectrometry.* Nuclear Instruments and Methods in Physics Research Section B: Beam Interactions with Materials and Atoms, 2002. **196**(1-2): p. 1-15.

22. Zhang, Y. and Weber, W.J., *Studies of Electronic Stopping Powers Using Time of Flight Spectrometry.* Nuclear Instruments and Methods in Physics Research Section B: Beam Interactions with Materials and Atoms, 2004. **219-220**: p. 256-262.

23. Arstila, K., *An Experimental Method for Precise Determination of Electronic Stopping Powers for Heavy Ions.* Nuclear Instruments and Methods in Physics Research Section B: Beam Interactions with Materials and Atoms, 2000. **168**(4): p. 473-483.

24. Paul, H., *Http://Www.Exphys.Uni-Linz.Ac.At/Stopping/*. 2007.

25. Ziegler, J.F., *Http://Www.Srim.Org/Srim/Srimpics/Stopplots.Htm*. 2006.

26. Paul, H. and Schinner, A., *An Empirical Approach to the Stopping Power of Solids and Gases for Ions from 3li to 18ar.* Nuclear Instruments and Methods in Physics Research Section B: Beam Interactions with Materials and Atoms, 2001. **179**(3): p. 299-315.

27. Paul, H. and Schinner, A., *An Empirical Approach to the Stopping Power of Solids and Gases for Ions from 3li to 18ar - Part Ii.* Nuclear Instruments and Methods in Physics Research Section B: Beam Interactions with Materials and Atoms, 2002. **195**(1-2): p. 166-174.

28. Sigmund, P., *Stopping Power in Perspective.* Nuclear Instruments and Methods in Physics Research Section B: Beam Interactions with Materials and Atoms, 1998. **135**(1-4): p. 1-15.

29. Paul, H. and Schinner, A., *Judging the Reliability of Stopping Power Tables and Programs for Heavy Ions.* Nuclear Instruments and Methods in Physics Research Section B: Beam Interactions with Materials and Atoms: Fifth International Symposium on Swift Heavy Ions in Matter, 2003. **209**: p. 252-258.

30. *Srim 2006. The Stopping and Range of Ions in Matter.*, http://www.srim.org/.

31. Northcliffe, L.C. and Schilling, R.F., *Range and Stopping-Power Tables for Heavy Ions.* Atomic Data and Nuclear Data Tables, 1970. **7**(3-4): p. 233-463.

32. Timmers, H., Elliman, R.G., Palmer, G.R., Ophel, T.R., and O'Connor, D.J., *The Development of a Facility for Heavy-Ion Elastic Recoil Detection Analysis at the Australian National University.* Nuclear Instruments and Methods in Physics Research Section B: Beam Interactions with Materials and Atoms, 1998. **136-138**: p. 611-615.

33. Elliman, R.G., Timmers, H., Palmer, G.R., and Ophel, T.R., *Limitations to Depth Resolution in High-Energy, Heavy-Ion Elastic Recoil Detection Analysis.* Nuclear Instruments and Methods in Physics Research Section B: Beam Interactions with Materials and Atoms, 1998. **136-138**: p. 649-653.

34. Besenbacher, F., Andersen, J.U., and Bonderup, E., *Straggling in Energy Loss of Energetic Hydrogen and Helium Ions.* Nuclear Instruments and Methods, 1980. **168**(1-3): p. 1-15.

35. Whitlow, H.J., Possnert, G., and Petersson, C.S., *Quantitative Mass and Energy Dispersive Elastic Recoil Spectrometry: Resolution and Efficiency Considerations.* Nuclear

Instruments and Methods in Physics Research Section B: Beam Interactions with Materials and Atoms, 1987. **27**(3): p. 448-457.

36. Thomas, J.P., Fallavier, M., Ramdane, D., Chevarier, N., and Chevarier, A., *High Resolution Depth Profiling of Light Elements in High Atomic Mass Materials.* Nuclear Instruments and Methods in Physics Research, 1983. **218**(1-3): p. 125-128.

37. Grigull, S., Kreissig, U., Huber, H., and Assmann, W., *Element-Dependent Erda Probing Depths Using Different Detection Systems.* Nuclear Instruments and Methods in Physics Research Section B: Beam Interactions with Materials and Atoms, 1997. **132**(4): p. 709-717.

38. Schiettekatte, F., Chicoine, M., Forster, J.S., Geiger, J.S., Gujrathi, S., Kolarova, R., Paradis, A., Roorda, S., and Wei, P., *Erd, 15n External Beam for Nrra in Air, Hirbs: Ion Beam Analysis Developments on the Hvec En-1 Tandem.* Nuclear Instruments and Methods in Physics Research Section B: Beam Interactions with Materials and Atoms, Proceedings of the Sixteenth International Conference on Ion Beam Analysis, 2004. **219-220**: p. 430-434.

39. Siegele, R., Haugen, H.K., Davies, J.A., Forster, J.S., and Andrews, H.R., *Forward Elastic Recoil Measurements Using Heavy Ions.* Journal of Applied Physics, 1994. **76**(8): p. 4524-4532.

40. Climent Font, A., Banks, J.C., and Doyle, B.L., *Quantitative Analysis with Heavy Ion E-Tof-Erd.* Nuclear Instruments and Methods in Physics Research Section B: Beam Interactions with Materials and Atoms, 2000. **161-163**: p. 255-259.

41. Arai, E., Funaki, H., Katayama, M., Oguri, Y., and Shimizu, K., *Tof Erd Experiments Using a 10 Mev 35cl Beam.* Nuclear Instruments and Methods in Physics Research Section B: Beam Interactions with Materials and Atoms, 1992. **64**(1-4): p. 296-300.

42. Razpet, A., Pelicon, P., Rupnik, Z., and Budnar, M., *Development of a Time-of-Flight Telescope for Erda at the Jozef Stefan Institute.* Nuclear Instruments and Methods in Physics Research Section B: Beam Interactions with Materials and Atoms, 2003. **201**(3): p. 535-542.

43. Mathot, G. and Terwagne, G., *The Development of a Time of Flight Spectrometer for Larn.* Nuclear Instruments and Methods in Physics Research Section B: Beam Interactions with Materials and Atoms, 2002. **190**(1-4): p. 190-194.

44. Martin, J.W., Cohen, D.D., Dytlewski, N., Garton, D.B., Whitlow, H.J., and Russell, G.J., *Materials Characterisation Using Heavy Ion Elastic Recoil Time of Flight Spectrometry.* Nuclear Instruments and Methods in Physics Research Section B: Beam Interactions with Materials and Atoms, 1994. **94**(3): p. 277-290.

45. Johnston, P.N., El Bouanani, M., Stannard, W.B., Bubb, I.F., Cohen, D.D., Dytlewski, N., and Siegele, R., *Complementary Scattered and Recoiled Ion Data from Tof-E Heavy Ion Elastic Recoil Detection Analysis.* Nuclear Instruments and Methods in Physics Research Section B: Beam Interactions with Materials and Atoms, 1998. **136-138**: p. 669-673.

46. Bohne, W., Rohrich, J., Schopke, A., Selle, B., Sieber, I., Fuhs, W., del Prado, A., San Andres, E., Martil, I., and Gonzalez-Diaz, G., *Compositional Analysis of Thin Sioxny:H Films by Heavy-Ion Erda, Standard Rbs, Edx and Aes: A Comparison.* Nuclear Instruments and Methods in Physics Research Section B: Beam Interactions with Materials and Atoms, 2004. **217**(2): p. 237-245.

47. Hult, M., Whitlow, H.J., and Ostling, M., *High-Resolution Recoil Spectrometry for Separate Characterization of Ga and as in Al[Sub X]Ga[Sub (1 - X)]as Structures.* Applied Physics Letters, 1992. **60**(2): p. 219-221.

48. Johnston, P.N., El Bouanani, M., Stannard, W.B., Bubb, I.F., Cohen, D.D., Siegele, R., and Dytlewski, N., *Si Detector Pulse Height Shift and Multiple Scattering Problems in Heavy Ion Elastic Recoil Detection Analysis.* Vacuum, 1997. **48**(12): p. 1017-1021.

49. Assmann, W., Hartung, P., Huber, H., Staat, P., Steffens, H., and Steinhausen, C., *Setup for Materials Analysis with Heavy Ion Beams at the Munich Mp Tandem.* Nuclear Instruments and Methods in Physics Research Section B: Beam Interactions with Materials and Atoms, 1994. **85**(1-4): p. 726-731.

50. Johnston, P.N., El Bouanani, M., Stannard, W.B., Bubb, I.F., Jonsson, P., Zhang, Y., and Whitlow, H.J., *Simulation of Two Dimensional Time of Flight and Energy Recoil*

Spectrometry Data. Applications Of Accelerators In Research And Industry, AIP Conference Proceedings, 1997. **392**(1): p. 715-718.

51. Timmers, H., Weijers, T.D.M., and Elliman, R.G., *Unique Capabilities of Heavy Ion Elastic Recoil Detection with Gas Ionization Detectors.* Nuclear Instruments and Methods in Physics Research Section B: Beam Interactions with Materials and Atoms, 2002. **190**(1-4): p. 393-396.

52. Persson, L., Whitlow, H.J., Bouanani, M.E., Hult, M., Andersson, M., Bubb, I.F., Cohen, D.D., Dytlewski, N., Johnston, P.N., and Walker, S.R., *Separation of Mass-Overlapped Time of Flight-Energy Elastic Recoil Detection Analysis Data Using Ryan and Jamieson's Dynamic Analysis Method.* Nuclear Instruments and Methods in Physics Research Section B: Beam Interactions with Materials and Atoms, 2001. **179**(3): p. 403-411.

53. Doyle, B.L. and Peercy, P.S., *Technique for Profiling [Sup 1]H with 2.5-Mev Van De Graaff Accelerators.* Applied Physics Letters, 1979. **34**(11): p. 811-813.

54. Davies, J.A., Forster, J.S., and Walker, S.R., *Elastic Recoil Detection Analysis with Heavy Ion Beams.* Nuclear Instruments and Methods in Physics Research Section B: Beam Interactions with Materials and Atoms, 1998. **136-138**: p. 594-602.

55. Bohne, W., Fuhs, W., Röhrich, J., Selle, B., Sieber, I., del Prado, A., San Andrés, E., Mártil, I., and González-Díaz, G., *Compositional Analysis of Sio_xn_y:H Films by Heavy-Ion Erda: The Problem of Radiation Damage.* Surface and Interface Analysis, 2002. **34**(1): p. 749-753.

56. Walker, S.R., Davies, J.A., Forster, J.S., Wallace, S.G., and Kockelkoren, A.C., *Radiation Damage During Heavy Ion Elastic Recoil Detection Analysis of Insulating Materials.* Nuclear Instruments and Methods in Physics Research Section B: Beam Interactions with Materials and Atoms, 1998. **136-138**: p. 707-712.

57. Shrestha, S.K. and Timmers, H., *The Optimum Heavy Ion Beam for the Compositional Analysis of Indium Nitride Films.* Nuclear Instruments and Methods in Physics Research Section B: Beam Interactions with Materials and Atoms, 2006. **249**(1-2): p. 257-260.

58. Doolittle, L.R., *Algorithms for the Rapid Simulation of Rutherford Backscattering Spectra.* Nuclear Instruments and Methods in Physics Research Section B: Beam Interactions with Materials and Atoms, 1985. **9**(3): p. 344-351.

59. Szilagyi, E. and Paszti, F., *Theoretical Calculation of the Depth Resolution of Iba Methods.* Nuclear Instruments and Methods in Physics Research Section B: Beam Interactions with Materials and Atoms, 1994. **85**(1-4): p. 616-620.

60. Szilagyi, E., Paszti, F., and Amsel, G., *Theoretical Approximations for Depth Resolution Calculations in Iba Methods.* Nuclear Instruments and Methods in Physics Research Section B: Beam Interactions with Materials and Atoms, 1995. **100**(1): p. 103-121.

61. Mayer, M., *Simnra User's Guide.*, in *Technical Report IPP 9/113*. 1997, Max-Planck-Institut fur Plasmaphysik: Garching, Germany.

62. Kotai, E., *Computer Methods for Analysis and Simulation of Rbs and Erda Spectra.* Nuclear Instruments and Methods in Physics Research Section B: Beam Interactions with Materials and Atoms, 1994. **85**(1-4): p. 588-596.

63. Jeynes, C., Barradas, N.P., Marriott, P.K., Boudreault, G., Jenkin, M., Wendler, E., and Webb, R.P., *Elemental Thin Film Depth Profiles by Ion Beam Analysis Using Simulated Annealing - a New Tool.* Journal of Physics D: Applied Physics, 2003. **36**(7): p. R97-R126.

64. Rauhala, E., Barradas, N.P., Fazinic, S., Mayer, M., Szilagyi, E., and Thompson, M., *Status of Ion Beam Data Analysis and Simulation Software.* Nuclear Instruments and Methods in Physics Research Section B: Beam Interactions with Materials and Atoms, 2006. **244**(2): p. 436-456.

65. Sigmund, P. and Winterbon, K.B., *Small-Angle Multiple Scattering of Ions in the Screened Coulomb Region. I. Angular Distributions.* Nuclear Instruments and Methods, 1974. **119**(3): p. 541-557.

66. Marwick, A.D. and Sigmund, P., *Small-Angle Multiple Scattering of Ions in the Screened Coulomb Region : 2. Lateral Spread.* Nucl Instrum Methods, 1975. **126**(3): p. 317-323.

67. Amsel, G., Battistig, G., and L'Hoir, A., *Small Angle Multiple Scattering of Fast Ions, Physics, Stochastic Theory and Numerical Calculations.* Nuclear Instruments and Methods

in Physics Research Section B: Beam Interactions with Materials and Atoms, 2003. **201**(2): p. 325-388.

68. Winterbon, K.B., *Finite-Angle Multiple Scattering Revisited.* Nuclear Instruments and Methods in Physics Research Section B: Beam Interactions with Materials and Atoms, 1989. **43**(2): p. 146-148.

69. Szilagyi, E., Wielunski, L.S., and Paszti, F., *Theoretical Approximation of Energy Distribution of Elastically Recoiled Hydrogen Atoms.* Nuclear Instruments and Methods in Physics Research Section B: Beam Interactions with Materials and Atoms, 1998. **136-138**: p. 701-706.

70. Wielunski, L.S., Szilagyi, E., and Harding, G.L., *Multiple Scattering Effects in Depth Resolution of Elastic Recoil Detection.* Nuclear Instruments and Methods in Physics Research Section B: Beam Interactions with Materials and Atoms, 1998. **136-138**: p. 713-718.

71. Weber, A., Mommsen, H., Sarter, W., and Weller, A., *Double Scattering in Rutherford Backscattering Spectra.* Nuclear Instruments and Methods in Physics Research, 1982. **198**(2-3): p. 527-533.

72. Eckstein, W. and Mayer, M., *Rutherford Backscattering from Layered Structures Beyond the Single Scattering Model.* Nuclear Instruments and Methods in Physics Research Section B: Beam Interactions with Materials and Atoms, 1999. **153**(1-4): p. 337-344.

73. Barradas, N.P., *Double Scattering in Grazing Angle Rutherford Backscattering Spectra.* Nuclear Instruments and Methods in Physics Research Section B: Beam Interactions with Materials and Atoms, 2004. **225**(3): p. 318-330.

74. Repplinger, F., Stoquert, J.P., and Siffert, P., *Double Scattering in Elastic Recoil Spectra.* Nuclear Instruments and Methods in Physics Research Section B: Beam Interactions with Materials and Atoms, 1993. **80-81**(Part 1): p. 24-27.

75. Mayer, M., *Ion Beam Analysis of Rough Thin Films.* Nuclear Instruments and Methods in Physics Research Section B: Beam Interactions with Materials and Atoms, 2002. **194**(2): p. 177-186.

76. Steinbauer, E., Bauer, P., and Biersack, J., *Monte Carlo Simulation of Rbs Spectra: Comparison to Experimental and Empirical Results.* Nuclear Instruments and Methods in Physics Research Section B: Beam Interactions with Materials and Atoms, 1990. **45**(1-4): p. 171-175.

77. Biersack, J.P., Steinbauer, E., and Bauer, P., *A Particularly Fast Trim Version for Ion Backscattering and High Energy Ion Implantation.* Nuclear Instruments and Methods in Physics Research Section B: Beam Interactions with Materials and Atoms, 1991. **61**(1): p. 77-82.

78. Bauer, P., Steinbauer, E., and Biersack, J.P., *The Width of an Rbs Spectrum: Influence of Plural and Multiple Scattering.* Nuclear Instruments and Methods in Physics Research Section B: Beam Interactions with Materials and Atoms, 1992. **64**(1-4): p. 711-715.

79. Pusa, P., Ahlgren, T., and Rauhala, E., *Fast Monte Carlo Simulation for Elastic Ion Backscattering.* Nuclear Instruments and Methods in Physics Research Section B: Beam Interactions with Materials and Atoms, Proceedings of the Sixteenth International Conference on Ion Beam Analysis, 2004. **219-220**: p. 95-98.

80. Li, M.M. and O'Connor, D.J., *Simulation of Multiple Scattering Background in Heavy Ion Backscattering Spectrometry.* Nuclear Instruments and Methods in Physics Research Section B: Beam Interactions with Materials and Atoms, 1999. **149**(4): p. 460-468.

81. Tassotto, M. and Watson, P.R., *Simulation of Time-of-Flight Spectra in Direct Recoil Spectrometry for the Study of Recoil Depth Distributions and Multiple Scattering Contributions.* Surface Science, 2000. **464**(2-3): p. 251-264.

82. Johnston, P.N., Bubb, I.F., El Bouanani, M., Cohen, D.D., and Dytlewski, N., *The Effects of Multiple and Plural Scattering on Heavy Ion Elastic Recoil Detection Analysis.* Applications Of Accelerators In Research And Industry, AIP Conference Proceedings, 1999. **475**(1): p. 517-520.

83. Sajavaara, T., Arstila, K., Laakso, A., and Keinonen, J., *Effects of Surface Roughness on Results in Elastic Recoil Detection Measurements.* Nuclear Instruments and Methods in

Physics Research Section B: Beam Interactions with Materials and Atoms, 2000. **161-163**: p. 235-239.

84. Edelmann, E., Arstila, K., and Keinonen, J., *Bayesian Data Analysis for Erda Measurements.* Nuclear Instruments and Methods in Physics Research Section B: Beam Interactions with Materials and Atoms, Proceedings of the Seventh International Conference on Computer Simulation of Radiation Effects in Solids, 2005. **228**(1-4): p. 364-368.

85. Mayer, M., Arstila, K., Nordlund, K., Edelmann, E., and Keinonen, J., *Multiple Scattering of Mev Ions: Comparison between the Analytical Theory and Monte-Carlo and Molecular Dynamics Simulations.* Nuclear Instruments and Methods in Physics Research Section B: Beam Interactions with Materials and Atoms, Ion Beam Analysis - Proceedings of the Seventeenth International Conference on Ion Beam Analysis, 2006. **249**(1-2): p. 823-827.

86. Knapp, J.A., Arstila, K., Wampler, W.R., Banks, J.C., and Doyle, B.L., *Elastic Recoil Detection Analysis of 3he.* Nuclear Instruments and Methods in Physics Research Section B: Beam Interactions with Materials and Atoms, Proceedings of the Sixteenth International Conference on Ion Beam Analysis, 2004. **219-220**: p. 440-443.

87. Johnston, P.N., Franich, R.D., Bubb, I.F., El Bouanani, M., Cohen, D.D., Dytlewski, N., and Siegele, R., *The Effects of Large Angle Plural Scattering on Heavy Ion Elastic Recoil Detection Analysis.* Nuclear Instruments and Methods in Physics Research Section B: Beam Interactions with Materials and Atoms, 2000. **161-163**: p. 314-317.

88. Franich, R.D., Johnston, P.N., Bubb, I.F., Dytlewski, N., and Cohen, D.D., *Efficiency Enhancements to Monte Carlo Simulation of Heavy Ion Elastic Recoil Detection Analysis Spectra.* Nuclear Instruments and Methods in Physics Research Section B: Beam Interactions with Materials and Atoms, 2002. **190**(1-4): p. 252-255.

89. Franich, R.D., Johnston, P.N., and Bubb, I.F. *The Paths of Plurally Scattered Ions in Heavy Ion Elastic Recoil Detection Analysis*. in *Application of Accelerators in Research and Industry: 17th International Conference on the Application of Accelerators in Research and Industry*. 2003. AIP. **680**. p. 385-388

90. Johnston, P.N., Bubb, I.F., Franich, R., Cohen, D.D., Dytlewski, N., Arstila, K., and Sajavaara, T. *Scattering of Ions Beyond the Single Scattering Critical Angle in Hierda*. in *Application Of Accelerators In Research and Industry: 17th International Conference on the Application of Accelerators in Research and Industry*. 2003. AIP. **680**. p. 460-463

91. Franich, R.D., Johnston, P.N., and Bubb, I.F., *Efficient Monte Carlo Simulation of Heavy Ion Elastic Recoil Detection Analysis Spectra.* Nuclear Instruments and Methods in Physics Research Section B: Beam Interactions with Materials and Atoms, 2004. **219-220**: p. 87-94.

92. Weijers, T.D.M., Elliman, R.G., and Timmers, H., *Heavy Ion Elastic Recoil Detection Analysis of Silicon-Rich Silica Films.* Nuclear Instruments and Methods in Physics Research Section B: Beam Interactions with Materials and Atoms, Proceedings of the Sixteenth International Conference on Ion Beam Analysis, 2004. **219-220**: p. 680-685.

93. Vieira, A. and Barradas, N.P., *Neural Network Analysis of Rutherford Backscattering Data.* Nuclear Instruments and Methods in Physics Research Section B: Beam Interactions with Materials and Atoms, 2000. **170**(1-2): p. 235-238.

94. Whitlow, H.J., in *High Energy and Heavy Ion Beams in Materials Analysis*, J.R. Tesmer, Maggiore, C.J., Nastasi, M.A., Barbour, J.C., and Mayer, J.W., Editors. 1990, Materials Research Society: Pittsburgh, Pensylvania. p. 73.

95. Whitlow, H.J., Jakobsson, B., and Lars Westerberg, D., *Mass Resolution of Recoil Fragment Detector Telescopes for 0.05-0.5 a Mev Heavy Recoiling Fragments.* Nuclear Instruments and Methods in Physics Research Section A: Accelerators, Spectrometers, Detectors and Associated Equipment, 1991. **310**(3): p. 636-648.

96. Busch, F., Pfeffer, W., Kohlmeyer, B., Schull, D., and Puhlhoffer, F., *A Position-Sensitive Transmission Time Detector.* Nuclear Instruments and Methods, 1980. **171**(1): p. 71-74.

97. Sigmund, P. and Schinner, A., *Effective Charge and Related/Unrelated Quantities in Heavy-Ion Stopping.* Nuclear Instruments and Methods in Physics Research Section B: Beam Interactions with Materials and Atoms, 2001. **174**(4): p. 535-540.

98. *16th International Conference on Ion Beam Analysis*. 2003: Albuquerque, New Mexico, USA.

99. Oen, O.S. and Robinson, M.T., *The Effect of Channeling on Displacement Cascade Theory.* Applied Physics Letters, 1963. **2**(4): p. 83-85.

100. Robinson, M.T. and Oen, O.S., *The Channeling of Energetic Atoms in Crystal Lattices.* Applied Physics Letters, 1963. **2**(2): p. 30-32.

101. Oen, O.S., Holmes, D.K., and Robinson, M.T., *Ranges of Energetic Atoms in Solids.* Journal of Applied Physics, 1963. **34**(2): p. 302-312.

102. Glasko, J.M., Zou, J., Cockayne, D.J.H., FitzGerald, J., and Elliman, R.G. *The Effect of Irradiation Temperature on Post-Irradiation Strain Levels in Ge_xsi_{1-X}/Si Strained Layer Heterostructures*. in *Proceedings, 1996 Conference on Optoelectronic and Microelectronic Materials And Devices*. 1996. p. 142-145

103. Glasko, J.M., Elliman, R.G., Zou, J., Cockayne, D.J.H., and Fitz Gerald, J.D., *Strain and Defect Microstructure in Ion-Irradiated Gesi/Si Strained Layers as a Function of Annealing Temperature.* Applied Physics Letters, 1998. **73**(6): p. 838-840.

104. Fatima, S., Wong-Leung, J., Fitzgerald, J., and Jagadish, C. *Comparative Study of the Electrical and Structural Characterization of the Sub-Threshold Damage in N- and P-Type Si Implanted with Mev Ions*. in *Proceedings, 1998 Conference on Optoelectronic and Microelectronic Materials Devices*. 1998. p. 505-508

105. Zhang, Y., Whitlow, H.J., Winzell, T., Bubb, I.F., Sajavaara, T., Arstila, K., and Keinonen, J., *Detection Efficiency of Time-of-Flight Energy Elastic Recoil Detection Analysis Systems.* Nuclear Instruments and Methods in Physics Research Section B: Beam Interactions with Materials and Atoms, 1999. **149**(4): p. 477-489.

106. Zhang, Y., Whitlow, H.J., and Winzell, T., *Influence of Heavy Ion Irradiation Damage on Silicon Charged Particle Detector Calibration.* Nuclear Instruments and Methods in Physics Research Section B: Beam Interactions with Materials and Atoms, 2000. **161-163**: p. 297-301.

107. El Bouanani, M., Hult, M., Persson, L., Swietlicki, E., Andersson, M., Ostling, M., Lundberg, N., Zaring, C., Cohen, D.D., and Dytlewski et, a., *Multivariate Analysis Method for Energy Calibration and Improved Mass Assignment in Recoil Spectrometry.* Nuclear Instruments & Methods in Physics Research, Section B (Beam Interactions with Materials and Atoms), 1994. **B94**(4): p. 530-536.

108. Persson, L., El Bouanani, M., Hult, M., Jonsson, P., Whitlow, H.J., Andersson, M., Georgsson, K., Bubb, I.F., Johnston, P.N., and Walker et, a., *Recoil Spectrometry of Thin Film Reactions in the Pd/Inp System.* Journal of Vacuum Science & Technology A (Vacuum, Surfaces, and Films), 1996. **14**(4): p. 2405-2413.

109. Watt, F., Bettiol, A.A., Van Kan, J.A., Teo, E.J., and Breese, M.B.H., *Ion Beam Lithography and Nanofabrication: A Review.* International Journal of Nanoscience, 2005. **4**(3): p. 269-286.

110. Reyntjens, S. and Puers, R., *A Review of Focused Ion Beam Applications in Microsystem Technology.* Journal of Micromechanics and Microengineering, 2001. **11**(4): p. 287.

111. Bettiol, A.A., Sum, T.C., van Kan, J.A., and Watt, F., *Fabrication of Micro-Optical Components in Polymer Using Proton Beam Micro-Machining and Modification.* Nuclear Instruments and Methods in Physics Research Section B: Beam Interactions with Materials and Atoms, 8th International Conference of Nuclear Microprobe Technology and Applications, 2003. **210**: p. 250-255.

112. Bettiol, A.A., Sum, T.C., Cheong, F.C., Sow, C.H., Venugopal Rao, S., van Kan, J.A., Teo, E.J., Ansari, K., and Watt, F., *A Progress Review of Proton Beam Writing Applications in Microphotonics.* Nuclear Instruments and Methods in Physics Research Section B: Beam Interactions with Materials and Atoms, Nuclear Microprobe Technology and Applications, 2005. **231**(1-4): p. 364-371.

113. Bettiol, A.A., Venugopal Rao, S., Sum, T.C., van Kan, J.A., and Watt, F., *Fabrication of Optical Waveguides Using Proton Beam Writing.* Journal of Crystal Growth, International Conference on Materials for Advanced Technologies (ICMAT 2005, Symposium M - Photonic Materials and Devices, 2006. **288**(1): p. 209-212.

114. van Kan, J.A., Bettiol, A.A., Wee, B.S., Sum, T.C., Tang, S.M., and Watt, F., *Proton Beam Micromachining: A New Tool for Precision Three-Dimensional Microstructures.* Sensors and Actuators A: Physical, 2001. **92**(1-3): p. 370-374.

115. Alves, A., Hearne, S.M., Reichart, P., Siegele, R., Jamieson, D.N., and Johnston, P.N. *Ion Beam Lithography with Single Ions*. in *Micro- and Nanotechnology: Materials, Processes, Packaging, and Systems II*. 2005. SPIE. **5650**. p. 381-390

116. Alves, A., Reichart, P., Siegele, R., Johnston, P.N., and Jamieson, D.N., *Ion Beam Lithography Using Single Ions.* Nuclear Instruments and Methods in Physics Research Section B: Beam Interactions with Materials and Atoms, 2006. **249**(1-2): p. 730-733.

117. Schenkel, T., Persaud, A., Park, S.J., Nilsson, J., Bokor, J., Liddle, J.A., Keller, R., Schneider, D.H., Cheng, D.W., and Humphries, D.E., *Solid State Quantum Computer Development in Silicon with Single Ion Implantation.* Journal of Applied Physics, 2003. **94**(11): p. 7017-7024.

118. Kane, B.E., *A Silicon-Based Nuclear Spin Quantum Computer.* Nature, 1998. **393**(6681): p. 133-137.

119. Watt, F., van Kan, J.A., Rajta, I., Bettiol, A.A., Choo, T.F., Breese, M.B.H., and Osipowicz, T., *The National University of Singapore High Energy Ion Nano-Probe Facility: Performance Tests.* Nuclear Instruments and Methods in Physics Research Section B: Beam Interactions with Materials and Atoms, 8th International Conference of Nuclear Microprobe Technology and Applications, 2003. **210**: p. 14-20.

120. Grabiec, P., Radojewski, J., Zaborowski, M., Domanski, K., Schenkel, T., and Rangelow, I.W., *Batch Fabricated Scanning near Field Optical Microscope/Atomic Force Microscopy Microprobe Integrated with Piezoresistive Cantilever Beam with Highly Reproducible Focused Ion Beam Micromachined Aperture.* Journal of Vacuum Science & Technology B: Microelectronics and Nanometer Structures, 2004. **22**(1): p. 16-21.

121. Lehrer, C., Freya, L., Petersena, S., Sulzbachb, T., Ohlssonb, O., Dziombac, T., U., D.H., and H., R., *Fabrication of Silicon Aperture Probes for Scanning near-Field Optical*

Microscopy by Focused Ion Beam Nano Machining. Microelectronic Engineering, 2001. **57-58**: p. 721-728.

122. Dziomba, T., Sulzbach, T., Ohlsson, O., Lehrer, C., Frey, L., and Danzebrink, H.U., *Ion Beam-Treated Silicon Probes Operated in Transmission and Cross-Polarized Reflection Mode near-Infrared Scanning near-Field Optical Microscopy (Nir-Snom).* Surface and Interface Analysis, Proc. SXM-3: Conference on Development and Industrial Application of Scanning Probe Methods, 1999. **27**(5-6): p. 486-490.

123. Peplow, D.E., *Direction Cosines and Polarization Vectors for Monte Carlo Photon Scattering.* Nuclear Science and Engineering, 1999. **131**(1): p. 132-136.

124. Luthi, R., Schlittler, R.R., Brugger, J., Vettiger, P., Welland, M.E., and Gimzewski, J.K., *Parallel Nanodevice Fabrication Using a Combination of Shadow Mask and Scanning Probe Methods.* Applied Physics Letters, 1999. **75**(9): p. 1314-1316.

125. Schenkel, T., Rangelow, I.W., Keller, R., Park, S.J., Nilsson, J., Persaud, A., Radmilovic, V.R., Grabiec, P., Schneider, D.H., Liddle, J.A., and Bokor, J., *Open Questions in Electronic Sputtering of Solids by Slow Highly Charged Ions with Respect to Applications in Single Ion Implantation.* Nuclear Instruments and Methods in Physics Research Section B: Beam Interactions with Materials and Atoms, Proceedings of the Sixteenth International Conference on Ion Beam Analysis, 2004. **219-220**: p. 200-205.

126. Taylor, M.L., Alves, A., Reichart, P., Franich, R.D., Rubanov, S., Johnston, P.N., and Jamieson, D.N., *Ion Beam Lithography Using a Nano-Aperture.* Nuclear Instruments and Methods in Physics Research Section B: Beam Interactions with Materials and Atoms, 2006(Accepted for publication September 2006, Article In Press, Corrected Proof Available online 14 February 2007).

127. Alves, A., Johnston, P.N., Reichart, P., Jamieson, D.N., and Siegele, R., *Characterization of Ion Tracks in Pmma for Single Ion Lithography.* Nuclear Instruments and Methods in Physics Research Section B: Beam Interactions with Materials and Atoms, (In Press, Accepted Manuscript).

128. Breese, M.B.H., de Kerckhove, D.G., Jeynes, C., Peel, R.M.A., and Murray, C.W., *An Electrostatic Beam Rocking System on the Surrey Nuclear Microprobe.* Nuclear Instruments and Methods in Physics Research Section B: Beam Interactions with Materials and Atoms, 2001. **181**(1-4): p. 54-59.

129. de Kerckhove, D.G., Breese, M.B.H., and Grime, G.W., *A Beam Rocking System for the Oxford Nuclear Microprobe: A New Approach to Channeling Analysis.* Nuclear Instruments and Methods in Physics Research Section B: Beam Interactions with Materials and Atoms, 1997. **129**(4): p. 534-542.

130. de Kerckhove, D.G., Breese, M.B.H., and Grime, G.W., *An Optimised Beam Rocking System to Produce Angle-Resolved Information from Small Areas.* Nuclear Instruments and Methods in Physics Research Section B: Beam Interactions with Materials and Atoms, 1998. **140**(1-2): p. 199-208.

Appendix A

Publications Arising From This Work